AUTOMATED ALGEBRA FOR THE QUANTUM VIRIAL EXPANSION OF STRONGLY-COUPLED MATTER

Yaqi Hou

A dissertation submitted to the faculty at the University of North Carolina at Chapel Hill in partial fulfillment of the requirements for the degree of Doctor of Philosophy in the Department of Physics and Astronomy in the College of Arts and Sciences.

Chapel Hill
2022

Approved by:

Joaquin E. Drut

Gökçe Başar

Fabian Heitsch

Reyco Henning

Yue Wu

ABSTRACT

Yaqi Hou: Automated Algebra for the Quantum Virial Expansion of Strongly-coupled Matter
(Under the direction of Joaquin E. Drut)

The thermodynamics of generic quantum many-body systems is a technically challenging area of research relevant to different fields covering a vast energy range, from condensed matter physics at the low-energy end, atomic systems in the middle, and nuclear and QCD at higher energies. An open question at the forefront of research concerns, for instance, the thermodynamics of neutron and nuclear matter at finite temperature, as it is directly relevant to the behavior of dense matter in neutron star mergers. With the advent of multimessenger astronomy, these astrophysical environments where nuclear many-body physics is essential have attracted considerable attention in recent years. This dissertation focuses on one of the most widely-applied methods in the calculation of the thermodynamics of quantum many-body systems, namely the Quantum Virial Expansion (QVE), which is an expansion of the grand canonical partition function in powers of the fugacity. While applications of the QVE have seen successes in systems as different as ultracold atoms and dilute neutron matter, most investigations have been limited to the lowest order, due to the increasing complexity of the quantum few-body problem. The main development of this work is the construction of a new class of semi-analytic methods which we will generally call "Automated-Algebra methods" to tackle the QVE, offering higher and more accurate analytic estimations for its coefficients than ever before.

Due to general interest from the condensed matter, atomic physics, and nuclear astrophysics communities, we focus on a system of spin-1/2 fermions with and without external harmonic trapping. In both cases, we were able to push the calculation of the QVE to the unprecedented fifth order. The analytic nature of our method makes our results an analytic function of parameters such as dimension, coupling strength, and external trapping frequency, which greatly extends the range of prior results on lower-order coefficients. We applied our high-order QVE to examine properties, such as density, Tan's contact compressibility and spin susceptibility, and finding good agreement

with existing experimental results.

Thanks to the access to such high-order coefficients, we were able to apply series resummation methods, which greatly extended the applicability of the QVE to regimes at lower temperature, where the truncated finite-order expansion usually fails.

ACKNOWLEDGEMENTS

Writing this dissertation is like walking the path of the last six years again. It brings back all the good old days. I am very fortunate to say that I can barely think about any bad memories of my time at UNC. But this is not true, as this has nothing to do with the fortunate. Instead, all the credits go to my advisor, girlfriend, family, and friends, without whom I would never have such an enjoyable Ph.D. experience. I would also like to thank the members of my dissertation committee for their patience and help.

Most of all, I want to extend my deepest gratitude to my advisor, Joaquín E. Drut. You are more like a senior friend to me: thank you for listening to me babbling some stupid ideas, supporting and sharing with me when I am uncertain about my next step in life, and guiding me to walk through all the challenges I encountered. I will never forget our discussions about physics, economics, career and life, as well as all the other fascinating topics and ideas. Your kindness, generosity and the serious altitudes towards physics motivate me not only to do better research but also to become a better person for others. Neither will I forget our walks around the campus and Chapel Hill. That day when you came to my office and said, "Yaqi, let's take a walk outside" indeed started a wonderful tradition! By the way, thank you for buying me so many lunches: I am now a huge fan of Cosmic Cantina and Chipotle (especially the former).

I owed so much to my parents and grandparents in the past years. It has been nearly six years since the last time we met in person, and I am so sorry for my missing part in the family, and not being able to be where I should be in the time needed. I can't say how grateful I am for your unconditional love and support, as well as the freedom to choose this major I loved when I started college.

Last and definitely not least[1], I would like to thank my girlfriend Yunjuan Liu. Without you, I would never have become the person I am now. The time with you made me a better person

---

[1] which is another reason why we human beings should evolve our language system to two-dimensional or at least cyclical to avoid such a tricky situation.

and helped me to grow from a (little bit too old) boy to a (yet still learning) man. Thank you for being with me and support me during this particular period of my life.

TABLE OF CONTENTS

LIST OF FIGURES

LIST OF TABLES

LIST OF ABBREVIATIONS

1D	One spatial dimension
2D	Two spatial dimensions
3D	Three spatial dimensions
l.h.s.	left hand side
r.h.s.	right hand side
AA	Automated algebra
CL	Complex Langevin
CPF	Canonical Partition Function
EOS	Equation of States
GCPF	Grand-Canonical Partition Function
LW	Luttinger-Ward
QFT	Quantum field theory
QVE	Quantum virial expansion
QMC	Quantum Monte Carlo
PIMC	Path-Integral Monte Carlo

LIST OF SYMBOLS

$\equiv$	set equal
b_n	n-th order virial coefficient
Δb_n	interaction-induced changes in the n-Th order virial coefficient
Ω	Grand thermodynamic potential
$\mathcal{Z}$	Grand canonical partition function
Q_N	Canonical partition function for N-particles system
λ_T	Thermal de Broglie wavelength
k_B	Boltzmann's constant
k_F	Fermi momentum
a_s	Scattering length
r_e	Effective range
S_{eff}	Effective action
σ	Hubbard-Stratonovich auxiliary field
N_τ	Temporal time steps
$\hbar$	Reduced Planck's constant
β	Inverse temperature
μ	Chemical potential
h	Polarization
z	Fugacity
χ	Susceptibility
$\mathcal{K}$	Compressibility
$\mathcal{I}$	Tan contact
n	Density
P	Pressure
$\hat{H}$	Hamiltonian operator
$\hat{T}$	Kinetic energy operator
$\hat{V}$	Potential energy operator
$\hat{N}$	Particle number operator

CHAPTER 1: Introduction

The last few decades witnessed a boom in the research of quantum many-body systems: the advent and maturity of experimental techniques led adventures into uncharted regimes; the further development and adoption of theoretical tools such as quantum field theory greatly enrich the theoretical arsenal and keep offering new insights. Furthermore, the rapid evolution in modern computer offers unimaginable computational powers, pushing the study of many-body problem into the precision era.

This dissertation is mostly devoted to ultracold atoms and its relatives, which have basically experienced the full story above, while still mysterious, holding the key to various fields such as superconductors and quantum computing. Starting around the beginning of this century, the achievements from the experimental side greatly boosted the investigation in the field of ultracold atoms. Among them, the so-called Feshbach resonance technique is surely special as it allows researchers to finely control the interaction strength between the particles, making it possible to explore various regimes in the phase diagram. In particular, with Feshbach resonances, experimentalists are able to connect two famous and well-developed theories: the Bardeen-Cooper-Schrieffer (BCS) theory which governs weakly attractive fermions, and the Bose Einstein condensation (BEC) theory for bosonic systems. Such process is called BCS-BEC crossover and will play a central role in this dissertation. Although its existence has long been theoretically predicted [1–4], it did not become experimentally accessible until 2004 using the Feshbach resonance technique [5, 6]. Since then, the investigations in relevant fields have been heated in the physics community.

In this dissertation, we mainly focus on the non-relativistic spin-1/2 Fermi gas system through the lens of a method called Quantum Virial Expansion (QVE). The physics of such a system is not just relevant to the ultracold atom community: via a universal point in the middle of BCS-BEC crossover called the unitarity limit, for example, we can relate the ultracold atoms to neutron matter and even nuclear matter (as an approximation). On the methodological side, although QVE has been widely applied in various fields to offer predictions of thermodynamics or other observables, they are usually limited to the second or third order in the expansion. The theo-

retical study of high-order coefficients in the QVE has been limited by the increasing difficulties of higher-body physics from both analytical and numerical fronts. One of the central questions we aim to answer in this dissertation is how to tackle this challenge by developing a novel semi-analytical method which bridges the analytical and numerical fronts.

Section 1.1: BCS-BEC crossover and ultracold atoms

In this first section, we begin with a qualitative introduction to the BCS-BEC crossover. Although this dissertation focus more on the theoretical studies, we devote a short section on ultracold atoms experiment to offer more context and establish the rough physics picture for our works.

1.1.1: BCS-BEC Crossover

Phenomenology and phase diagram

One of the most commonly investigated systems in the ultracold atoms community is the two-species $(\uparrow, \downarrow)$ Fermi gas with attractive interactions in 3D. In the absence of polarization, i.e. when there are $N_\uparrow = N_\downarrow$ particles for species $\uparrow, \downarrow$, the phase diagram is shown in Fig. 1.1. The horizontal axis shows $1/(k_F a_s)$, which is a measure of the coupling strength. Here, $k_F \propto n^{1/3}$ is the Fermi momentum and equivalently a measure of the density, and a_s is the s-wave scattering length. For the dilute regimes studied with ultracold gases, a_s is the only scale characterizing the interaction. The smooth transition of the coupling strength from the left to right, as controlled using the Feshbach resonance in the experiments, then defines the famous BCS-BEC crossover.

As $1/(k_F a_s) \to -\infty$, we are in the so-called BCS regime[1], where the system is Fermionic with weak attractive interaction. BCS theory governs and describes the formation and condensation of Cooper pairs. The size of Cooper pairs ξ follows $\xi \gg \lambda_F \propto n^{-1/3}$, where λ_F corresponds to the interparticle distance.

At $1/(k_F a_s) = 0$, we are at the so-called unitary limit (or unitary point), which is the threshold for bound-state formation. In this regime, the pairs have size comparable to the interparticle distance, i.e. $\xi \approx \lambda_F$. The divergence of the only length scale, the scattering length, is a peculiar feature. Due to the lack of length scales, properties in this unitary regime are universal: all phys-

---

[1] strictly speaking, the system becomes a free Fermi gas in the limit
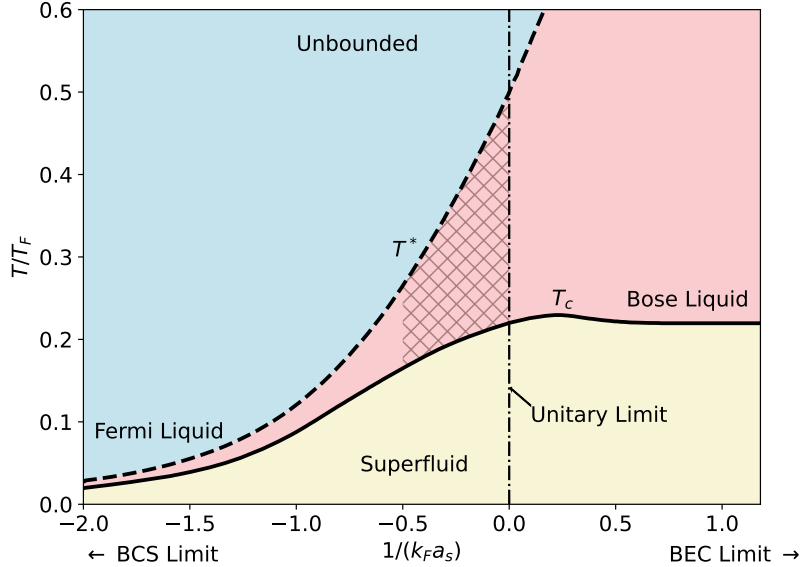
Figure 1.1: (Figure is inspired by Fig. 3 of Ref. [7]) Qualitative phase diagram of the BCS to BEC crossover as a function of the temperature T/T_F, where T_F is the Fermi temperature, and the dimensionless coupling $1/(k_F a_s)$, where k_F is the Fermi momentum and a_s is the scattering length. The attraction coupling is changing from weak to strong from the left to right. To the left as $1/(k_F a_s) \rightarrow -\infty$, the system approaches the BCS limit; and as $1/(k_F a_s) \rightarrow \infty$, the system approaches the BEC limit. In between at $1/(k_F a_s) = 0$, as indicated by the dashed-dotted line, it is a special point called the unitary limit or unitarity. The thick dashed line represent the pairing-formation crossover temperature T^*. Note that the T^* boundary does not represent a phase presentation and is only a qualitative representation of the crossover scale. The solid line represents the condensation temperature T_c, below which condensate exists. Different colors represent the phases qualitatively. The yellow region corresponds to the superfluid phase. In the blue region, the system is Fermionic, in the form of normal Fermi liquid at low temperature. In the red region, One caveat is that the boundary between Fermi phase and Bose phase should not be taken as precise, but rather a "blurred" boundary representing the finite-temperature crossover between the Fermi liquid and Bose liquid. Such crossover is presumably related to a pseudogap phase [8, 9], represented as the cross-shaded region in between T^* and T_c.

ical quantities are given by dimensionless functions that do not depend on the details of the system (cold atoms, neutrons, etc.) multiplied by a power of the density. For example, as pointed by Bertsch [10], the ratio between the ground-state energy of the unitary gas and its noninteracting counterpart is a universal number called Bertsch parameter, which can also describe low density neutron matter.

As $1/(k_F a_s) \rightarrow +\infty$, we reach the BEC regime. The strong attractive interaction bound Fermions into bosonic dimers with pair size $\xi \ll \lambda_F$. The inter-dimer interaction is the reminisce of attraction and becomes effectively weak repulsion, which is therefore governed by the BEC theory. The bosonic dimers condense into a superfluid phase below the critical temperature T_c. Compared to the BCS limit, where the pair formation and condensation occur nearly simultaneously,

the pair-formation temperature T^* diverges from the the condensation critical temperature T_c, leaving room to the so-called pseudogap region in between, whose existence is currently under active investigations and debates. We will revisit this topic in Sec. 3.4.5.

Low-energy effective theory

In scattering theory, the scattering can happen in states with different angular momentum $l = 0, 1, 2, \ldots$, named as s-, p-, d-wave scattering and so on. In the case of ultracold atoms, the system is very dilute and the incident energy is so small that the angular motion is frozen out. Therefore, the s-wave scattering ($l = 0$) is the dominant contribution. The corresponding phase shift defines scattering parameters via the effective range expansion [11]

$$k \cot \delta_0(k) = -1/a_s + \frac{1}{2} r_e k^2 + \ldots \tag{1.1}$$

where a_s is scattering length and r_e is the effective range. At low energies and low densities, $r_e k^2 \ll 1$ and so the second term can be omitted.

The unitary limit mentioned above is named after that fact that the phase shift $\cot \delta_0 = -1/ka_s$ becomes zero and the scattering amplitude $f(k) = (k \cot \delta_0 - ik)^{-1}$ reaches its maximum value $-(ik)^{-1}$ allowed by unitarity. Passing this point, two fermions form a bound state with energy $E_B = 1/ma_s^2$.

In particular, the scattering length diverges at unitarity, erasing out the only length scale. This implies the universality in the unitary limit and hence relates distinct systems such as dilute ultracold atoms at density $n \approx 10^{-12} \text{cm}^{-3}$ and neutron matter at low density $n \approx 10^{-4} \text{fm}^{-3}$ [12].

1.1.2: Ultracold atom experiments

For a relative long time, quantum gases and strongly correlated systems were two distinct topics, as the quantum gases were thought to be weakly-coupled and research in strongly correlated systems was mostly restricted to the dense and strongly interacting quantum liquids [13]. Starting around 2000s, several experimental achievements changed this picture and revolutionized the study of ultracold atoms. In this section, we will discuss three types of developments:

1. techniques such as laser cooling or evaporative cooling to cool atomic clouds down to the mili-Kelvin regime, where quantum effects are manifest;
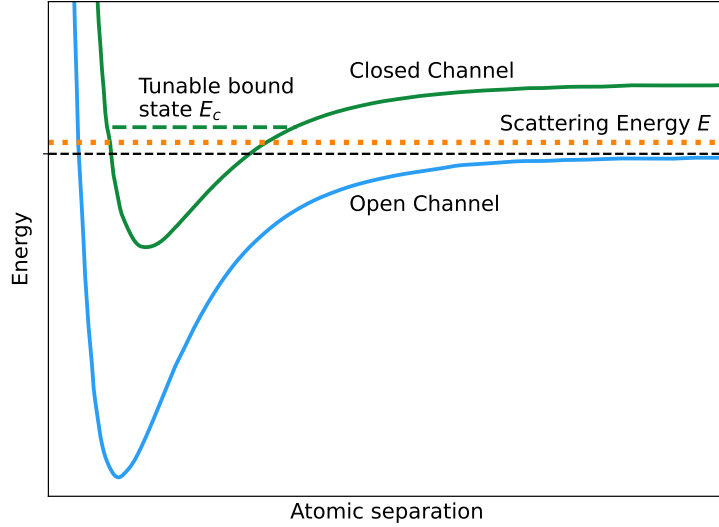
Figure 1.2: The qualitative sketch of the two-channel model for a Feshbach resonance. The blue and green curves correspond to the energy of open and closed channel respectively. The orange dotted line corresponds to the scattering energy E, which is close to zero for the ultracold atoms. The green dashed line represents the molecular bound state supported by the closed channel, with a tunable bound energy E_c. The Feshbach resonance occurs as E_c approaches E.

2. the trapping techniques like magnetic or optical ones to modulate the system;

3. the Feshbach resonance technique to tune the interaction strength

In the end, we also outline other active areas such as the microscopes that brings ultracold atom experiments to the single-atom level.

Cooling, trapping and tuning

The most popular system in ultracold atom experiments is the system of dilute ultracold alkali atoms such as ^{40}K or ^{6}Li or their mixtures, because there is only one electron in the outermost shell and the nuclei structure is negligible compared to the overall experimental length scale. In ultracold atom experiments, the atomic cloud is cooled down into the degenerate regime using techniques like laser cooling or evaporative cooling. The low temperature corresponds to large thermal de Broglie wave length λ_T, which then defines the diluteness by requiring the density n to satisfy $n^{-1/d} \ll \lambda_T$, where d is the spatial dimension.

After cooling down, an external trap is imposed to confine the atoms and separate the sys-

tem from the "hot" walls. The optical dipole trap is the most commonly used confinement, which is formed by two focused counter-propagating Gaussian beams. Compared to magnetic traps, optical traps are compatible with arbitrary homogeneous magnetic fields without affecting the trap, which is essential for Feshbach tuning (described below). Optical traps are also more universal than magnetic traps as the latter cannot be used to investigate lowest atomic state, which is high-field seeking state [14]. Due to the shape of the trap, the density profile is no longer homogeneous. Usually, the trapping frequency is small enough such that the so-called local-density approximation (LDA) can be safely assumed. Under its assumption, the gas can be regarded as locally homogeneous everywhere in the trap. However, even at small trap frequency, the LDA may still break down [15] and hence the trapped system is an important topic for theoretic study (See Chap. 5).

The external traps also serve to modulate the system by reducing the dimensionality or creating periodic lattices. For example, when squeezing the transverse potential such that the transverse trap energy $\hbar\omega_\perp$ is much larger than the Fermi energy $E_F = N\hbar\omega_z$, the trapped gas becomes kinematically one-dimensional [16]. Another example is the optical lattice: by overlapping two or three orthogonal standing waves, it is possible to trap the gases in two- and three- dimensional periodic lattice potentials. The optical lattice allows the experimental simulation of lattice models such as Hubbard-Fermi model, which is believed to be important for high-T_c superconductors, and is generally an important model in condensed matter physics.

Another revolutionary technique to modulate the system is the Feshbach resonance, which can tune the coupling strength between difference species either magnetically or optically. Both realizations share the similar concepts and can be qualitatively described with a two-channel model, as shown in Fig. 1.2. The open (blue) and closed (green) channels are "resonantly coupled" when the bound state in closed channel has energy E_c close to the open channel threshold, which is usually set to be zero. Taking the magnetic Feshbach resonance for example, if the open and closed channels carry different magnetic moments, it is possible to magnetically tune the position of E_c. In experiments, the atoms are prepared in the open channel with low incident energy before collision. In the course of the collision, the open channel is coupled to the closed channel, and when a bound state has energy E_c close to zero, a scattering resonance occurs. It is then shown

that the scattering length is

$$a(B) = a_{bg} \left(\frac{\Delta}{B - B_0} \right), \tag{1.2}$$

where a_{bg} is the scattering length associated with open channel potential only while Δ and B_0 are the width and position of resonance respectively. Therefore, via controlling external magnetic field, it is possible to probe scattering length from $-\infty$ to ∞. The resonant point where $a(B)$ diverges is just the unitary point. This is only a rough picture of Feshbach resonance; for more details, see e.g. Ref. [17].

Atomic microscopes

Another active area in ultracold atom experiments aims to improve the probing resolution and achieve finer control of the system, which is called atomic microscopy. Usually, the resolution is determined by the probing wavelength, half of it to be more specific. Multiple methods have been developed in recent years to achieve "superresolution" imaging that could resolve objects up to 50 times smaller than the probing optical wavelength [18], and therefore it is possible to probe the system at the single atom level. The atomic microscope is essential to quantum simulators, a sub-area of the quantum computation, as it allows the direct observation of properties such as magnetic order and entanglement. One example of such a quantum simulator is fermions trapped in an optical lattice as a realization of the Fermi-Hubbard model, which is believed to be relevant to high-T_c superconductors [19].

Section 1.2:   Review of Quantum Statistical Physics: noninteracting Fermi gas

We devote this section to reviewing several important concepts in quantum statistical physics. In particular, we consider the noninteracting, non-relativistic spin-1/2 Fermi gas as example to demonstrate the basic formalism and derive some thermodynamic properties.

For a general system, the Hamiltonian can be written as three terms:

$$\hat{H} = \underbrace{\hat{T} + \hat{V}_{\text{ext}}}_{\hat{H}_0} + \hat{V}_{\text{int}}, \tag{1.3}$$

where $\hat{T}$ is the kinetic energy operator. In the non-relativistic system, it is

$$\hat{T} = \sum_{s=\uparrow,\downarrow} \int d^d r \, \hat{\psi}_s^\dagger(\mathbf{r}) \left(-\frac{\hbar \nabla^2}{2m}\right) \hat{\psi}_s(\mathbf{r}), \tag{1.4}$$

where $\hat{\psi}_s^\dagger(\mathbf{r})$ and $\hat{\psi}_s(\mathbf{r})$ are, respectively, the creation and annihilation operators for particles of spin s at position $\mathbf{r}$. Alternatively, we use its diagonal form in the momentum representation

$$\hat{T} = \sum_{s=\uparrow,\downarrow} \int d^d p \, \frac{\mathbf{p}^2}{2m} \hat{n}_s(\mathbf{p}), \tag{1.5}$$

where $\hat{n}_s(\mathbf{p}) = \hat{\psi}_s^\dagger(\mathbf{p})\hat{\psi}_s(\mathbf{p})$ is the particle number operator in the momentum space.

The second term $\hat{V}_{\text{ext}}$ is the operator of external potential, whose form depends on the configuration. In most part of this dissertation, we consider the homogeneous system, i.e. $\hat{V}_{\text{ext}} = 0$, while in Chap. 5, we will discuss the harmonically trapped system with the non-zero $\hat{V}_{\text{ext}}$ term.

The last term $\hat{V}_{\text{int}}$ is the inter-particle interaction operator. Through out this dissertation, we exclusively consider the contact interaction model in form of

$$\hat{V}_{\text{int}} = -g_d \int d^d r \, \hat{n}_\uparrow(\mathbf{r})\hat{n}_\downarrow(\mathbf{r}), \tag{1.6}$$

where g_d is the bare coupling and the minus sign is by convention to make g_d positive for the attractive interactions. The operator $\hat{n}_s(\mathbf{r}) = \hat{\psi}_s^\dagger(\mathbf{r})\hat{\psi}_s(\mathbf{r})$ is the particle density operator for spin-s particles in the coordinate space. Note that we have only one parameter g_d as there is only one parameter a_s modeling the scattering in the zero-range s-wave model. To tune the system to the unitary limit, we renormalize the bare coupling g_d, or just g for short, to reproduce the unitary physics, as will be discussed in more details in Sec. 2.2.4. For simplicity, we will denote $\hat{V}_{\text{int}}$ as $\hat{V}$ from now on. We will also use natural units across the dissertation such that $\hbar = k_B = m = 1$.

In the noninteracting case, consider the Hamiltonian in the momentum representation

$$\hat{H} = \hat{T} = \frac{\hat{\mathbf{p}}^2}{2m}, \tag{1.7}$$

where the boldface momentum $\mathbf{p}$ refers to the vector in arbitrary dimensions, a notation we will use throughout this document.

The core quantity of quantum statistical physics is the Grand-Canonical Partition Function (GCPF) $\mathcal{Z}$, defined as

$$\mathcal{Z} = \mathrm{Tr}_F \exp\left[-\beta(\hat{H} - \mu\hat{N})\right], \tag{1.8}$$

where $\beta = (k_B T)^{-1}$ is the inverse temperature (also known as the imaginary time), μ the chemical potential, $\hat{N}$ the particle number operator, and Tr_F the trace over the many-body Fock space.

To evaluate the GCPF, at least in theory, we have the freedom to choose any representation. Here, we take the conventional path as in Ref. [20] using the occupation number representation. Denote the occupation number basis as $|n\rangle = |n_0, n_1, n_2, \ldots\rangle$, where i is the ith energy level and n_i is the particle number occupying that level, we have

$$\hat{H}|n\rangle = \sum_i n_i \epsilon_i,$$
$$\hat{N}|n\rangle = \sum_i n_i \equiv N, \tag{1.9}$$

where ϵ_i is the energy at i^{th} level. The GCPF is then

$$\mathcal{Z} = \sum_{N=0}^{\infty} \sum_{\{|n\rangle\}_N} \exp\left[-\beta \sum_i (n_i \epsilon_i - \mu n_i)\right],$$
$$= \sum_{N=0}^{\infty} \sum_{\{|n\rangle\}_N} \prod_i \left[z^{n_i} \exp(-\beta n_i \epsilon_i)\right], \tag{1.10}$$

where $z = \exp(\beta\mu)$ is the fugacity and the $\{|n\rangle\}_N$ under the second summation refers to all possible states satisfying $\sum_i n_i = N$. The double summation is equivalent to summing over all possible values of n_i independently, i.e.

$$\mathcal{Z} = \sum_{n_0=0}^{\infty} \left(z e^{-\beta\epsilon_0}\right)^{n_0} \sum_{n_1=0}^{\infty} \left(z e^{-\beta\epsilon_1}\right)^{n_1} \sum_{n_2=0}^{\infty} \left(z e^{-\beta\epsilon_2}\right)^{n_2} \ldots, \tag{1.11}$$

For Fermi gases, n_i can only take the value of 0 or 1, and therefore

$$\mathcal{Z} = \prod_i \left(1 + z e^{-\beta\epsilon_i}\right). \tag{1.12}$$

The GCPF encodes all the thermodynamics of the system and we can derive multiple equations of state from it. More specifically, the directly-related quantity is the logarithm $\ln \mathcal{Z}$, which is also called q-potential as in Ref. [20] or written in terms of the grand potential Ω via

$$-\beta\Omega = \ln \mathcal{Z} = \sum_i \ln\left(1 + ze^{-\beta\epsilon_i}\right). \tag{1.13}$$

The pressure is then immediately accessible through the relation

$$\beta PV = -\beta\Omega = \sum_i \ln\left(1 + ze^{-\beta\epsilon_i}\right), \tag{1.14}$$

and the particle number is given as

$$N = \frac{\partial \ln \mathcal{Z}}{\partial \ln z} = \sum_i \frac{1}{1 + z^{-1}e^{\beta\epsilon_i}}. \tag{1.15}$$

Other quantities such as the energy, free energy and entropy can be derived in a similar fashion.

To evaluate the above expressions, we use the free particle energy

$$\epsilon_i = \epsilon(p) = \frac{\mathbf{p}^2}{2m}. \tag{1.16}$$

In a continuous system, the summation is replaced with the corresponding integration, and Eq. (1.14) now becomes

$$\begin{aligned}
\ln \mathcal{Z} &= \sum_{\mathbf{p}} \ln[1 + ze^{-\beta\mathbf{p}^2/(2m)}] \\
&= \left(\frac{L}{2\pi}\right)^d \int_{-\infty}^{\infty} d^d p \ \ln[1 + ze^{-\beta\mathbf{p}^2/(2m)}],
\end{aligned} \tag{1.17}$$

where d is the dimension and L is the system size in one dimension[2], and

$$d^d p = \prod_i^d d\mathbf{p}_i. \tag{1.18}$$

---

[2]Here we assume the system has the same length in all dimension just for simplicity. The result is valid for any systems and we can replace L^d with V to accommodate it.

In the 3D case, we use spherical coordinates

$$\ln \mathcal{Z} = \left(\frac{L}{2\pi}\right)^3 \int_{-\pi}^{\pi} \mathrm{d}\phi \int_0^{\pi} \sin\theta \mathrm{d}\theta \int_0^{\infty} r^2 \mathrm{d}r \ \ln[1 + z\mathrm{e}^{-\beta r^2/(2m)}], \tag{1.19}$$

where the angular parts are trivial and yield 4π. The integral over r can be evaluated using integration by parts, leading to the final expression

$$\ln \mathcal{Z} = \frac{V}{\lambda_T^3}\left[\frac{4}{3\sqrt{\pi}} \int_0^{\infty} \mathrm{d}x \frac{x^{3/2}}{z^{-1}\mathrm{e}^x + 1}\right] = \frac{V}{\lambda_T^3} f_{\frac{5}{2}}(z), \tag{1.20}$$

where we substituted the integration variable $p \rightarrow x = \beta p^2/(2m)$ and $\lambda_T = \sqrt{2\pi\beta}$ is the thermal wavelength.

This integral inside the square bracket is called Fermi-Dirac function, denoted as $f_{\frac{5}{2}}(z)$ where the subscript $\frac{5}{2}$ is the order of Fermi-Dirac function. More generally, the Fermi-Dirac function is defined as

$$f_\nu(z) \equiv \frac{1}{\Gamma(\nu)} \int_0^{\infty} \frac{x^{\nu-1}\mathrm{d}x}{z^{-1}\mathrm{e}^x + 1} = z - \frac{z^2}{2^\nu} + \frac{z^3}{3^\nu} + \dots. \tag{1.21}$$

The same function is sometimes referred to in the literature by its mathematical name, the polylogarithm function $\mathrm{Li}_\nu(z)$, defined as

$$\mathrm{Li}_\nu(z) = \sum_{k=1}^{\infty} \frac{z^k}{k^\nu} = z + \frac{z^2}{2^\nu} + \frac{z^3}{3^\nu} + \dots, \tag{1.22}$$

Hence Eq. (1.20) is now written as

$$\ln \mathcal{Z} = \frac{V}{\lambda_T^3} f_{\frac{5}{2}}(z) = -\frac{V}{\lambda_T^3} \mathrm{Li}_{\frac{5}{2}}(-z). \tag{1.23}$$

So far, we have not yet taken into consideration the spin degree of freedom. In the noninteracting case, it is straightforward to include the second species as there is no interaction between the two species. Therefore the total GCPF is factorized as $\mathcal{Z} = \mathcal{Z}_\uparrow \mathcal{Z}_\downarrow$, and in the spin-balanced

case, such internal structure introduces a multiplicity factor into Eq. (1.23)

$$\ln \mathcal{Z} = \frac{gV}{\lambda_T^3} f_{\frac{5}{2}}(z) = -\frac{gV}{\lambda_T^3} \mathrm{Li}_{\frac{5}{2}}(-z), \tag{1.24}$$

where $g = 2$ for the spin-1/2 system, but could take other values in general. [3]

More generally, in d dimensions, the integral element becomes

$$\sum_k \rightarrow \left(\frac{L}{2\pi}\right)^d \int \mathrm{d}^d k = \left(\frac{L}{2\pi}\right)^d \int_0^\infty \mathrm{d}k S_d(k), \tag{1.25}$$

where $S_d(k) = \frac{2}{\Gamma(d/2)} \pi^{d/2} k^{d-1}$. Following the same steps, we eventually have

$$-\beta\Omega = \ln \mathcal{Z} = \frac{gL^d}{\lambda_T^d} f_{\frac{d}{2}+1}(z). \tag{1.26}$$

Similarly, the noninteracting density and pressure equation in d dimensions are

$$P = \frac{g}{\beta\lambda_T^d} f_{\frac{d}{2}+1}(z), \tag{1.27}$$

$$n = \frac{N}{V} = \frac{g}{\lambda_T^d} f_{\frac{d}{2}}(z), \tag{1.28}$$

where we used the property of Fermi-Dirac function $\partial f_\nu(z)/\partial \ln z = f_{\nu-1}(z)$.

Section 1.3: Quantum Virial Expansion

1.3.1: Breaking down many-body systems

In the previous section, we evaluated the grand-canonical partition function $\mathcal{Z}$ in the occupation number representation. When evaluating the GCPF, we converted the Fock trace into a double summation over the system particle number N and all possible states of N particles, as shown in Eq. (1.10). In evaluating that equation, we convert the double summation into a series of independent summation for each state as in Eq.(1.11). A natural question arises: can we evaluate this double summation in a straightforward fashion, i.e. taking the first summation over N from 0 to ∞ explicitly?

---

[3]In fact, in other contexts (QCD but also in condensed matter), it is often useful to theoretically consider systems with g species, where g can take on any value, even complex!

Interpreting Eq. (1.10) from this perspective leads to the idea of an important technique, also the central piece of this dissertation, called Quantum Virial Expansion (QVE). To begin with, rewrite Eq. (1.10) as

$$\mathcal{Z} = \sum_{N=0}^{\infty} z^N \left[\sum_{\{|n\rangle\}_N} \prod_i \exp(-\beta n_i \epsilon_i) \right]. \tag{1.29}$$

Let us neglect the terms inside the square bracket for a while and assume they are just some known numbers. Now, the r.h.s. of Eq. (1.29) can be treated as a power series in z, and interpreted as an approximation of the true infinite-body system using finite system of N particles. In other words, we are reconstructing the open system (i.e. $\mathcal{Z}$) using a series of closed systems of $N = 0, 1, 2, 3, \ldots$ particles. By adding one particle at a time, we will approach the true physics eventually.

Formally, the above interpretation is the result of the decomposition of the Fock space as a direct sum of the Hilbert spaces for systems of $0, 1, 2, \ldots$ particles, i.e.

$$\mathcal{F} = \bigoplus_{N=0}^{\infty} \mathcal{H}_N, \tag{1.30}$$

where $\mathcal{F}$ is the Fock space and $\mathcal{H}_N$ is the N-particle Hilbert space. The latter is constructed from the single-particle Hilbert space $\mathcal{H}$ as $\mathcal{H}_N = \mathcal{S}\mathcal{H}^{\otimes N}$, where $\mathcal{S}$ is the (anti-)symmetrization operator depending on the particle type.

We can then write the Fock trace as

$$\mathrm{Tr}_F = \bigoplus_{N=0}^{\infty} \mathrm{tr}_N, \tag{1.31}$$

where tr_N is the trace over the Hilbert space for the N-particle system. Thus, the grand-canonical partition function $\mathcal{Z}$ is also decomposed as

$$\mathcal{Z} = \sum_{N=0}^{\infty} z^N Q_N. \tag{1.32}$$

where $Q_N = \mathrm{tr}_N e^{-\beta \hat{H}}$ is the Canonical Partition Function (CPD) Q_N for N-particle system. Now, we see that the Q_N is exactly the square-bracketed term in Eq. (1.29), which sums over all

possible states $\{|n\rangle\}_N$ in a system of $N = \sum_i n_i$ particles, i.e. takes the trace in the N-body Hilbert space.

In short, instead of evaluating the GCPF directly in the Fock space consisting infinite particles, we can approximately reproduce the physics by summing up a series of finite-body systems of $N = 0, 1, 2, \ldots$ particles. This is the fundamental philosophy behind the QVE.

Mathematically, we define the QVE as the expansion of the grand potential $-\beta\Omega = \ln\mathcal{Z}$ in terms of fugacity z.

$$-\beta\Omega = \ln\mathcal{Z} \equiv Q_1 \sum_{k=1}^{\infty} z^n b_n, \tag{1.33}$$

where b_n is a dimensionless number defined as the nth-order virial coefficient. For clarity, we will use lower n to denote the particle number for the virial coefficients, while still keeping the capital N to refer the particle number in the canonical partition function Q_N.

Once we knew the virial coefficients b_n (ideally in form of an analytic function of the order n), we can then reconstruct the GCPF as well as other thermodynamics observables. For example, using Eq. (1.15), the density in terms of QVE is then

$$n = \frac{Q_1}{V} \sum_{n=1}^{\infty} n b_n z^n. \tag{1.34}$$

However, for large n, it is very challenging to obtain numerical results, not to mention analytic ones, especially in the presence of interactions. In practice, our best hope is to push the calculation of b_n to as large n as possible and use the truncated finite-order series (or its variants as will be explained later) to approximate the true many-body physics.

At the first glance, the QVE may seem like a sub-optimal method compared to the direct approach. However, in general situations when the interaction is present, it is even more difficult, if not impossible, to take the Fock trace directly. On the other hand, the finite-body systems are usually easier for both analytical (at least for $N \leq 3$) and numerical studies. In fact, as we will see in the later chapters, we do not need very high order in the expansion to reproduce the true many-body physics with satisfactory accuracy, even when z is greater than unity.

The QVE is particularly useful in studying strongly coupled systems in the regime $\lambda_T/\lambda_F \ll$

1. One prominent example is the Unitary Fermi Gas as will be discussed in Sec. 3.1, where the conventional perturbation theory is no longer applicable due to the lack of small-value expansion parameter. In this sense, we can also interpret the QVE as a kind of perturbation theory around the interacting classical system, with z as the expansion parameter. To be precise, if $z \ll 1$, such that only $N = 1$ system is important, then we are in a noninteracting regime. However, interactions will typically leave a clear imprint on the $N = 2, 3, \ldots$ subspaces, which in turn modify the many-body picture.

1.3.2: Calculation of virial coefficients

To evaluate the coefficients b_n, we start by substituting the $\mathcal{Z}$ in Eq. (1.33) with Eq. (1.32), and then expand the logarithm in powers of z, we have

$$
\begin{aligned}
\ln \mathcal{Z} &= \ln \sum_{N=0}^{\infty} z^N Q_N = \ln\left(1 + zQ_1 + z^2 Q_2 + \ldots\right) \\
&= (zQ_1 + z^2 Q_2 + \ldots) - \frac{1}{2}(zQ_1 + z^2 Q_2 + \ldots)^2 + \frac{1}{3}(zQ_1 + z^2 Q_2 + \ldots)^3 + \ldots
\end{aligned}
\tag{1.35}
$$

Expanding and organizing Eq. (1.35) by the power of z, and comparing to Eq. (1.33) order by order, the virial coefficients b_k can be expressed in terms of Q_N. The first few coefficients are given as

$$
b_1 = 1,
\tag{1.36}
$$

$$
b_2 = \frac{Q_2}{Q_1} - \frac{Q_1}{2!},
\tag{1.37}
$$

$$
b_3 = \frac{Q_3}{Q_1} - b_2 Q_1 - \frac{Q_1^2}{3!},
\tag{1.38}
$$

$$
b_4 = \frac{Q_4}{Q_1} - \left(b_3 + \frac{b_2^2}{2}\right)Q_1 - b_2\frac{Q_1^2}{2!} - \frac{Q_1^3}{4!},
\tag{1.39}
$$

$$
b_5 = \frac{Q_5}{Q_1} - (b_4 + b_2 b_3)Q_1 - \left(b_2^2 + b_3\right)\frac{Q_1^2}{2} - b_2\frac{Q_1^3}{3!} - \frac{Q_1^4}{5!},
\tag{1.40}
$$

and so on.

The above equations verify our previous statement that the b_n captures the physics of the N-particle system, which is represented mathematically by the first term Q_N for each b_n. Based on the dimensional argument, the b_n is a dimensionless number, while Q_N is of dimension V^N, where V is for volume. In this sense, the expression for b_n can be divided into two parts: the first term

Q_N/Q_1 which includes both volume-independent and higher-dependent parts; and the rest terms to cancel out the contributions from Q_N/Q_1 at higher-volume order. We can also interpret the expression diagrammatically: the first term includes all kinds of diagrams, both connected and disconnected, while the rest terms are all disconnected diagrams. Hence the b_n contains only the connected diagram contributions. More details and examples of the diagrammatic interpretation are presented in Appendix. E.

The derivation of Eq. (1.36) relies on the Taylor expansion of logarithm function. Generally speaking, it is expected that the QVE is a good description when $z \ll 1$. Unfortunately, there are essentially no studies regarding its radius of convergence, which will typically be reduced by interactions. However, from a more physical standpoint, the expansion corresponds to a true physical quantity, which must converge. In this sense, the divergence of QVE is barely a mathematical artifact in the polynomial basis. In theory, we are able to obtain the convergent physical results by using a different basis or implementing other mathematical tools to circumvent certain singularities[4]. Actually, as we will demonstrate in later chapters, we observe quantitatively correct results using QVE even beyond $z > 1$.

Now, the task of calculating b_n is converted to calculating Q_N, or at least the part of Q_N at the same volume order as Q_1. We further break down the whole space of N-particle system into corresponding subspaces, i.e. decompose Q_N as

$$Q_N = \sum_{MJ}{}' Q_{MJ}, \tag{1.41}$$

where the primed summation is subject to the constraint $M + J = N$, and $M, J \geq 0$ for M (J) spin-up (down) particles. For example, we have

$$Q_3 = Q_{30} + Q_{21} + Q_{12} + Q_{03} = 2Q_{30} + 2Q_{21}, \tag{1.42}$$

$$Q_4 = Q_{40} + Q_{31} + Q_{22} + Q_{13} + Q_{04} = 2Q_{40} + 2Q_{31} + Q_{22}, \tag{1.43}$$

and so on. Note that we use the particle symmetry that $Q_{MJ} = Q_{JM}$ as we consider only the

---

[4]However, we note that such argument may not work in the critical region around the phase transition, where infinite singularities will accumulate in the complex plane of z. In this case, we will not find an appropriate tool circumventing the singularities to cross the critical point.

mass-balanced system ($m_\uparrow = m_\downarrow$) in this dissertation. In the case of mass imbalance, the second equal will no longer hold true.

We will leave the details on evaluating the subspace partition function Q_{MJ} to Sec. 2.2.2. For now, let us revisit the noninteracting system with QVE. Using Eq. (1.17) with $g = 2$, we expand the integrand into a Taylor series in terms of z,

$$
\begin{aligned}
\ln \mathcal{Z} &= 2\frac{1}{2^d}\frac{2}{\Gamma(d/2)}\left(\frac{L}{\sqrt{\pi}}\right)^d \sum_{n=1}^{\infty} z^n \frac{(-1)^{n+1}}{n} \int_0^{\infty} \mathrm{d}k \; k^{d-1} \mathrm{e}^{-n\beta k^2/2} \\
&= 2\left(\frac{L}{\lambda_T}\right)^d \sum_{n=1}^{\infty} z^n \frac{(-1)^{n+1}}{n^{(d+2)/2}},
\end{aligned}
\tag{1.44}
$$

where we used Eq. (1.25) and

$$
\int_0^{\infty} \mathrm{d}x \; x^a \mathrm{e}^{-x^2} = \frac{1}{2} \cdot \Gamma\left(\frac{a+1}{2}\right).
\tag{1.45}
$$

With the single-particle partition function

$$
Q_1 = 2Q_{10} = 2\sum_{\mathbf{k}} \exp\left(-\beta \mathbf{k}^2/2\right) \to 2\left(\frac{L}{2\pi}\right)^3 \int_{-\infty}^{\infty} \mathrm{d}^d k \; \mathrm{e}^{-\beta \mathbf{k}^2/2} = 2\left(\frac{L}{\lambda_T}\right)^d,
\tag{1.46}
$$

the noninteracting virial coefficients are

$$
b_n^{(0)} = \frac{(-1)^{n+1}}{n^{(d+2)/2}},
\tag{1.47}
$$

which is exactly the polylogarithm results we obtained in Eq. (1.24) when expressed in power of z as given by Eq. (1.21) or Eq. (1.22).

Alternatively, we can arrive at the same results using Eq. (1.36) by evaluating the partition function Q_N. It may look trivial and redundant for the noninteracting system, as we have already obtained the analytic series expression for $\ln \mathcal{Z}$. However, it is not always possible (or rather, impossible for most time) to obtain the analytical expression of $\ln \mathcal{Z}$ as in Eq. (1.23) when the interaction is present. In such situations, the standard way is to start with the finite-body system to calculate Q_N (or Q_{MJ}), and use Eq.(1.36) to calculate the virial coefficient.

Taking the calculation of b_2 for example, we need the two-particle partition function $Q_2 =$

$2Q_{20} + Q_{11}$. The second term is trivial in the absence of interaction as the two species are independent, hence

$$Q_{11} = Q_{10} \cdot Q_{01} = Q_{10}^2. \tag{1.48}$$

We should be careful when evaluating Q_{20} as the particles are identical so that we need to take into account the Fermi statistics. This gives us

$$
\begin{aligned}
Q_{20} = \mathrm{tr}_2[e^{-\beta\hat{H}}] &= \frac{1}{2!} \sum_{\mathbf{k}_1\mathbf{k}_2} \langle \mathbf{k}_1\mathbf{k}_2 | e^{-\beta\hat{H}} | \mathbf{k}_1\mathbf{k}_2 \rangle - \langle \mathbf{k}_1\mathbf{k}_2 | e^{-\beta\hat{H}} | \mathbf{k}_2\mathbf{k}_1 \rangle \\
&= \frac{1}{2} \left[Q_{10}^2 - Q_{10}(2\beta) \right],
\end{aligned}
\tag{1.49}
$$

where $Q_{10}(a \cdot \beta)$ is

$$Q_{10}(a \cdot \beta) = \sum_{\mathbf{k}} e^{-a\cdot\beta\mathbf{k}^2/2} \rightarrow \left(\frac{L}{2\pi}\right)^d \int_{-\infty}^{\infty} d^d k \; e^{-a\cdot\beta\mathbf{k}^2/2} = \left(\frac{1}{\sqrt{a}}\right)^d Q_{10}. \tag{1.50}$$

Substituting the above results into Eq.(1.36), we obtained

$$b_2^{(0)} = \frac{2Q_{20} + Q_{11}}{2Q_{10}} - \frac{2Q_{10}}{2} = -\frac{1}{2}Q_{10}(2\beta) = -\frac{1}{2^{5/2}}, \tag{1.51}$$

agreeing with Eq. (1.47). The same procedure can be applied to higher-order terms.

As the noninteracting results are analytically known, we can focused on the interaction-induced changes to b_n, denoted as Δb_n, which describe $\ln[\mathcal{Z}/\mathcal{Z}^{(0)}]$. Similarly, denote the interaction-induced contribution to the canonical partition function as ΔQ_N, Eq. (1.36) now becomes

$$\Delta b_2 = \frac{\Delta Q_2}{Q_1}, \tag{1.52}$$

$$\Delta b_3 = \frac{\Delta Q_3}{Q_1} - \Delta b_2 Q_1, \tag{1.53}$$

$$\Delta b_4 = \frac{\Delta Q_4}{Q_1} - \left[\Delta b_3 + \frac{\Delta(b_2^2)}{2}\right] Q_1 - \Delta b_2 \frac{Q_1^2}{2!}, \tag{1.54}$$

$$\Delta b_5 = \frac{\Delta Q_5}{Q_1} - \Delta(b_4 + b_2 b_3) Q_1 - \Delta\left(b_2^2 + b_3\right) \frac{Q_1^2}{2} - \Delta b_2 \frac{Q_1^3}{3!}, \tag{1.55}$$

where

$$\Delta b_n = b_n - b_n^{(0)}, \tag{1.56}$$

$$\Delta(b_i b_j) = b_i \cdot b_j - b_i^{(0)} \cdot b_j^{(0)} = \Delta b_i \cdot \Delta b_j + \Delta b_i b_j^{(0)} + b_i^{(0)} \Delta b_j. \tag{1.57}$$

1.3.3: Subspace virial coefficients

Until now, we treat particles of different species on the same footing, which is enough for the unpolarized system (also known as spin-balanced system), i.e. the spin-up and spin-down particles have the same chemical potential. However, for the polarized (spin-imbalanced) system, we need to consider the difference between particles of different species in our calculation.

The convention we will use across the dissertation is to denote $\mu_s, s = \uparrow, \downarrow$ as the chemical potential for spin-up/down particles, $\mu = (\mu_\uparrow + \mu_\downarrow)/2$ as the average chemical potential, and $h = (\mu_\uparrow - \mu_\downarrow)/2$ is the polarization.

For finite h, we further decompose Eq. (1.32) and (1.33) into subspace contributions[5],

$$\mathcal{Z} = \sum_{N=0}^{\infty} \sideset{}{'}\sum_{MJ} z_\uparrow^M z_\downarrow^J Q_{MJ}, \tag{1.58}$$

$$\ln \mathcal{Z} = Q_1 \sum_{n=1}^{\infty} \sideset{}{'}\sum_{mj} z_\uparrow^m z_\downarrow^j b_{mj}, \tag{1.59}$$

where $z_s = \exp(\beta \mu_s)$ for $s = \uparrow, \downarrow$.

Following the same procedure as in the unpolarized case, we can express the subspace virial coefficients b_{mj} in terms of the subspace partition function just as we derived in the whole space case. For $n = 4$, we have

$$\Delta b_{31} = \frac{\Delta Q_{31}}{Q_1} - \frac{Q_{10}^2 - Q_{10}(2\beta)}{4Q_{10}} \Delta Q_{11} - \frac{1}{2} \Delta Q_{21} + \frac{Q_{10}}{2} \Delta Q_{11}, \tag{1.60}$$

$$\Delta b_{22} = \frac{\Delta Q_{22}}{Q_1} - \frac{\Delta Q_{11}^2}{4Q_{10}} - \frac{Q_{10}}{2} \Delta Q_{11} - \Delta Q_{21} + Q_{10} \Delta Q_{11}. \tag{1.61}$$

Note that following our definition, we have $\Delta b_4 = 2\Delta b_{31} + \Delta b_{22}$, while some works [21] prefer

---

[5]We used the same convention to use capital subscripts for partition function and lower subscripts for virial coefficients, but they all refer to the same thing, the particle number.

$\Delta b_4 = \Delta b_{31} + \Delta b_{22}/2$. Hence the above equation needs a factor of 2 when compared to their results. Similarly for $n = 5$, we have

$$\Delta b_{41} = \frac{\Delta Q_{41}}{Q_1} - \frac{\Delta Q_{31}}{2} + \left(\frac{Q_1}{4} - \frac{Q_{20}}{Q_1}\right)\Delta Q_{21} + \left(Q_{20} - \frac{Q_{30}}{Q_1} - \frac{Q_1^2}{8}\right)\Delta Q_{11}, \tag{1.62}$$

$$\Delta b_{32} = \frac{\Delta Q_{32}}{Q_1} - \frac{\Delta Q_{31} + \Delta Q_{22}}{2} - \frac{\Delta(Q_{21}Q_{11})}{Q_1} + \left(\frac{3}{4}Q_1 - \frac{Q_{20}}{Q_1}\right)\Delta Q_{21}$$
$$+ \left(Q_{20} - \frac{3}{8}Q_1^2\right)\Delta Q_{11}\,\frac{\Delta(Q_{11}^2)}{2}, \tag{1.63}$$

where we use the same notation as in Eq. (1.56) such that

$$\Delta Q_n = Q_n - Q_n^{(0)}, \tag{1.64}$$

$$\Delta(Q_i Q_j) = Q_i \cdot Q_j - Q_i^{(0)} \cdot Q_j^{(0)} = \Delta Q_i \cdot \Delta Q_j + \Delta Q_i Q_j^{(0)} + Q_i^{(0)}\Delta Q_j. \tag{1.65}$$

Lastly, though we discussed the subspace virial coefficients in the context of spin-polarized systems, they are applicable to the unpolarized system as well. In fact, even in our investigations of the unpolarized systems, we focused on the subspace contribution as well since it allows better control over the extrapolation and management of computational loads.

1.3.4: Virial expansion vs cluster expansion

Before concluding this section, we devote this short paragraph to clarify the ambiguity between the term "virial expansion" and "cluster expansion". Initially, the QVE inherits the same definition from the classical virial expansion, i.e. expand the pressure (and hence the GCPF) in terms of the density as

$$\beta P = n\left[1 + nB_2(T) + n^2 B_3(T) + \dots\right], \tag{1.66}$$

where $B_n(T)$ are the *original* virial coefficients.

The virial expansion we used here was then called either fugacity expansion or as cluster expansion, which is related to Mayer's cluster integrals [22, 23] (see also Ref. [20]). For such historical reasons, the ambiguous terminology may still be used in modern works. Throughout this dissertation, the QVE will be used only to refer the fugacity expansion.

Section 1.4: Existing works on QVE for the interacting Fermi gas

Before leaving this chapter, let us take a short detour to review existing theoretical and experimental works related to QVE for interacting Fermi gas. For more detailed discussions, see e.g. Ref. [24].[6]

1.4.1: Second-order virial coefficient Δb_2

As the first step towards the investigation of QVE, the study of second-order virial coefficient can date back to more than 80 years ago. In 1930s, Beth and Uhlenbeck analytically calculated the second-order virial coefficient b_2 in terms of binding energy and scattering phase shift, which describe the two-particle interaction properties.

Their work is later known as Beth-Uhlenbeck formula, relating the virial coefficient and scattering properties. For a spin-1/2 Fermi gas in 3D, there is

$$\Delta b_2 = \sqrt{2} \sum_i e^{-\beta E_B^i} + \sqrt{2} \sum_l \frac{2l+1}{\pi} \int_0^\infty \mathrm{d}p \frac{\mathrm{d}\delta_l}{\mathrm{d}p} e^{-\frac{\lambda_T^2 p^2}{2\pi}}, \tag{1.67}$$

where the first summation is over all bound states, the second summation is over all partial waves, and δ_l is the phase shift of each partial wave.

The above expression can be applied in different dimensions and expressed in parameters of the corresponding effective range expansion as shown in Eq. 1.1 (i.e., scattering length, effective range, etc.). For a zero-range interaction (see, e.g., Ref. [26, 27] for results in 1D, Ref. [28–33] for 2D, and Ref. [34] for 3D):

$$\Delta b_2^{1D} = -\frac{1}{2\sqrt{2}} + \frac{e^{\lambda_1^2/4}}{2\sqrt{2}} \left[1 + \mathrm{erf}(\lambda_1/2) \right], \tag{1.68}$$

$$\Delta b_2^{2D} = e^{\lambda_2^2} - 2 \int_0^\infty \frac{\mathrm{d}p}{p} \frac{2e^{-\lambda_2^2 p^2}}{\pi^2 + 4\ln^2(p^2)}, \tag{1.69}$$

$$\Delta b_2^{3D} = \frac{e^{\lambda_3^2}}{\sqrt{2}} \left[1 + \mathrm{erf}(\lambda_3) \right], \tag{1.70}$$

---

[6]This section is partly based on works published in Ref. [25]

where λ_d is the physical coupling strength in d dimensions, defined as

$$
\begin{aligned}
\lambda_1 &= 2\frac{\sqrt{\beta}}{a_0}, \\
\lambda_2 &= \sqrt{\beta E_B}, \\
\lambda_3 &= \frac{\sqrt{\beta}}{a_0},
\end{aligned}
\tag{1.71}
$$

where a_0 is the s-wave scattering length and E_B is the binding energy of the single two-body bound state of the 2D case.

The above results are sufficient descriptions for ultracold atoms, for which the zero-range model interaction is a precise approximation. However, for systems like neutron matter or more complicated nuclear matter, the scattering properties are much richer and require more parameters such as a non-zero effective range and/or other angular momentum channels.

For pure neutron matter, Refs. [12, 35] integrate by parts to rewrite the Beth–Uhlenbeck result as

$$
\Delta b_2 = \frac{1}{2^{1/2}\pi T} \int_0^\infty dE \; e^{-\beta E/2} \delta_{\text{neutrons}}^{\text{tot}}(E),
\tag{1.72}
$$

where $\delta_{\text{neutrons}}^{\text{tot}}(E)$ is the sum of all the scattering phase shifts at laboratory energy E, whose contributions from different angular momentum channels enter as

$$
\delta_{\text{neutrons}}^{\text{tot}}(E) = \sum_{S,L,J} (2J+1)\delta_{{}^{2S+1}L_J}(E),
\tag{1.73}
$$

where the partial wave terms $\delta_{{}^{2S+1}L_J}(E)$ are obtained from partial wave analyses of experimental data such as Nijmegen's [36].

For nuclear matter, on the other hand, one must account for the deuteron bound state, such that

$$
\Delta b_2 = \frac{3}{2^{1/2}} \left(e^{E_d/T} - 1 \right) + \frac{1}{2^{3/2}\pi T} \int_0^\infty dE \; e^{-\beta E/2} \delta_{\text{nuc}}^{\text{tot}}(E),
\tag{1.74}
$$

where E_d is the binding energy of the deuteron and the -1 term comes from partial integration when accounting for the phase shift at zero energy being π times the number of bound states

(see also Ref. [37]). The work of Ref. [12, 35] also analyzed the contributions due to pure alpha-particle scattering and nucleon-alpha scattering, thus obtaining all possible contributions to the second-order QVE for nuclear matter composed of neutrons, protons, and alpha particles.

These analytic works for the second-order virial coefficients offered a benchmark and, more importantly, the reference to renormalize the effective model.We will discuss more about the renormalization process in Sec. 2.2.4.

1.4.2: Third-order virial coefficient Δb_3

Since the pioneering work by Beth and Uhlenbeck on Δb_2, the community started to work on the next term in the ladder, see early works e.g. Refs.[38–40]. However, it took nearly 70 years until finally in the 2000s the community established a conclusive accurate estimation of Δb_3, with the help of modern numerical solution and powerful theoretical tools such as diagrammatic expansions.

Impressive exact analytic progress has been made by notable works of Leyronas [41], Kaplan and Sun [42], and Castin and colleagues [43–45], as well as the large effective range expansion of Ngampruetikorn et al. [46] (see also the early work of Ref. [47] focusing on the unitary limit). Readers may also be interested in Ref. [48, 49], which attacked this problem from different angles: in Ref. [48], authors used the harmonic approximation for the inter-particle interaction, and Ref. [49] followed and extended Lee and Yang's cluster expansion method [50–53].

Leyronas organizes the calculation of Δb_n around the QVE of the density equation of state, itself expressed as an integral over all momenta of the equal-time single-particle Green's function in momentum space (i.e., the momentum distribution). Diagrams of various types are then identified at each order in z (up to order z^3), where contributions from the two- and three-body T matrix appear (the latter describing the atom-dimer scattering). The resulting time integrals are converted into energy integrals, which are then evaluated analytically where possible and otherwise numerically. The resulting approach is thus for the most part analytic and in principle exact and is in remarkable agreement in the unitary limit with prior purely numerical results for b_3 [54].

Other diagrammatic approaches also made interesting contributions. The work of Kaplan and Sun [42], which preceded Leyronas, starts from the density equation-of-state written as a momentum integral over the single-particle Green's function (as Leyronas does), but rather than carrying

out the Matsubara sum from the outset, it uses a Poisson summation to express the propagator directly as a power series in z. The latter is then interpreted as a sum over the winding number of worldlines around the compact imaginary time direction. The diagrams associated with each term in that expansion are referred to as "chronographs". Adding the contributions from such chronographs and accounting for systematic effects by extrapolation, very good agreement with prior numerical results [54] for b_3 was obtained in the unitary limit.

Ngampruetikorn et al. [46] used an expansion around large effective range r_e (compared to the thermal wavelength λ_T), which allows them to examine up to the four-particle subspace diagrammatically, thus obtaining numerical estimates for up to Δb_4. They focused on the unitary Fermi gas by interpolating between $R^* \gg \lambda_T$ and $\lambda_T/|a| \gg 1$, where a is the scattering length, and applied their method to the pressure, density, entropy, and spectral functions. Their interpolation results for Δb_3 and Δb_4 at unitarity agree with those obtained by other groups, including those presented here. In Ref. [30], Ngampruetikorn et al. also studied the pairing correlations of the 2D Fermi gas up to third order in the virial expansion, additionally obtaining Tan contact (we return to the expansion of this and other quantities below).

In Ref. [55], Werner and Castin analyzed the $(2+1)$-body problem of harmonically trapped spin-1/2 fermions at unitarity. They analytically solved the system and obtain the exact spectrum and eigenstates.

On the numerical side, some of the early works used exact diagonalization in hyperspherical coordinates [54, 56], whereby a large number of eigenstates can be calculated and their energies summed over to calculate canonical partition functions, thus providing access to b_3 (and to some extent b_4, and with low accuracy b_5) for systems of cold atoms with short-range interactions.

In spite of all of the above remarkable progress, it is evident that, due to the complexity of the n-particle quantum mechanical problem, a different kind of approach is needed if one is to determine high-order virial coefficients with well-controlled systematic error. In particular, stochastic methods tend to have too large uncertainties to yield the accurate estimates, which could be fatal to the resummation techniques as will be discussed in Sec. 2.4. On the other hand, direct numerical methods such as exact diagonalization can be very powerful in providing detailed information (furnishing not only energies but also the associated eigenstates), but have not yet succeeded in accurately determining virial coefficients beyond the third order. One of the main objectives of

this dissertation is to present our work on developing a non-perturbative, semi-analytic, computational approach that is free of stochastic effects, as well as its applications in various systems and on different physical quantities.

1.4.3: Fourth-order virial coefficient Δb_4 and beyond

The calculation of Δb_4 is even more challenging as it requires studying a four-particle system, which includes two subspaces. All existing works focused on the Δb_4 at the unitary limit and there are large discrepancies especially between the experimental measurements and theoretical calculations.

On the theoretical side, multiple groups contribute using diagrammatic approaches. In the same work [46], Ngampruetikorn *et al.* examined the four-particle subspace as well, and obtained estimates $\Delta b_4 = 0.06$. Endo and Castin [43, 44] (see also Ref. [45]) generalized their work on Δb_3 to the problem of (3+1) and (2+2) particles, and calculated the value of Δb_4 as a function of the trapping frequency $\beta\omega$ and obtained $\Delta b_4 = 0.062$. As we will show in Sec. 5.3.1, our non-perturbative determination turned out to be in remarkable agreement with their result, which they considered to be only a conjecture.

Along the line of stochastic method, a notable work is the calculation by Yan and Blume [21, 57], where they designed an *ad hoc* Monte Carlo method to tackle the calculation of Δb_4 for fermions at unitarity, resulting in the first determination of this quantity with stochastic methods. Their calculation featured a harmonic trapping potential, which induces a temperature dependence in Δb_4. To obtain the temperature-independent value of Δb_4 in the unitary limit, they performed a high-temperature extrapolation to extrapolate the results to the $\beta\omega \to 0$ limit, introducing an extra source of systematic error. The only important drawback of this work was the large uncertainty in the final result, induced by the increased stochastic noise as the trapping potential is removed. We will revisit this issue later in Sec. 5.3.1.

Rakshit et al. [56] gave predictions based on the energy spectra of a trapped system. They extrapolated the coefficients to the high-temperature limit $\beta\omega \to 0$ based on the low-lying portion of the excitation spectra, and obtained negative prediction $\Delta b_4 = -0.016(4)$. For other works, see e.g. Ref. [58–60].

On the experimental side, groups from MIT [61] and ENS [62] determined b_4 based on the

measurement of pressure or density. For example, the MIT group directly measured the local density and the pressure can then be reconstructed by integrating the local density over the trapping potential. In terms of the virial coefficient, as shown in Eq. (1.27), the pressure is written as

$$\beta P \lambda_T^3 / 2 = b_1 z + b_2 z^2 + b_3 z^3 + b_4 b^4 + \mathcal{O}(z^5), \tag{1.75}$$

where $b_1 = 1$, $b_2 = 3\sqrt{2}/8$ are known exactly and the authors used $b_3 = -0.29095295$ from Ref. [54]. The higher-order terms $\mathcal{O}(z^5)$ is assumed to be negligible, and b_4 is obtained by fitting to the reconstructed pressure, which yields the prediction $b_4 = 0.065(10)$, or equivalently $\Delta b_4 = 0.096(10)$. The ENS group used a similar procedure except that they directly measured the local pressure $P(\mu, T)$, and fitted both Δb_3 and Δb_4 to the ratio P/P_{free}. They obtained a very close estimation $\Delta b_4 = 0.096(15)$[7].

The agreement between the experimental determination is not a big surprise considering the accurate pressure measurement in both experiments and the accurate results at the third order. As we will show later, the true culprit behind the discrepancy between the experimental determination and theoretical calculation is that the fifth-order contribution is actually not negligible. In fact, it is positive, the same sign as the fourth-order, and has comparable magnitude to that of the fourth order, which explains the overestimates from the experiments.

Beyond fourth-order coefficient, the existing results are even more limited. In the same work [56], Rakshit *et al* predicted $\Delta b_5 \in [0.0017, 0.101]$ and the sign of b_n at low temperature follows $+, -, -, +, +, -, -, +, +, \ldots$ for $n = 2, 3, 4, 5, 6, 7, 8, 9, 10, \ldots$. In Refs [63, 64], Bhaduri et al. proposed an ansatz

$$\Delta b_n = (-1)^n \frac{\Delta b_2}{2^{(n-1)(n-2)/2}}, \tag{1.76}$$

which is based on their conjecture of n-body cluster in terms of two-body systems.

As will be further explained later, one main drawback of the conjectures is that they are based on the properties of n-body system, while our results demonstrate that the competition between the subsystems plays an important role in Δb_n, and therefore it will be more accurate to conjec-

---

[7]Their fitted results yielded $\Delta b_3 = -0.35(2)$, agreeing very well with expected $\Delta b_3 = -0.355$.

ture for the subspace contribution Δb_{mj}.

Section 1.5:   Dissertation overview

This dissertation is mainly based on the following published works:

1. *Leading- and next-to-leading-order semiclassical approximation to the first seven virial coefficients of spin-1/2 fermions across spatial dimensions*, **Hou, Y.**, Czejdo, A. J., DeChant, J., Shill, C. R. and Drut, J. E., Physical Review A, **100**, 6, 063627 (2019)

2. *Fourth- and fifth-order virial coefficients from weak coupling to unitarity*, **Hou, Y.** and Drut, J. E., Physical Review Letters, **125**, 5, 050403 (2020)

3. *Virial expansion of attractively interacting fermi gases in one, two, and three dimensions, up to fifth order*, **Hou, Y.** and Drut, J. E. Physical Review A, **102**, 3, 033319 (2020)

4. *Fourth- and fifth-order virial expansion of harmonically trapped fermions at unitarity*, **Hou, Y.**, Morrell, K. J., Czejdo, A. J. and Drut, J. E., Physical Review Research, **3**, 3, 033099 (2021)

5. *Toward an automated-algebra framework for high orders in the virial expansion of quantum matter*, Czejdo, A. J., Drut, J. E., **Hou, Y.**, and Morrell, K. J., Condensed Matter, **7**, 1, 13 (2022)[8]

Several sections are partially related to the following published works

1. *Virial coefficients of trapped and untrapped three-component fermions with three-body forces in arbitrary spatial dimensions*, Czejdo, A. J., Drut, J. E., **Hou, Y.**, McKenney, J. R. and Morrell, K. J., Physical Review A, **101**, 6, 063630 (2020)

2. *Pairing and the spin susceptibility of the polarized unitary fermi gas in the normal phase*, Rammelmüller, L., **Hou, Y.**, Drut, J. E. and Braun, J., Physical Review A, **103**, 4, 043330 (2021)

---

[8]Authors are in the alphabetic order

This dissertation is organized as follow: Chap. 2 focuses on the methodology, where we briefly review the conventional methods and the motivations behind the development of the automated-algebra methods. In Chap. 3 and Chap. 4, we apply the automated-algebra method to homogeneous Fermi gas. Chap. 3 is exclusively devoted to the Unitary Fermi gas while Chap. 4 focuses on the general settings for arbitrary coupling strength across the BCS-BEC crossover and in different dimensions. Chap. 5 discusses the harmonically trapped Fermi gases, for which we generalized of automated-algebra method to the coordinate space. Chap. 6 concludes the dissertation and presents the outlook for the automated-algebra framework.

CHAPTER 2:   Computational methods: Automated-algebra framework

In this chapter, we focus on the technical aspects. We start with a detour to a brief review on the existing methods that are widely applied for quantum many-body problems. We particularly focus on the Quantum Monte Carlo method to introduce several important concepts such as the Trotter-Suzuki decomposition and the Hubbard-Stratonovich transformations. After the review, we dive into the formalism and technical details of the so-called automated-algebra method.

Section 2.1:   Review of existing computational methods

Before starting this section, we would like to clarify that this section is definitely not a exhaustive review on methods for Quantum Many-body problems. Rather, its aim is to offer more contexts to establish the foundation for better analysis of the automated-algebra method presented later.

Roughly speaking, the computational methods for the quantum many-body problem could be categorized into two classes: the direct ones (also called memory-intensive) vs the stochastic ones (or statistical-intensive), and the criterion is whether the statistical sampling is used. The common examples of the first type are the exact diagonalization (see e.g. [65, 66]) and the coupled cluster methods (see e.g. [67, 68]). Though taking the advantages such as "exact" accuracy and free from numerical analytic continuation, such methods are extremely memory-hungry due to the exponential growth of the Hilbert space dimension as the size of system increases, i.e. the "curse of dimensionality doom".

In dealing with the growing memory requirement, the second type of methods takes a different route by incorporating the statistical samplings, rather than work directly in the complete Fock space. The most prominent example of this type is the Quantum Monte Carlo (QMC) method. The QMC is not the name of a single method, but rather refers to a set of techniques that incorporate the Monte Carlo method into quantum systems. Depending on the formalism, there are multiple variations in the big QMC family such as Variational QMC [69, 70], path-integral QMC [71], hybrid QMC [72] and so on.

Here, we will focus on one kind called Determinant QMC (DQMC) to introduce several common concepts and demonstrate the challenges encountered by the conventional numerical methods. For more details of QMC method, see e.g. Ref. [73].

The essential principle of QMC is the same as its classical counterpart. Assume we have a given quantity also denoted as $\mathcal{Z}$, and it can be written as

$$\mathcal{Z} = \sum_{\mathbf{n}} \mathcal{P}_{\mathbf{n}} \text{ or } \mathcal{Z} = \int \mathrm{d}^d\mathbf{n} \; \mathcal{P}(\mathbf{n}), \tag{2.1}$$

where $\sum_{\mathbf{n}}$ or $\int \mathrm{d}^d\mathbf{n}$ is over all possible configurations and $\mathcal{P}(\mathbf{n})$ is any semi-positive function at the corresponding configuration $\mathbf{n}$, i.e. probability measure (again, with proper normalization). Using the Monte Carlo method, we could estimate this quantity by randomly sampling a large number of configurations $\mathbf{n}$ and taking the average.

In our case, in order to estimate the GCPF, we rewrite it in form of

$$\mathcal{Z} = \mathrm{Tr}_F[\mathrm{e}^{-\beta(\hat{H}-\mu\hat{N})}] = \int \mathcal{D}\sigma \mathrm{e}^{-S[\sigma]}. \tag{2.2}$$

Now the integrand $\mathrm{e}^{-S[\sigma]}$ plays the role of probability measure (with proper normalization), and our goal is now to find the proper form of $S[\sigma]$. To express the GCPF into this desired form, we introduce two techniques: the Trotter-Suzuki decomposition and the Hubbard-Stratonovich transformation.

At first, we would like to "decouple" the kinetic operator $\hat{T}$ and interaction operator $\hat{V}$ as they usually belong to different eigenspace. To decompose the exponential operator $\exp\left[-\tau(\hat{A}+\hat{B})\right]$ properly, we use the Trotter-Suzuki decomposition

$$\mathrm{e}^{-\tau(\hat{A}+\hat{B})} = \mathrm{e}^{-\tau\hat{A}/2}\mathrm{e}^{-\tau\hat{B}}\mathrm{e}^{-\tau\hat{A}/2} + \mathcal{O}(\tau^3). \tag{2.3}$$

With a small τ, the Suzuki-Trotter decomposition can approximate the quantum effect with relatively small error. In our case, we firstly discretize β into N_τ slices such that $\tau = \beta/N_\tau$ is a small

quantity, where τ is now the imaginary time spacing. We can then write

$$\mathrm{e}^{-\beta\hat{H}} = \prod_{\tau} \mathrm{e}^{-\tau(\hat{T}+\hat{V})} = \prod_{\tau} \mathrm{e}^{-\tau\hat{T}/2}\mathrm{e}^{-\tau\hat{V}}\mathrm{e}^{-\tau\hat{T}/2}. \tag{2.4}$$

Higher-order decomposition are also available [74], while in most cases, the leading order formula with small τ is accurate enough as the decomposition error is insignificant compared to other sources such as statistical error from sampling.

Now we have successfully decoupled the two operators but it remains that $\hat{T}$ is a single-body operator while $\hat{V}$ is a two-body operator (or n-body operator in general). The next step is to transform operator $\hat{V}$ into decoupled single-particle operators so that we can work uniformly in the single-body space.

To this end, the conventional technique is the Hubbard-Stratonovich (HS) transformation [75, 76], which is originally defined through the identity

$$\exp\left(-\frac{x^2}{2}\right) = \sqrt{\frac{1}{2\pi a}} \int_{-\infty}^{\infty} \mathrm{d}y \ \exp\left[-\frac{y^2}{2a} - ixy\right], \tag{2.5}$$

where the x^2 term in the LHS plays the role of our two-body operator, i.e. x can be interpreted as the density operator, and y is the newly-introduced "auxiliary field". From a physical standpoint, the above transformation convert a system with two-body inter-particle interaction into a noninteracting system coupled to a auxiliary field[1].

Though this original form is still being widely used, evaluating an unbound integral is not a cheap operation. Therefore, later research propose more choices (see e.g. Refs. [73, 78]) to decouple $\hat{V}$ operator. Here we use the broader definition and call all of them the HS transformation, and specifically, we will use the bounded continuous version as

$$\exp(\tau g\hat{n}_\uparrow\hat{n}_\downarrow) = \int_{-\pi}^{\pi} \frac{\mathrm{d}\sigma}{2\pi}(1 + A\sin\sigma\hat{n}_\uparrow)(1 + A\sin\sigma\hat{n}_\downarrow), \tag{2.6}$$

where $A = \sqrt{2(\mathrm{e}^{\tau g} - 1)}$.

After applying the TS decomposition and HS transformation, we end up with GCPF expressed

---

[1]Though we consider only the two-body contact interaction, the Hubbard-Stratonovich transformation could be generalized to the arbitrary many-body case, see e.g. Ref. [77]

in the form as in Eq.(2.2).

$$\mathcal{Z} = \int \mathcal{D}\sigma e^{-S_{\text{eff}}[\sigma]}, \tag{2.7}$$

where $\mathcal{D}\sigma$ is the path integral over all possible configurations of the field σ, and $S[\sigma] = S_{\text{eff}}[\phi]$ now takes the physical meaning of the effective action. It can be shown that

$$e^{-S_{\text{eff}}[\sigma]} = \det M_{\uparrow}[\sigma] \det M_{\downarrow}[\sigma], \tag{2.8}$$

where M_s is called fermion matrix for each species. The "canonical" definition of the Fermion matrix is

$$\mathcal{M} = \begin{pmatrix} \mathbb{1} & 0 & 0 & 0 & \cdots & \mathcal{U}_{N_\tau} \\ -\mathcal{U}_1 & \mathbb{1} & 0 & 0 & \cdots & 0 \\ 0 & -\mathcal{U}_2 & \mathbb{1} & 0 & \cdots & 0 \\ \vdots & \vdots & \vdots & \ddots & \vdots & \vdots \\ 0 & 0 & \cdots & -\mathcal{U}_{N_\tau-2} & \mathbb{1} & 0 \\ 0 & 0 & 0 & \cdots & -\mathcal{U}_{N_\tau-1} & \mathbb{1} \end{pmatrix}, \tag{2.9}$$

where we omit the subscript s for spin species and $\mathcal{U}_i$ is the decomposed and transformed i^{th} slice defined as

$$[\mathcal{U}_i]_{jk} = \langle \mathbf{p}_j | \exp\left(-\frac{\tau}{2}\hat{T}\right)(1 + A\sin\sigma_i\hat{n})\exp\left(-\frac{\tau}{2}\hat{T}\right)|\mathbf{p}_k\rangle \equiv \mathcal{T}\mathcal{V}_i[\sigma]\mathcal{T} \tag{2.10}$$

Alternatively, it can be demonstrated that the $\det \mathcal{M}$ can be written as

$$\det \mathcal{M} = \det(\mathbb{1} + \mathcal{U}) = \det(\mathbb{1} + \mathcal{U}_{N_\tau}\mathcal{U}_{N_\tau-1}\cdots\mathcal{U}_1). \tag{2.11}$$

Note that we did not consider the contribution from operator $\exp\left(\beta\mu\hat{N}\right)$ as it yields just the fugacity z in the single-body space. We omit it from the above expressions for clarity and in prac-

tice we absorb the fugacity into kinetic matrix, i.e.

$$\mathcal{T} = \exp\left(-\frac{\tau}{2}\frac{\mathbf{p}^2}{2}\right)\exp\left(\frac{\tau\mu}{2}\right). \tag{2.12}$$

Lastly, to evaluate the path integral on a computer, coordinates are also discretized into a d-dimensional lattice of size N_x^d with lattice spacing ℓ, which is set to one by convention and defines the lattice unit. The lattice parameters are required to satisfy $1 = \ell \ll \lambda_T \ll N_x$ to "fit" the system properly. The lattice spacing ℓ imposes an ultraviolet cutoff in the momentum space $\Lambda \propto \ell^{-1}$ in lattice units, and the lattice size N_x discretizes the momentum in units of $2\pi/N_x$ and represents an infrared cutoff.

Such finite lattice can also be regarded as a cutoff of Fock space. However, in the ultracold regime, the low-lying states contribute dominantly and the effects are expected not to change the physics qualitatively. With finite lattice results, the result in the thermodynamic limit can be obtained by extrapolation.

One of the greatest challenge inhibiting the wide application of QMC is the infamous sign problem. In the previous section, we claimed that the $\exp(-S_{\text{eff}})$ can be treated as probability measure. However, as in Eq. (2.8), the product of determinants is not guaranteed to be semi-positive for all σ configurations. When the sign of $\mathcal{P}[\sigma]$ depends on σ, the interpretation as probability measure is no longer valid, which is why the issue is called (minus) sign problem. More generally, $\mathcal{P}[\sigma]$ can even be complex (for example, when the Hamiltonian is complex) and hence the sign problem is actually a special case of a more general problem called complex phase problem.

In the presence of sign problem, the contributions with different sign will cancel each other out, leading to exponential calculation time. In this sense, the sign problem can be regarded as a signal-to-noise issue. The sign problem is common in many systems of physical interests, such as the imbalanced [79, 80] or repulsively interacting fermions, as well as finite-density QCD [81], the sign problem emerges and severely limits the application of QMC.

The sign problem has been proven to be NP-hard [82], which means no polynomial time method exists in the presence of sign problem. To mitigate the sign problem, many methods has been developed, such as the "naive" reweighting method [83] or the more recent Fermion's bag approach [84].

In some situations, it is also possible to circumvent the sign problem by taking a different representation, such as by using the Majorana representation [85]. For a more comprehensive review, see e.g. Ref. [86]. Another direction is to turn to alternative methods that does not depend on the probabilistic interpretation. One example is the complex Langevin which has been successfully applied in fields of both QCD and condensed matter. For more details on complex Langevin as well as other approaches for the sign problem, see e.g. Ref. [87].

Besides the theoretical obstacles like the sign problem, some practical issues related to the Fermion determinant are also inhibiting the wide application of QMC. We present two forms of the Fermion determinant in Eq. (2.9) (sparse version) and (2.11) (compact version), and both forms have their own pros and cons. Compared to the sparse matrix $\mathcal{M}$, the compact matrix $1+\mathcal{U}$ is better-conditioned and more memory economical. However, it is more complicated to calculate the term $\delta M/\delta\sigma$, which is required in calculation some observables, using the compact form than the sparse matrix, since the derivative of the product of $\mathcal{U}_i$s yields a series of length N_τ. Moreover, the product of the long sequence matrices is numerically unstable. Though it is possible to stabilize the product by incorporating rank-revealing decomposition such as the singular value decomposition (SVD) or QR decomposition [88, 89], whose idea is to align the number by order such that the multiplication results remains exact with in the machine precision, the huge expense of the rank-revealing decomposition hinders its application in large scale simulation.

Another issue related to the fermion matrix arises when simulating in large lattice, which is important for understanding the extrapolation to thermodynamic limit and the finite size effect. In QMC methods, one computationally expensive step is the inverse of fermion matrix M^{-1}. The direct method is to calculate the explicit form of M^{-1} using LU decomposition, scaling as cubic of the matrix size, namely $\mathcal{O}[(N_x^d N_\tau)^3]$. It is therefore impractical to apply the direct method in large lattice. The limited memory is another reason why direct inversion is not the optimal choice for simulation in large lattice. The LU decomposition requires the storage of two matrices of the same size as the fermion matrix. As the simulation usually consists of dozens or even hundreds of jobs in parallel, the direct inversion will swallow up the memory in no time. One possible solution is to treat the problem as a linear problem, instead of trying to find the explicit form of M^{-1}.

Section 2.2:   Automated-algebra method

2.2.1:   From QMC to Automated-Algebra

In the last section, we discussed several general limitations of QMC. In the context of QVE, there is another specific issue rooting from the statistical sampling errors. Due to the decreasing order of magnitude and dedicated volume cancellations, it is very expensive to apply QMC, when it is applicable, to evaluate higher-order virial coefficients. Moreover, due to its numerical nature, one has to repeat the calculations to cover different parameters, or in other words, it is a kind of "discrete method". Even though a natural remedy to all the three issues above is to turn to analytic method, analytic solutions for n-body systems with $n > 3$ are extremely difficult, if not impossible.

In between the purely numerical and purely analytical method, a balance may be struck by developing a semi-analytic method whose results, though still rely on complicated numerical methods for evaluation, are essentially analytical expressions.

To evaluate the partition function, we also use the TS decomposition, the same as in the QMC.

However, as it is much more expensive to perform the analytic evaluation, the calculations are usually limited small N_τ, resulting into a larger decomposition error (or physically, a larger truncation error when neglecting certain quantum effects). In a pilot work [90] (see also Sec. 4.1), the authors found qualitative agreement between the QMC results and semiclassical results, i.e. using $N_\tau = 1$ in the TS decomposition. This success inspires us to explore the results at larger N_τ. But to deal with the sheer increase in computational costs, we aim to develop a method to automatically evaluate the above algebraic expression, which is also inspired by an early work by our group on the automated perturbation theory [27].

As there is no need to rewrite the partition function as probability integral, no HS transformation is required. Instead, we express the Hilbert trace explicitly as

$$Q_N = \mathrm{tr}_N\left[\exp\left(-\beta\hat{H}\right)\right] = \mathrm{tr}_N\left[\prod_{N_\tau}\exp\left(-\tau\hat{T}\right)\exp\left(-\tau\hat{V}\right)\right], \tag{2.13}$$

where the cyclic property of trace is used, and insert a series of complete sets $|\mathbf{X}\rangle\langle\mathbf{X}|$ or $|\mathbf{P}\rangle\langle\mathbf{P}|$ to

project operator into their eigenspace, where the capital states refers to a set of all particles, i.e.

$$\mathbf{P} = \{\mathbf{p}_1, \mathbf{p}_2, \cdots \mathbf{p}_M, \mathbf{p}_{M+1}, \cdots \mathbf{p}_{M+J}\}. \tag{2.14}$$

The partition function is now explicitly expressed as

$$
\begin{aligned}
Q_N &= \mathrm{tr}_N \left[\prod_{N_\tau} \exp\left(-\tau \hat{T}\right) \exp\left(-\tau \hat{V}\right) \right] \\
&= \sum_{\mathbf{P}^{(1)}} \left\langle \mathbf{P}^{(1)} \left| \prod_{N_\tau} \exp\left(-\tau \hat{T}\right) \exp\left(-\tau \hat{V}\right) \right| \mathbf{P}^{(1)} \right\rangle \\
&= \sum_{\{\mathbf{P}\}} \sum_{\{\mathbf{X}\}} \epsilon[\mathbf{P}^{(1)}] \left\langle \mathbf{P}^{(1)} \middle| \mathbf{X}^{(1)} \right\rangle V[\mathbf{X}^{(1)}] \left\langle \mathbf{X}^{(1)} \middle| \mathbf{P}^{(2)} \right\rangle \\
&\qquad \times \epsilon[\mathbf{P}^{(2)}] \left\langle \mathbf{P}^{(2)} \middle| \mathbf{X}^{(2)} \right\rangle V[\mathbf{X}^{(2)}] \left\langle \mathbf{X}^{(2)} \middle| \mathbf{P}^{(3)} \right\rangle \\
&\qquad \times \dots \epsilon[\mathbf{P}^{(N_\tau)}] \left\langle \mathbf{P}^{(N_\tau)} \middle| \mathbf{X}^{(N_\tau)} \right\rangle V[\mathbf{X}^{(N_\tau)}] \left\langle \mathbf{X}^{(N_\tau)} \middle| \mathbf{P}^{(1)} \right\rangle .
\end{aligned}
\tag{2.15}
$$

Reordering the terms, we have

$$Q_N = \sum_{\{\mathbf{P}\}} \epsilon[\mathbf{P}^{(1)}] \epsilon[\mathbf{P}^{(2)}] \cdots \epsilon[\mathbf{P}^{(N_\tau)}] \sum_{\{\mathbf{X}\}} \left\langle \mathbf{P}^{(1)} \middle| \mathbf{X}^{(1)} \right\rangle V[\mathbf{X}^{(1)}] \left\langle \mathbf{X}^{(1)} \middle| \mathbf{P}^{(2)} \right\rangle \cdots . \tag{2.16}$$

The first part is summing over all momentum variables and $\epsilon[\mathbf{P}]$ is the free-space propagator

$$\epsilon[\mathbf{P}] = \exp\left(-\tau \sum_{i=1}^{n} \mathbf{p}_i^2\right). \tag{2.17}$$

The second part sums over all coordinate space, which is to calculate the representation of $\hat{V}$ in the momentum representation, i.e. $\left\langle \mathbf{P}^{(i)} \middle| \hat{V} \middle| \mathbf{P}^{(j)} \right\rangle$.

The wavefunction $\langle \mathbf{X} | \mathbf{P} \rangle$ is given by the Slater determinant, i.e.

$$\langle \mathbf{X} | \mathbf{P} \rangle = \sqrt{\frac{1}{N!}} \sqrt{\frac{1}{V^N}} \begin{vmatrix} e^{i\mathbf{x}_1 \mathbf{p}_1} & e^{i\mathbf{x}_1 \mathbf{p}_2} & \cdots \\ e^{i\mathbf{x}_2 \mathbf{p}_1} & e^{i\mathbf{x}_2 \mathbf{p}_2} & \cdots \\ \vdots & \vdots & \ddots \end{vmatrix}_M \begin{vmatrix} e^{i\mathbf{x}_{M+1} \mathbf{p}_{M+1}} & e^{i\mathbf{x}_{M+1} \mathbf{p}_{M+2}} & \cdots \\ e^{i\mathbf{x}_{M+2} \mathbf{p}_{M+1}} & e^{i\mathbf{x}_{M+2} \mathbf{p}_{M+2}} & \cdots \\ \vdots & \vdots & \ddots \end{vmatrix}_J , \tag{2.18}$$

and the interaction matrix $V[\mathbf{X}]$ is in form of

$$V[\mathbf{X}] = \langle \mathbf{X}|\exp\left(-\tau\hat{V}\right)|\mathbf{X}\rangle = \langle \mathbf{X}|\exp(\tau g\hat{n}_\uparrow\hat{n}_\downarrow)|\mathbf{X}\rangle = \langle \mathbf{X}|\prod_{\mathbf{x}}\exp[\tau g\hat{n}_\uparrow(\mathbf{x})\hat{n}_\downarrow(\mathbf{x})]|\mathbf{X}\rangle \qquad (2.19)$$

where we used the density operator in the coordinate space $\hat{n}_s = \prod_{\mathbf{x}}\hat{n}_s(x)$. Expanding the operator $\exp[\tau g\hat{n}_\uparrow(\mathbf{x})\hat{n}_\downarrow(\mathbf{x})]$, we obtain

$$\begin{aligned}\exp[\tau g\hat{n}_\uparrow(\mathbf{x})\hat{n}_\downarrow(\mathbf{x})] &=1 + \tau g\hat{n}_\uparrow(\mathbf{x})\hat{n}_\downarrow(\mathbf{x}) + \frac{(\tau g)^2}{2!}\hat{n}_\uparrow(\mathbf{x})\hat{n}_\downarrow(\mathbf{x}) + \dots \\ &=1 + C\hat{n}_\uparrow(\mathbf{x})\hat{n}_\downarrow(\mathbf{x}),\end{aligned} \qquad (2.20)$$

where C is also referred as bare coupling and defined as

$$C = \exp(\tau g) - 1. \qquad (2.21)$$

The product now becomes

$$\prod_{\mathbf{x}}[1 + C\hat{n}_\uparrow(\mathbf{x})\hat{n}_\downarrow(\mathbf{x})] = 1 + C\sum_{\mathbf{x}}\hat{n}_\uparrow(\mathbf{x})\hat{n}_\downarrow(\mathbf{x}) + C^2\sum_{\mathbf{x}\neq\mathbf{x}'}{}'\hat{n}_\uparrow(\mathbf{x})\hat{n}_\downarrow(\mathbf{x})\hat{n}_\uparrow(\mathbf{x}')\hat{n}_\downarrow(\mathbf{x}') + \dots \quad (2.22)$$

where the primed summation is the result of the Pauli exclusion principle. Due to the limited number of pairs, the series is not infinite but rather truncated at order $\min(M, J)$, i.e. the maximum number of pairs allowed in the subsystem.

Without the HS transformation, the interaction operator remains a two-body operator but its analytic forms are explicitly known. For example, the first summation yields

$$\begin{aligned}C\sum_{\mathbf{x}}\hat{n}_\uparrow(\mathbf{x})\hat{n}_\downarrow(\mathbf{x})\,|\mathbf{Y}\rangle &=C\sum_{\mathbf{x}}\left[\sum_{m=1}^{M}\delta(\mathbf{x} - \mathbf{y}_m)\right]\left[\sum_{j=1}^{J}\delta(\mathbf{x} - \mathbf{y}_{M+j})\right]|\mathbf{Y}\rangle \\ &=C\sum_{(m,j)}\delta(\mathbf{y}_m - \mathbf{y}_{M+j})\,|\mathbf{Y}\rangle\,,\end{aligned} \qquad (2.23)$$

where the last summation is over all possible particle pairs (m, j). Similarly the second summa-

tion corresponds to the two-pair summation and is given as

$$C^2 \sum_{\mathbf{x} \neq \mathbf{x}'}{}' \hat{n}_\uparrow(\mathbf{x}) \hat{n}_\downarrow(\mathbf{x}) \hat{n}_\uparrow(\mathbf{x}') \hat{n}_\downarrow(\mathbf{x}') \ket{\mathbf{Y}} = C^2 \sum_{(m,j)} \sum_{(m',j')}{}' \delta(\mathbf{y}_m - \mathbf{y}_{M+j}) \delta(\mathbf{y}_{m'} - \mathbf{y}_{M+j'}) \ket{\mathbf{Y}} \quad (2.24)$$

where the primed double sum is over all possible two-pairs. Note that we use the Dirac delta notation $\delta(\cdot)$ for clarity but they are still Kronecker deltas as we have not yet taken the continuum limit.

In the end, the coordinate variable summation is in general form as

$$\sum_{\mathbf{x}_1, \mathbf{x}_2} \exp\left[i\mathbf{x}_1(\mathbf{p}_j^{(\tau)} - \mathbf{p}_k^{(\tau+1)})\right] \exp\left[i\mathbf{x}_2(\mathbf{p}_l^{(\tau)} - \mathbf{p}_m^{(\tau+1)})\right] \delta(\mathbf{x}_1 - \mathbf{x}_2)$$
$$= \sum_{\mathbf{x}_1} \exp\left[i\mathbf{x}_1(\mathbf{p}_j^{(\tau)} + \mathbf{p}_l^{(\tau)} - \mathbf{p}_k^{(\tau+1)} - \mathbf{p}_m^{(\tau+1)})\right] = V\delta\left[\mathbf{p}_j^{(\tau)} + \mathbf{p}_l^{(\tau)} - \mathbf{p}_k^{(\tau+1)} - \mathbf{p}_m^{(\tau+1)}\right], \quad (2.25)$$

where $\mathbf{x}_1$ and $\mathbf{x}_2$ are particles of different species. The exponential terms are from the wave function (Slater determinants) and $\delta(\mathbf{x}_1 - \mathbf{x}_2)$ is from the interaction matrix $V[\mathbf{X}]$. For other particles not participating in the connect interaction, the summation takes the form as

$$\sum_{\mathbf{x}_3} \exp\left[i\mathbf{x}_3(\mathbf{p}_j^{(\tau)} - \mathbf{p}_k^{(\tau+1)})\right] = V\delta\left[\mathbf{p}_j^{(\tau)} - \mathbf{p}_k^{(\tau+1)}\right]. \quad (2.26)$$

Eq. (2.25) and (2.26) are just the conservation description in the momentum space for different particles during the two-body scattering process.

Denote the momentum representation of $\hat{V}$ as

$$V[\mathbf{P}^{(i)}, \mathbf{P}^{(j)}] = \left\langle \mathbf{P}^{(i)} \middle| \hat{V} \middle| \mathbf{P}^{(j)} \right\rangle = 1 + C f_1(\mathbf{P}^{(i)}, \mathbf{P}^{(j)}) + C^2 f_2(\mathbf{P}^{(i)}, \mathbf{P}^{(j)}) + \cdots, \quad (2.27)$$

where $f_i(\mathbf{P}^{(i)}, \mathbf{P}^{(j)})$ are composed of all combinations of Eq. (2.25) and Eq. (2.26). Eventually, we simplify Eq. (2.15) into

$$Q_N = \sum_{\{\mathbf{P}\}} \epsilon[\mathbf{P}^{(1)}] \epsilon[\mathbf{P}^{(2)}] \cdots \epsilon[\mathbf{P}^{(N_\tau)}] V[\mathbf{P}^{(1)}, \mathbf{P}^{(2)}] V[\mathbf{P}^{(2)}, \mathbf{P}^{(3)}] \cdots V[\mathbf{P}^{(N_\tau)}, \mathbf{P}^{(1)}], \quad (2.28)$$

where $\epsilon[\mathbf{P}^{(i)}]$ are Gaussian functions and $V[\mathbf{P}^{(i),\mathbf{P}^{(j)}}]$ are a bunch of delta functions. Taking the

continuum limit as in Eq. (1.25), the final form of Q_N is turned into a multidimensional Gaussian integral, which can be evaluated analytically (see Sec. 2.3 for details). As $V[\mathbf{P}^{(i)}, \mathbf{P}^{(j)}]$ is a polynomial of C at degree $\min(M, J)$, the final expressions of Q_N is therefore a polynomial of C at degree $N_\tau \min(M, J)$. In fact, as demonstrated later, the polynomials are actually in powers of the dimensionless $C/\lambda_T^d \equiv \widetilde{C}$, where the extra factors comes in the continuum limit as in Eq. (1.25).

One important feature of this automated-algebra calculation is that we can track the volume power analytically, as shown in Eq. (2.18) and (2.25) (also from the continuum limit as in Eq. (1.25)). As discussed in Sec. 1.3, the dedicated volume cancellation as in Eq. (1.36) is one of the main reason that the b_n is more susceptible to the statistical error. The analytical volume power count allows a analytic cancellation, making the AA method an ideal way for the QVE.

However, the calculation in such naive form is very expensive. The wavefunction at each imaginary time step grows factorially as particle number N, and the number of terms in interaction matrix also scales factorially as particle content M and J. The total computational costs is therefore roughly at order of $\mathcal{O}[(N!M!J!)^{N_\tau}]$.

Fortunately, as pointed out by Lee and Yang [50, 51], we do not need to anti-symmetrize the "pseudo-particles" at immediate imaginary steps. It is because all operators preserve the particle symmetry, and therefore we only need to account for the particle symmetry just once. In other words, we can treat particles at imaginary slices, i.e. $\mathbf{P}^{(2)}$ to $\mathbf{P}^{(N_\tau)}$ as classical distinguishable particles, and only the particles $\mathbf{P}^{(1)}$ are treated as quantum identical particles. Equivalently, we can treat particles at all times steps as distinguishable. In this case, instead of evaluating $\langle \mathbf{P}^{(1)} | \exp\left(-\beta \hat{H}\right) | \mathbf{P}^{(1)} \rangle$, we compute the matrix elements $\langle \mathbf{P}^{(1)} | \exp\left(-\beta \hat{H}\right) | \mathbf{P}^{(N_\tau+1)} \rangle$, and the Fermi statistics is encoded as different boundary conditions of $\mathbf{P}^{(1)}$ and $\mathbf{P}^{(N_\tau+1)}$. In the end, such simplification greatly reduces the overall computational cost to $\mathcal{O}[N!(M!J!)^{N_\tau}]$.

Furthermore, due to the cyclic property of the trace, we do not need to evaluate all $(M!J!)^{N_\tau}$ terms from the expansion of product of $V[\mathbf{P}^{(1)}, \mathbf{P}^{(2)}]V[\mathbf{P}^{(2)}, \mathbf{P}^{(3)}] \cdots V[\mathbf{P}^{(N_\tau)}, \mathbf{P}^{(1)}]$. Instead, we only need to evaluate the contributions that are not cyclically identical. For example, the $\mathcal{O}(C)$ term from the product $V[\mathbf{P}^{(1)}, \mathbf{P}^{(2)}]V[\mathbf{P}^{(2)}, \mathbf{P}^{(3)}] \cdots V[\mathbf{P}^{(N_\tau)}, \mathbf{P}^{(1)}]$ is from $f_1(\mathbf{P}^{(1)}, \mathbf{P}^{(2)}) \times 1 \times \cdots \times 1, 1 \times f_1(\mathbf{P}^{(2)}, \mathbf{P}^{(3)}) \times \cdots \times 1$ and so on. They all give the same results, as can be easily shown by cyclically shifting the variables (see Sec. 2.3 for a more explicit example). Such property

defines a mathematical object called the "necklace". The k-ary necklace of length n is defined as an equivalence class of n-character strings over an alphabet of size k. In our case, we are looking for the necklace of length N_τ, and the alphabet size $k = 1 + \min(M, J)$ is the number of terms as in Eq. (2.27).

Now, instead of taking the full expansion of the product of interaction matrices, we only need to find all possible necklaces, whose number is sub-factorial and given as

$$N_k(n) = \frac{1}{n} \sum_{d|n} \varphi(d) k^{\frac{n}{d}}, \tag{2.29}$$

for the k-ary necklaces of length n, where $\varphi(\cdot)$ is Euler's torrent function

$$\varphi(n) = n \prod_{p|n} \left(1 - \frac{1}{p}\right), \tag{2.30}$$

and $a|b$ under the summation and multiplication is over the distinct prime numbers dividing b. For more details of the necklace and the generation algorithms, see e.g. Refs. [91–93].

2.2.2: Transfer matrix formalism

The formalism presented in the last section laid down the foundation for the AA method. However, its details heavily depend on the particle content and it is unclear how the antisymmetrization is implemented in its current form. Therefore, we develop another unified framework based on the transfer matrix.

Recall that the GCPF can be written in the path integral form as

$$\mathcal{Z} \equiv \mathrm{Tr}\left[e^{-\beta(\hat{H} - \mu \hat{N})}\right] = \int \mathcal{D}\sigma \, \det^2(1 + z\mathcal{U}[\sigma]), \tag{2.31}$$

where $\mathcal{U}[\sigma] = \mathcal{U}_{N_\tau} \ldots \mathcal{U}_2 \mathcal{U}_1$ and $\mathcal{U}_i = \mathcal{T} \mathcal{V}[\sigma_i]\mathcal{T}$, see Eq. (2.10) and (2.11) for details. Note that compared to the previous equations, here we write out the fugacity z explicitly.

Differentiate with respect to fugacity z at $z = 0$, we reproduce

$$\frac{\partial}{\partial z}\Big|_{z=0} \int \mathcal{D}\sigma \, \det^2(1 + z\mathcal{U}[\sigma]) = 2 \int \mathcal{D}\sigma \, \mathrm{tr}\,\mathcal{U} = 2 \left(\frac{L}{\lambda_T}\right)^d = Q_1. \tag{2.32}$$

Similarly higher-order derivatives yields contributions from other systems. For example, we have

$$Q_2 = \frac{1}{2!} \int \mathcal{D}\sigma \left[4(\mathrm{tr}\,\mathcal{U})^2 - 2(\mathrm{tr}\,\mathcal{U}^2) \right], \tag{2.33}$$

$$Q_3 = \frac{1}{3!} \int \mathcal{D}\sigma 4 \left[2(\mathrm{tr}\,\mathcal{U})^3 - 3(\mathrm{tr}\,\mathcal{U})(\mathrm{tr}\,\mathcal{U}^2) + \mathrm{tr}\left(\mathcal{U}^3\right) \right], \tag{2.34}$$

and so on.

To carry out the path integral, we write the matrix product in its explicit form. Generally, every time $\mathcal{U}$ appears, a given temporal index j_0 and its corresponding field $\sigma(\mathbf{x}, j_0)$ will appear once, and that factor will become part of the integrand for the $\sigma(\mathbf{x}, j_0)$ integral living on that time slice. In the case of b_2, for instance, the j_0 factor will appear twice in each of the traces. The corresponding path integral will then take the form

$$\int \mathcal{D}\sigma(\mathbf{x}, j_0) \left[\mathcal{T}\mathcal{V}_{j_0}[\sigma]\mathcal{T} \right]_{xy} \left[\mathcal{T}\mathcal{V}_{j_0}[\sigma]\mathcal{T} \right]_{wz}. \tag{2.35}$$

Writing out all the indices explicitly at this point, the integral is separated from the kinetic energy factors and one is left with the simple task of evaluating

$$\int \mathcal{D}\sigma(\mathbf{x}, j_0) \left[\mathcal{V}_{j_0}[\sigma] \right]_i \left[\mathcal{V}_{j_0}[\sigma] \right]_j = 1 + \left[\exp(\tau g) - 1 \right] \delta_{ij} = 1 + C\delta_{ij}, \tag{2.36}$$

where we have used the fact that the potential energy factors are diagonal in coordinate space for a contact interaction.

Furthermore, we can unify the path integral over different kind of traces using the transfer matrix $\mathcal{M}$. For example, for the two body case, we have

$$\int \mathcal{D}\sigma(\mathrm{tr}\,\mathcal{U})^2 = \sum_{ab} \left[M_2^{N_\tau} \right]_{ab,ab}, \tag{2.37}$$

$$\int \mathcal{D}\sigma\,\mathrm{tr}\left(\mathcal{U}^2\right) = \sum_{ab} \left[M_2^{N_\tau} \right]_{ab,ba}, \tag{2.38}$$

where the r.h.s. of the first equation corresponds to a regular trace while that of the second equa-

tion to a "twisted" trace. The transfer matrix for the two-body case is given as

$$[M_2]_{ab,cd} = \left[\mathcal{T}^2\right]_{ac}\left[\mathcal{T}^2\right]_{bd} + C\left[\mathcal{I}_2\right]_{ab,cd}, \tag{2.39}$$

where the interaction part is

$$[\mathcal{I}_2]_{ab,cd} = \sum_i [\mathcal{T}]_{ai}[\mathcal{T}]_{bi}[\mathcal{T}]_{ic}[\mathcal{T}]_{id}. \tag{2.40}$$

Eventually, the partition function is now in form of

$$Q_2 = \frac{1}{2}\sum_{a,b}\left\{4\left[M_2^{N_\tau}\right]_{ab,ab} - 2\left[M_2^{N_\tau}\right]_{ab,ba}\right\}, \tag{2.41}$$

To evaluate $\mathcal{M}^{N_\tau}$, we use the explicit forms

$$\left[\mathcal{T}^2\right]_{pp'} = e^{-\tau\frac{p^2}{2m}}\delta_{pp'} = \epsilon[p]\delta_{pp'}, \tag{2.42}$$

and similarly

$$[\mathcal{I}_2]_{p_1p_2,p_1'p_2'} = \frac{1}{V}e^{-\frac{\tau}{2}\frac{p_1^2+p_2^2}{2m}}e^{-\frac{\tau}{2}\frac{p_1'^2+p_2'^2}{2m}}\delta_{p_1+p_2,p_1'+p_2'} = \epsilon[p_1]\epsilon[p_2]\epsilon[p_1']\epsilon[p_2']\delta_{p_1+p_2,p_1'+p_2'}, \tag{2.43}$$

which corresponds to Eq. (2.26) and (2.25) respectively. More generally, in the N-body case, the form of $\mathcal{M}$ is

$$\mathcal{M}_N = \mathcal{K}_0 + C\mathcal{K}_1 + C^2\mathcal{K}_2 + \ldots, \tag{2.44}$$

which truncates at order $\min M, J$, the same as in Eq. (2.22). $\mathcal{K}_0$ represents the noninteracting piece, namely

$$[\mathcal{K}_0]_{\mathbf{ab}} = \left[\mathcal{T}^2\right]_{a_1b_1}\left[\mathcal{T}^2\right]_{a_2b_2}\cdots\left[\mathcal{T}^2\right]_{a_Nb_N}, \tag{2.45}$$

where we have used collective indices $\mathbf{a} = (a_1, a_2, \ldots, a_N)$ and $\mathbf{b} = (b_1, b_2, \ldots, b_N)$. Higher-order $\mathcal{K}_n$ matrices are composed of the noninteracting part as $\mathcal{K}_0$ and the n-pair interactions tensor $\mathcal{I}_n$,

which is the combinations of $\mathcal{I}_2$ (due to the contact interaction) over all possible pairing configurations. For example, for a three-body system, the interaction matrix $\mathcal{I}_3$ is

$$[\mathcal{I}_3]_{abc,def} = \left[\mathcal{T}^2\right]_{ad} [\mathcal{I}_2]_{bc,ef} + \left[\mathcal{T}^2\right]_{be} [\mathcal{I}_2]_{ac,df}, \tag{2.46}$$

which includes two possible pairs. In other words, the matrix $\mathcal{K}_n$ plays the role of $f_n(\mathbf{P}^{(i)}, \mathbf{P}^{(j)})$ as in Eq. (2.27), except that $\mathcal{K}_n$ also includes the propagator terms $\mathcal{T}^2$.

Taking the N_τ-th power of the above M_N, we may identify the various multinomial-expansion terms contributing at each order in powers of C^n, $n = 0, 1, 2, \ldots, N_\tau \min(M, J)$ as

$$(\mathcal{M}_N)^{N_\tau} = K_0^{N_\tau} + C \sum_{k=0}^{N_\tau - 1} K_0^k K_1 K_0^{N_\tau - k - 1} + C^2 \left[\sum_{k=0}^{N_\tau - 1} K_0^k K_2 K_0^{N_\tau - k - 1} + \ldots\right] + \ldots. \tag{2.47}$$

It is also easier to identify the cyclic property using the above expression.

As discussed in Sec. 1.3, it is advantageous to work in the subspace directly, i.e. calculating the subspace contribution Q_{MJ} rather than Q_N. In analogue to the derivation of subspace coefficients, we write GCPF with explicit $z_\uparrow$ and $z_\downarrow$

$$\mathcal{Z} \equiv \mathrm{Tr}\left[e^{-\beta(\hat{H} - \mu\hat{N})}\right] = \int \mathcal{D}\sigma \, \det(1 + z_\uparrow \mathcal{U}[\sigma])\det(1 + z_\downarrow \mathcal{U}[\sigma]), \tag{2.48}$$

and take derivative with respect to $z_\uparrow$ and $z_\downarrow$ at different order. All the following steps are the same as demonstrated above. Below, we list the final explicit expressions for Q_{MJ} up to the five-body system that yields a non-zero interaction-induced contribution.

$$Q_{11} = \sum_{ab} \left[\mathcal{M}_2^{N_\tau}\right]_{ab,ab}, \tag{2.49}$$

$$Q_{21} = \frac{1}{2!} \sum_{abc} \left\{\left[\mathcal{M}_3^{N_\tau}\right]_{abc,abc} - \left[\mathcal{M}_3^{N_\tau}\right]_{abc,bac}\right\}, \tag{2.50}$$

$$Q_{31} = \frac{1}{3!} \sum_{abcd} \left\{\left[\mathcal{M}_4^{N_\tau}\right]_{abcd,abcd} - 3\left[\mathcal{M}_4^{N_\tau}\right]_{abcd,bacd} + 2\left[\mathcal{M}_4^{N_\tau}\right]_{abcd,bcad}\right\}, \tag{2.51}$$

$$Q_{22} = \frac{1}{(2!)^2} \sum_{abcd} \left\{\left[\mathcal{M}_4^{N_\tau}\right]_{abcd,abcd} - 2\left[\mathcal{M}_4^{N_\tau}\right]_{abcd,abdc} + \left[\mathcal{M}_4^{N_\tau}\right]_{abcd,badc}\right\}, \tag{2.52}$$

$$Q_{41} = \frac{1}{4!} \sum_{abcde} \left\{ \left[\mathcal{M}_5^{N_\tau} \right]_{abcde,abcde} - 6 \left[\mathcal{M}_5^{N_\tau} \right]_{abcde,abdce} \right.$$
$$\left. + 3 \left[\mathcal{M}_5^{N_\tau} \right]_{abcde,badce} + 8 \left[\mathcal{M}_5^{N_\tau} \right]_{abcde,acdbe} - 6 \left[\mathcal{M}_5^{N_\tau} \right]_{abcde,bcdae} \right\}, \tag{2.53}$$

$$Q_{32} = \frac{1}{3!2!} \sum_{abcde} \left\{ \left[\mathcal{M}_5^{N_\tau} \right]_{abcde,abcde} - 3 \left[\mathcal{M}_5^{N_\tau} \right]_{abcde,acbde} \right.$$
$$\left. + 2 \left[\mathcal{M}_5^{N_\tau} \right]_{abcde,bcade} - \left[\mathcal{M}_5^{N_\tau} \right]_{abcde,abced} + 3 \left[\mathcal{M}_5^{N_\tau} \right]_{abcde,acbed} - 2 \left[\mathcal{M}_5^{N_\tau} \right]_{abcde,bcaed} \right\}. \tag{2.54}$$

In summary, within the transfer matrix formalism, we are able to present the expression for Q_{MJ} in a unified form. It also allows a cleaner representation of the necklace object as demonstrated in Eq. (2.47). Moreover, the particle symmetry has also been automatically encoded in the GCPF and is present in form of the trace and "anomalous" traces. The distinguishable particles at the intermediate imaginary time steps are easy to implement using matrix elements.

2.2.3: Observables

To calculate observables in the QMC method, we firstly need to couple the one-body observable operator to a source in the Hamiltonian, i.e.

$$\hat{H} \rightarrow \hat{H}(j) = \hat{H} + j\hat{O}, \tag{2.55}$$

where j is the source current and $\hat{O}$ is the desired one-body observable. Similarly, the GCPF becomes

$$\mathcal{Z}[j] = \text{Tr}_F \left(\exp\left[-\beta(\hat{H}[j] - \mu\hat{N}) \right] \right). \tag{2.56}$$

The expected value of observable is then given by

$$\left\langle \hat{O} \right\rangle = \frac{1}{\mathcal{Z}} \text{Tr}_F \left[e^{-\beta(\hat{H} - \mu\hat{N})} \hat{O} \right] = \left. \frac{\delta \ln \mathcal{Z}(j)}{\delta j} \right|_{j=0}. \tag{2.57}$$

For higher-body observables, multiple source terms are required, i.e. $\hat{H} \rightarrow \hat{H}(j_1, j_2, \cdots)$, and the observables are reproduced via taking higher-order derivatives. As the QMC results are discrete, the calculation of the numerical derivative could be expensive and can be unstable in case of higher-order derivatives are involved.

On the other hand, the calculation of observable in the AA method is more straightforward. Same as Eq. (2.57), we decompose both numerator and denominator into subspaces

$$
\begin{aligned}
\left\langle \hat{O} \right\rangle &= \frac{1}{\mathcal{Z}} \operatorname{Tr}_F \left[\mathrm{e}^{-\beta(\hat{H}-\mu\hat{N})} \hat{O} \right] = \frac{zW_1 + z^2 W_2 + z^3 W_3 + \cdots}{1 + zQ_1 + z^2 Q_2 + z^3 Q_3 + \cdots} \\
&= \left(\sum_{N=1} z^N W_N \right) \left[1 - \left(\sum_{N=1} z^N Q_N \right) + \left(\sum_{N=1} z^N Q_N \right)^2 + \cdots \right] \\
&= z \cdot W_1 + z^2 \cdot (W_2 - Q_1 W_1) + z^3 \cdot \left[W_3 - Q_1 W_2 + \left(Q_1^2 - Q_2 \right) W_1 \right] + \cdots,
\end{aligned}
\tag{2.58}
$$

where we expand the denominator in the second line and W_N is defined as

$$
W_N = \operatorname{tr}_N(\mathrm{e}^{-\beta\hat{H}} \hat{O}).
\tag{2.59}
$$

To evaluate W_N we take the same procedure

$$
W_N = \sum_{\mathbf{P}} \langle \mathbf{P} | \mathrm{e}^{-\beta\hat{H}} \hat{O} | \mathbf{P} \rangle = \sum_{\mathbf{P}} \sum_{\mathbf{Q}} \langle \mathbf{P} | \mathrm{e}^{-\beta\hat{H}} | \mathbf{Q} \rangle \, \langle \mathbf{Q} | \hat{O} | \mathbf{P} \rangle,
\tag{2.60}
$$

where the first term takes the same form as in evaluating Q_N, and the second matrix element can be written explicitly as analytic expressions for general operator $\hat{O}$.

However, the observable calculation in the AA method also faces its own challenges. For example, the general form of W_N is no longer necessarily a multidimensional Gaussian integral due to the arbitrary form of $\langle \mathbf{Q} | \hat{O} | \mathbf{P} \rangle$ term. If no analytical solution to the integral is available, it will lead to sheer increase in computational costs as we have to incorporate numerical methods for evaluation. Fortunately, as we will show later, the Gaussian form assumptions hold true for many observables of physical importance.

2.2.4:   Renormalization

The results we obtained so far are in terms of the bare coupling strength C. To encode the true physics, our next step is to renormalize the bare coupling strength. To this end, we present two different procedures here and claim that the first procedure is advantageous. We leave the details and discussions supporting this argument to Appendix. A.

Procedure I   The first way is to tune the bare coupling such that the calculation of Δb_2, at a given order N_τ in the Trotter-Suzuki factorization, reproduces the known, continuum-limit value of that coefficient as in Eq. (1.68), (1.69) and (1.70). The idea of this procedure is that one is approaching the continuum limit along the "line of constant physics", where the physics is set by the second-order virial coefficient. More specifically, our calculations yield, at a given N_τ, analytic expressions for Δb_n which are polynomials in the dimensionless coupling $\tilde{C}$. The latter is then determined by matching to Δb_2. The remaining Δb_n are then simply evaluated by plugging in the tuned value of $\tilde{C}$.

Procedure II   This procedure is commonly used in QMC, where we tuned the bare coupling such that the largest eigenvalue of the factorized transfer matrix matched the value dictated by Lüscher's formula [94]. As we show next, this can be accomplished mostly analytically. Starting with Trotter-Suzuki-factorized transfer matrix

$$\mathcal{U}_\tau \equiv e^{-\beta \hat{T}/(2N_\tau)} e^{-\beta \hat{V}/N_\tau} e^{-\beta \hat{T}/(2N_\tau)}, \tag{2.61}$$

whose two-body matrix elements, in the center-of-mass frame, are given by

$$T(\boldsymbol{p_r}, \boldsymbol{q_r}) = \langle \boldsymbol{p_1 p_2} | e^{-\beta \hat{T}/(2N_\tau)} e^{-\beta \hat{V}/N_\tau} e^{-\beta \hat{T}/(2N_\tau)} | \boldsymbol{q_1 q_2} \rangle, \tag{2.62}$$

where

$$\begin{cases} \boldsymbol{p_1} + \boldsymbol{p_2} = 0 \\ \boldsymbol{q_1} + \boldsymbol{q_2} = 0 \end{cases} \text{and} \quad \begin{cases} \boldsymbol{p_1} - \boldsymbol{p_2} = 2\boldsymbol{p_r} \\ \boldsymbol{q_1} - \boldsymbol{q_2} = 2\boldsymbol{q_r} \end{cases}. \tag{2.63}$$

Inserting complete sets of states, we have

$$T(\boldsymbol{p_r}, \boldsymbol{q_r}) = e^{-\beta p_r^2/(2N_\tau)} e^{-\beta q_r^2/(2k)} \left(\delta_{\boldsymbol{p_r q_r}} + \frac{C}{V} \right), \tag{2.64}$$

which evaluated at momenta $\boldsymbol{p_r} = 2\pi\boldsymbol{a}/L$ and $\boldsymbol{q_r} = 2\pi\boldsymbol{b}/L$, where $\boldsymbol{a}$ and $\boldsymbol{b}$ are integer vectors, becomes

$$T_{\boldsymbol{ab}} = f_{\boldsymbol{a}}f_{\boldsymbol{b}}\left(\delta_{\boldsymbol{ab}} + \frac{C}{V}\right) \equiv f_{\boldsymbol{a}}f_{\boldsymbol{b}}\left[\delta_{\boldsymbol{ab}} + \tilde{C}\,(2\pi x)^{3/2}\right]. \tag{2.65}$$

For convenience, we defined $f_{\boldsymbol{a}} = \exp\!\left(-\frac{x}{2k}\frac{4\pi^2\boldsymbol{a}^2}{m}\right)$, rescale C into $\tilde{C}$, and used $x = \beta/L^2$. Tuning $\tilde{C}$ to reproduce the leading eigenvalue $\lambda_0 = \exp\!\left(-\frac{x}{k}\frac{4\pi^2\eta_0^2}{m}\right)$ amounts to imposing the condition

$$\sum_{\mathbf{b}}[T - \lambda_0 I]_{\mathbf{ab}}\,\mathbf{v_b} = 0, \tag{2.66}$$

which can be solved analytically to obtain the dependence of the bare coupling on λ_0:

$$\tilde{C} = \frac{1}{(2\pi x)^{\frac{3}{2}}}\left[\sum_{\boldsymbol{a}}^{\Lambda}\frac{1}{\lambda_0/f_{\boldsymbol{a}}^2 - 1}\right]^{-1}, \tag{2.67}$$

Section 2.3: Automated-algebra method: technical details

2.3.1: Method overview

In this section, we present a more detailed technical discussion of our automated algebra method to capture the general idea represented in our code. The ultimate goal of the method is to evaluate the canonical partition functions, which requires the evaluation of the matrix elements of $\mathcal{M}^{N_\tau}$. Roughly speaking, the complete computation is composed of three steps:

1. **Term generation**: Expand the product $\mathcal{M}^{N_\tau}$ symbolically, which will yield a large number of terms as N_τ is increased.

2. **Delta crunch**: Introduced by $\mathcal{T}^2$ and $\mathcal{I}$ tensors, the expanded expressions are now composed of propagator terms $\epsilon(\cdot)$ as well as a bunch of delta functions. This step contracts indices to saturate all Kronecker deltas, thus simplifying each term into a product of Gaussian functions, namely the propagator $\epsilon(\mathbf{p})$, by integrating out a subset of variables. This is the most computationally expensive step.

3. **Gaussian integration**: For each term, take the summation over the rest of the variables and take the continuum limit, ultimately turning each term into a multidimensional Gaus-

sian integral whose results are analytically available as the well-known formula

$$\int \mathcal{D}\mathbf{x} \exp\left(-\frac{1}{2}\mathbf{x}^T \mathcal{A}\mathbf{x}\right) = \sqrt{\frac{(2\pi)^n}{\det \mathcal{A}}}, \tag{2.68}$$

where n is the dimension of vector $\mathbf{x}$ and $\mathcal{A}$ is the quadratic coefficient matrix.

We now proceed to elaborate on the above steps.

Step 1 The first step is to expand the product of interaction matrix as in Eq. (2.47), i.e.

$$(\mathcal{M}_N)^{N_\tau} = K_0^{N_\tau} + C \sum_{k=0}^{N_\tau-1} K_0^k K_1 K_0^{N_\tau-k-1} + C^2 \left[\sum_{k=0}^{N_\tau-1} K_0^k K_2 K_0^{N_\tau-k-1} + \ldots\right] + \ldots \tag{2.69}$$

It is easier to organize the expansion order by order. To find all necklaces contributing at the order $\mathcal{O}(C^l)$, we firstly generate all partitions of the integer l with N_τ parts, under the constraint

$$l_i \leq \min(M, J), \forall i \in [1, N_\tau] \tag{2.70}$$

where l_i is the value of ith part, and $\min(M, J)$ is the highest degree in Eq. (2.27) and (2.44), i.e. the maximum pairs allowed. For example, in a (2+2) subsystem when $N_\tau = 3$, there are two partitions $(2, 2, 0)$ and $(2, 1, 1)$ at $\mathcal{O}(C^4)$ order, which means the $\mathcal{O}(C^4)$ terms are either $\mathcal{K}_2 \mathcal{K}_2 \mathcal{K}_0$ or $\mathcal{K}_2 \mathcal{K}_1 \mathcal{K}_1$. Each partition corresponds to a subset of the 3-ary necklace class of length 3 called the fixed-content necklaces. In the language of necklace, the two partitions above corresponds to two contents: one with 1 type-0 (i.e. $\mathcal{K}_0$), 0 type-1 and 2 type-2 beads, and another with 0 type-0, 2 type-2 and 1 type-2 beads.

Breaking the k-ary necklaces into subsets of fixed-content necklaces also allows better control of the computational load and favors the parallelization as the calculations are completely independent.

In our implementation, we use the program by Ref. [93] to generate the fixed-content necklace, which represents the combinations of $\mathcal{K}_n$ operators. We then symbolically expand it in terms of propagators and interaction matrices, and eventually the results expressions contains N_τ propagators and interaction terms in form of delta functions. By using the volume power counting, we are also able to discard terms at higher-volume order, i.e. the disconnected diagrams contributions,

and therefore the volume cancellation is performed analytically.

We also takes this opportunity to show an explicit example of the cyclic symmetry. It is more clear to use the form as in Eq. (2.27) that

$$\prod_{i=1}^{N_\tau} \left\langle \mathbf{P}^{(i)} \middle| e^{-\tau \hat{V}} \middle| \mathbf{P}^{(i+1)} \right\rangle = \prod_{i=1}^{N_\tau} [1 + C f_1(\mathbf{P}^{(i)}, \mathbf{P}^{(i+1)}) + C^2 f_2(\mathbf{P}^{(i)}, \mathbf{P}^{(i+1)}) + \cdots] \tag{2.71}$$

For example, for $N_\tau = 2$, there are two terms $f_1(\mathbf{P}^{(1)}, \mathbf{P}^{(2)}) f_2(\mathbf{P}^{(2)}, \mathbf{P}^{(3)})$ and $f_2(\mathbf{P}^{(1)}, \mathbf{P}^{(2)}) f_1(\mathbf{P}^{(2)}, \mathbf{P}^{(3)})$ at $\mathcal{O}(C^3)$, which are equivalent under the cyclic variable substitution $\mathbf{P}^{(1)} \to \mathbf{P}^{(2)}$, $\mathbf{P}^{(2)} \to \mathbf{P}^{(3)}$, $\mathbf{P}^{(3)} \to \mathbf{P}^{(1)}$.

Step 2   After the expansion, we obtain a large number of independents terms and each of them is in the form of a product of propagators and delta functions as

$$\epsilon(\mathbf{P}^{(1)})\epsilon(\mathbf{P}^{(2)})\epsilon(\mathbf{P}^{(3)}) \cdots \times \Delta(\mathbf{P}^{(1)}, \mathbf{P}^{(2)}, \mathbf{P}^{(3)}, \cdots) \tag{2.72}$$

where we omit the summation indices in front. The propagator $\epsilon(\mathbf{P}^{(i)})$ is a shorthand for the kinetic-energy product $\epsilon(\mathbf{p}_1^{(i)})\epsilon(\mathbf{p}_2^{(i)}) \cdots \epsilon(\mathbf{p}_{M+N}^{(i)})$, and $\Delta(\cdot)$ is a product of Kronecker δ's from the combination of $f_i(\mathbf{P}^{(i)}, \mathbf{P}^{(i+1)})$ functions.

The second step of the method is to carry out the omitted sums on such a term over all momentum variables from $\mathbf{P}^{(2)}$ to $\mathbf{P}^{(N_\tau-1)}$, i.e., all intermediate complete sets inserted. This operation is called "Delta crunch" as it will reduce the Δ function by substituting all available momentum variables, i.e., "crunching" the δ's into the ϵ factors. To this end, we loop through the δ's in the Δ function one at a time, and perform variable substitution in both ϵ and Δ. To provide efficiency in variable substitutions, the ϵ and the δ's are represented as a hashmap, which offers a $\mathcal{O}(1)$ time in lookup and modification.

In short, at this step we perform the tensor contraction (for all internal indices; not the trace indices) over all intermediate time steps. At the end of this step, the expressions is just the matrix element $\left\langle \mathbf{P}^{(1)} \middle| \hat{M} \middle| \mathbf{P}^{(N_\tau+1)} \right\rangle = \left[\mathcal{M}^{N_\tau} \right]_{abc\ldots,\alpha\beta\gamma\ldots}$

Step 3   The last step is to take the traces (both the normal and anomalous ones), which encodes the pertinent quantum statistics, and evaluate them in the continuum limit. To this end,

we implement different boundary conditions on $\mathbf{P}^{(1)}$ and $\mathbf{P}^{(N_\tau)+1}$. For example, in Eq. (2.50), the first term on the right-hand side is a normal trace, which we obtain by imposing a periodic boundary condition

$$\mathbf{p}_i^{(1)} = \mathbf{p}_i^{(N_\tau+1)}, \forall i = 1, 2, 3 \tag{2.73}$$

The second term is the analogus trace with "twisted" indices, corresponding to the boundary condition

$$\begin{cases} \mathbf{p}_1^{(1)} = \mathbf{p}_2^{(N_\tau+1)} \\ \mathbf{p}_2^{(1)} = \mathbf{p}_1^{(N_\tau+1)} \\ \mathbf{p}_3^{(1)} = \mathbf{p}_3^{(N_\tau+1)} \end{cases} \tag{2.74}$$

These boundary conditions introduce the last set of delta functions to be crunched at time step N_τ.

Once the last delta crunch step is completed, the resulting expression will be a product of propagators only, e.g. in form like

$$\epsilon(\mathbf{p}_1^{(1)})\epsilon(\mathbf{p}_2^{(1)})\epsilon(\mathbf{p}_3^{(1)})\epsilon(\mathbf{p}_1^{(1)} + \mathbf{p}_2^{(1)} - \mathbf{p}_3^{(1)})\cdots . \tag{2.75}$$

Note that momentum variables at other time steps also exist, which corresponds to the loop as in the Feynman diagrams.

Recalling that $\epsilon(\mathbf{p})$ is a Gaussian function, the evaluation of the summation over the remaining momentum variables is easiest carried out in the continuum limit. We convert the above product into a multidimensional quadratic Gaussian integral

$$\exp\left(-\frac{\tau}{2m}\mathbf{p}^T \mathcal{A}\mathbf{p}\right) \tag{2.76}$$

where $\mathbf{p}$ contains all remaining momentum variables. The matrix $\bar{\mathbf{A}}$ is symmetric and positive-definite, such that one can use Cholesky decomposition to evaluate the determinant, which is computationally more efficient and numerically more stable than the LU decomposition.

2.3.2: Parallelization

Before concluding this section, we want to add one more technical note on the parallelization of our method. Compared to more conventional methods such as QMC, ours is much easier to parallelize. All the terms generated in the first step are independent from each other, which means they can be evaluated in fully parallel fashion with little or no communication overhead among processes. Moreover, the evaluation of each term is cheap as it does not involve complicated linear algebra operations, and so it is suitable to run on any number of CPU cores. These features make our method ideal to run on a distributed, heterogeneous computing cluster, such as the Open Science Grid or the Folding@home project, where the computational power is unevenly distributed across nodes, in contrast with traditional supercomputers, where the number of available cores can be much higher. We would like to acknowledge Open Science Grid [95, 96] here for the computational resources supporting part of works presented in this dissertation.

Section 2.4: Resummation techniques

The last piece in our arsenal is a mathematical technique called resummation which has been widely applied in physics to deal with asymptotic series. Here, we introduce two kinds of resummation techniques that will be used later: the Padé resummation and the Borel-Padé (or just Borel for short) resummation.

Firstly, we define the Padé approximant. For a given series $F(z)$ in form of

$$F(z) = \sum_n f_n z^n,$$

(2.77)

the Padé approximation at $[M/N]$ order is defined as

$$\widetilde{F}(z) = \frac{P_M(z)}{Q_N(z)} = \frac{p_0 + p_1 z + \cdots + p_M z^M}{1 + q_1 z + \cdots + q_N z^N},$$

(2.78)

where the coefficients p_i and q_i are determined by requiring $\widetilde{F}(z)$ reproduce the first $M + N$ known coefficients in $F(z)$ after expanding the denominator. The calculation can be turned into a linear problem $Ax = b$, and the matrix A depends on the original coefficients in $F(z)$ (see e.g. [97, 98] for details).

Using the Padé approximant in place of the truncated $M + N$ order series is the Padé resum-

mation. Similarly the Borel-Padé resummation combines the Borel integral sum with the Padé approximant, and is especially useful when the series coefficients diverge quickly.

By applying the Borel transformation $\mathcal{B}$ on the original series $F(z)$, we have a new series

$$\mathcal{B}F(z) = \sum_n \frac{f_n}{n!} z^n, \tag{2.79}$$

where the factorial damping factors are expected to help the series to converge.

If the integral

$$B(z) \equiv \int_0^\infty \mathrm{d}t \ \mathrm{e}^{-t} \mathcal{B}F(tz) \tag{2.80}$$

converges for the given z, we then reproduce the original series and $B(z)$ is called the Borel sum of series $F(z)$. As only a finite number of coefficients of $F(z)$ known and so does $B(z)$, one can further apply the Padé approximation on $\mathcal{B}F(z)$

$$\mathcal{B}F(z) = P_M(z)/Q_N(z), \tag{2.81}$$

and the Borel sum becomes

$$B(z) = \int_0^\infty \mathrm{d}t \mathrm{e}^{-t} \frac{P_M(tz)}{Q_N(tz)}, \tag{2.82}$$

which defines the Borel-Padé resummation for the original series $F(z)$.

Conventionally, most applications of resummation method are related to the perturbation theory [99] or diagrammatic expansion [100]. The lack of knowledge of higher-order coefficients limits its application to the QVE.

In this dissertation, we will mainly use the Padé resummation method, though sometimes show the Borel-Padé results for comparison. This is because the Borel-Padé method is more suitable to divergent asymptotic series, especially with diverging coefficients (which is one of the motivations using the Borel transformation). Such features are more common in the context of QCD rather than the QVE for ultracold atoms. But we would like to note that in the general ultracold atoms study, there are many successful applications of the Borel-Padé methods such as in

Refs. [101–103]

As will be shown in later chapters, with our estimations on up to the fifth-order coefficients, the resummation significantly improve the convergence region compared to the finite-order series at its face value. In some situations, we even observed quantitative agreements between the resummed results and other existing results at low temperature in the vicinity of the critical temperature.

But the resummation method is definitely not a free meal and a few intrinsic issues stand against the application of resummation techniques. The major issue is that the validity of the Padé approximation cannot be taken for granted *a priori*, which is also pointed out in Ref. [24]. In the absence of reference results for benchmark, we cannot tell the region of convergence of the resummed results beforehand. Making new predictions using the resummation method therefore should be taken with a grain of salt. See Sec. 5.3.2 for an example.

A related issue is that there is no robust proof nor theorem about the order of Padé approximant. We empirically observed that the central order, i.e. $[m/m]$, or off-central order, i.e. $[(m+1)/m]$ or $[m/(m+1)]$, always yield better results compared to other order. Among these three choices, which specific order to use varies case by case. Indeed, we can make an argument based on the asymptotic behavior of the target quantity in the dense limit $z \to \infty$ such that we select the central order $[m/m]$ if the observable is expected to converge. In the case of the order parameter during a phase transition, $[m/(m+1)]$ seems a better choice, while $[(m+1)/m]$ order captures the monotonic behaviour better than the other two choices. However, in practice, it is easy to find counter-example to the above assumptions. In addition, another issue is that the Padé approximant is deterministic, depending only on the known coefficients of the series. Therefore, there is no way to systematically improve Padé resummed results.

Despite of such issues, the resummation method remains an important technique in practice, as it offers a computationally economical way to extrapolate the QVE to a much wide regime. In situations where results from other methods such as the QMC exist, we can make confident predictions and extend the discrete results to smooth and even analytic ones.

CHAPTER 3:   Homogeneous Fermi Gas: The unitary limit

In this chapter, we will focus on a system called Unitary Fermi Gas, i.e. the homogeneous Fermi gas in the unitary limit. In the next chapter, we will revisit the homogeneous system across the BCS-BEC crossover and in different dimensions.[1]

Section 3.1:   Unitary Fermi Gas (UFG)

In Sec. 1.1.2 when we discussed BCS-BEC crossover, we emphasized that in the middle there was a peculiar point called the unitary limit, or simply "unitarity". In this limit, the scattering length diverges $1/(k_F a_s) \to 0$, leaving the only length scale in the system being the interparticle distance $\propto n^{-1/3}$. The system at unitarity is therefore universal, whose properties could be written as the product of a dimensionless function and a power of density. In other words, the microscopic details of the interaction have no influence on the physics. Such universality is like the Bifröst connecting different domains in the world of physics [13, 106–110]. For example, systems as different as ultracold atoms and neutron matter can be described by the same dimensionless function.[2]

Here, we consider the spin-1/2 Fermi gas at the unitarity. As shown in Eq. (1.3) with $\hat{V}_{\text{ext}} = 0$, the Hamiltonian of the homogeneous Fermi gas is given as

$$\hat{H} = \hat{T} + \hat{V}. \tag{3.1}$$

where $\hat{T}$ and $\hat{V}$ are

$$\hat{T} = \sum_{s=\uparrow,\downarrow} \int d^d r \ \hat{\psi}_s^\dagger(\mathbf{r}) \left(-\frac{\hbar \nabla^2}{2m} \right) \hat{\psi}_s(\mathbf{r}), \tag{3.2}$$

---

[1]This chapter is based on works published in Ref. [104, 105]

[2]Strictly speaking, this statement hold only up to the order $(k_F r_e)^2$, as we neglect the effect range term in Eq. 1.1. Therefore, the universality between the UFG and neutron matter is only valid in the dilute regime where the finite-range effect is negligible.

Table 3.1: The maximum temporal steps $N_{\tau,\text{max}}$ calculated with automated-algebra method for homogeneous Fermi gas.[3]

Q_{MN}	Q_{11}	Q_{21}	Q_{31}	Q_{22}	Q_{41}	Q_{32}	Q_{51}	Q_{42}	Q_{33}	Q_{61}	Q_{52}	Q_{43}
$N_{\tau,\text{max}}$	21	21	15	14	12	11	8	8	8	6	6	6

and

$$\hat{V}_{\text{int}} = -g \int d^d r \ \hat{n}_\uparrow(\mathbf{r})\hat{n}_\downarrow(\mathbf{r}). \tag{3.3}$$

See Eq. (1.4) and (1.6) for details. To tune the system to the unitary limit, we renormalize g to reproduce $\Delta b_2^{\text{UFG}} = 1/\sqrt{2}$, see Eq. (1.70).

Section 3.2: Quantum Virial Expansion of Unitary Fermi Gas with the AA method

3.2.1: From $N_\tau = 1$ and 2 to $N_\tau \to \infty$ limit

In Sec. 2.2.2, we demonstrated an example evaluating the general partition function at leading-(semi-classical approximation, $N_\tau = 1$) and next-to-leading-order ($N_\tau = 2$). Although the semi-classical approximation results are qualitatively correct (see Ref. [90] and Sec. 5.3.1), to achieve quantitatively accurate results, results at higher N_τ and, more importantly, the extrapolation to the $N_\tau \to \infty$ limit are required. With the help of automated-algebra method, we achieved the calculation of Q_{MN} up to $N_{\tau,\text{max}}$ shown in Table. 3.1.

In Fig. 3.1, we plot the Δb_n at given N_τ for $n = 4, 5$ as functions of $1/N_\tau$ for different coupling strengths, represented as the fraction of $\Delta b_2/\Delta b_2^{\text{UFG}}$. In this notation, the noninteracting limit corresponds to $\Delta b_2/\Delta b_2^{\text{UFG}} = 0$ and the unitary limit is at $\Delta b_2/\Delta b_2^{\text{UFG}} = 1$.

Although the convergence curve is monotonically approaching specific values in the case of Δb_5 as $N_\tau \to \infty$, we observed non-monotonic convergence in the case of Δb_4. This is because our results are not based on perturbation theory and there is no systematical description of the convergence as a function of N_τ. Recall that during the renormalization process, we tune the coupling strength C to the two-particle physics (Δb_2) and use it to calculate in higher-particle systems. At the same decomposition order N_τ, however, the truncated quantum effects are not the same for different systems. In other words, the effects of finite imaginary-time spacing are differ-

---

[3]Note that this table include values from latest ongoing works and different from those reported in Ref. [104]

ent for different particle contents. Therefore, the final error we observed is a mixed effect of the direct decomposition error and the indirect competition between such unmatched error from truncated quantum effects. As a result, we may observe the curve points in the wrong direction at low N_τ, where the error from competition still dominates; while when N_τ is large enough, the direct decomposition error dominates and the convergence becomes monotonic again. From a alternative technical point of view, the non-monotonicity can also be interpreted as temporal "finite size effect" in analogue to its counterpart in the spatial lattice, which introduces unphysical error at lower N_τ.
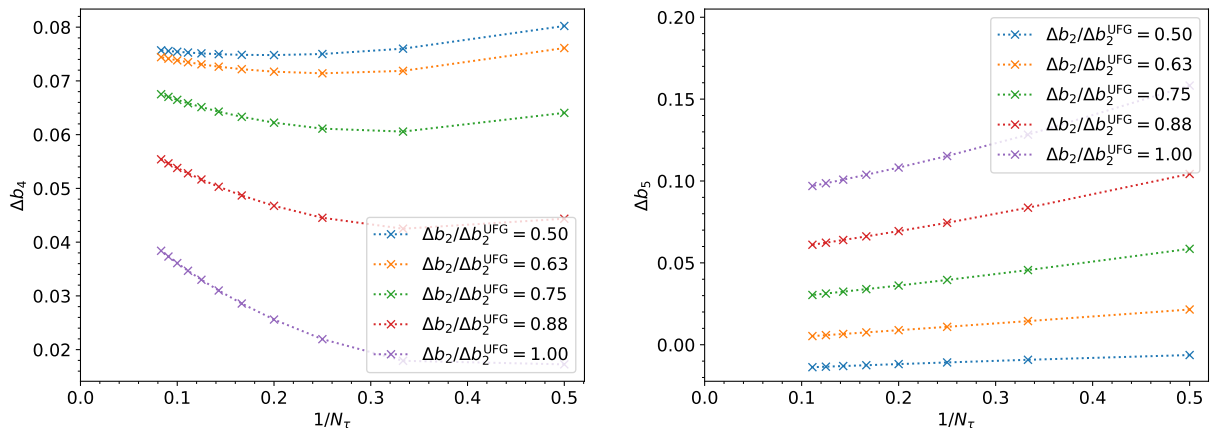
Figure 3.1: Δb_4 (left) and Δb_5 (right) as functions of $1/N_\tau$ for different values of the coupling, parametrized by $\Delta b_2/\Delta b_2^{\mathrm{UFG}}$ as in the main text.

To extrapolate to the $N_\tau \to \infty$ limit, the most straightforward way is to directly extrapolate the curve as shown in Fig. 3.1 to $1/N_\tau = 0$. However, due to the lack of analytic knowledge of the error term, there are no objective and consistent fitting functions applicable to all Δb_n. For example, the Δb_4 and Δb_5 curves in Fig. 3.1 show different asymptotic behaviors. Also, in the case of Δb_4, the non-monotonic convergence curve also makes it even harder to find a proper fitting function.

Therefore, we propose a parameterized approach by extrapolating indirectly through the ratio $C_{\Delta b_n}/C_{\Delta b_2}$ to unify the extrapolation process for all Δb_n. Recall that in the renormalization process, we tune the coupling strength C to reproduce the physical Δb_2 by fitting $\Delta b_2^{(N_\tau)}(C) \equiv \Delta b_2^{\mathrm{analytic}}$. For clarity, this renormalized C is denoted as $C_{\Delta b_2}$. We repeat the same process for a set of values for Δb_n and obtain a series $C_{\Delta b_n}$ for each N_τ.
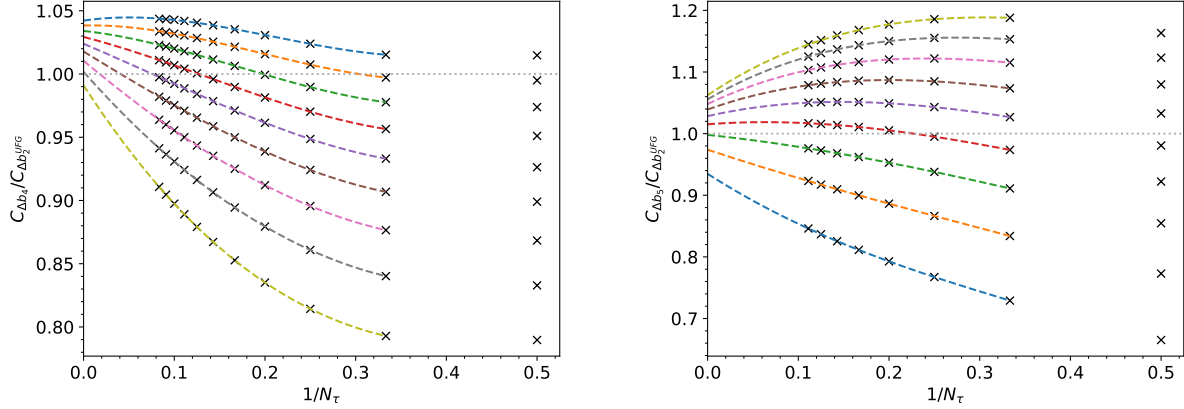
Figure 3.2: $\tilde{C}_{\Delta b_n}/\tilde{C}_{\Delta b_2}^{\text{UFG}}$ as a function of $1/N_\tau$. The left panel is for Δb_4 and right panel for Δb_5. The crosses show the various orders N_τ calculated. The dashed lines show our polynomial fit and extrapolation to large N_τ. The dashed-line endpoints indicate that data beyond that value of N_τ was not included in the fit.

We now have a series of $C_{\Delta b_n}/C_{\Delta b_2}$ ratios as a function of $1/N_\tau$ for a set of given values for Δb_n, as plotted in Fig. 3.2. The ratios are then extrapolated to the $1/N_\tau \to 0$ limit using polynomial fittings, which can be understood as a power series approximating the unknown error term. The intercept then represent if the n-body system of the given Δb_n value shares the same physics, i.e. the same interaction strength, as the two-body system of the target Δb_2. In the end, we obtain the intercept ratio as a function of Δb_n, and use a linear interpolation to pin down the exact value Δb_n that corresponds to $C_{\Delta b_n}/C_{\Delta b_2} = 1$.

To measure the uncertainty of our estimation, we use polynomial fittings at different degree in extrapolating the ratio $C_{\Delta b_n}/C_{\Delta b_2}$ to the large N_τ limit. It yields different spared of intercepts and therefore leads to different interpolation results, as shown in Fig. 3.2. The final estimation is then the average of interpolated results. To calculate the error term σ, we use the half of the difference between the maximum and minimum estimations instead of the standard deviation, because there is no statistical support to assume the errors follow the normal distribution. In the final interpolation, we always use the linear interpolation as the accuracy can be systematically improved by using finer Δb_n value mesh. Finally, to further increase the confidence interval, which cannot be quantified in our case due to the unknown distribution of error terms, we report our estimation error as 2σ, i.e. we add an *ad hoc* error term of the same magnitude.

In short, using the indirect method, we are "double renormalizing" both the two-body and n-body system, and "phase lock" the physical coupling strength, i.e. $C_{\Delta b_n}/C_{\Delta b_2} \to 1$. From a purely
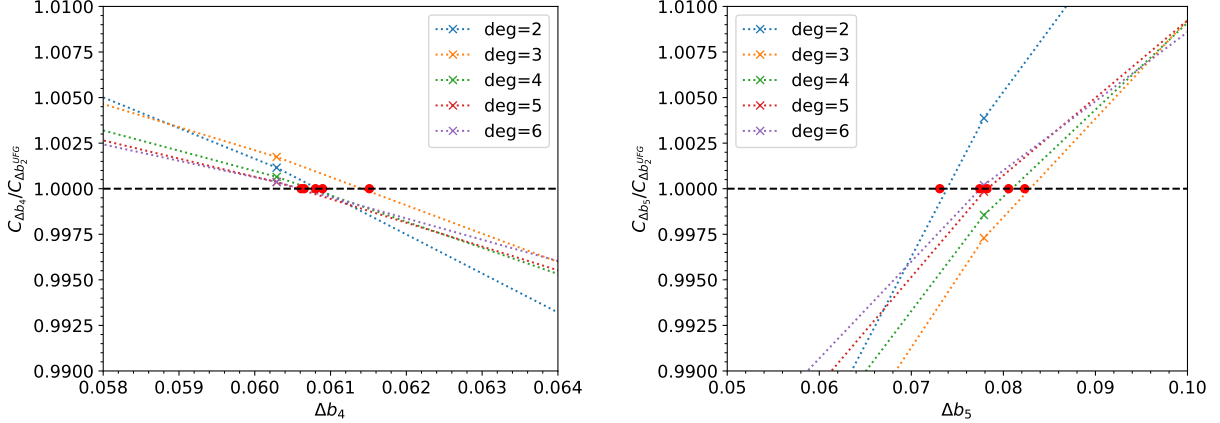
Figure 3.3: Uncertainty estimation from polynomial fits at different degrees for Δb_4 (left) and Δb_5 (right) in the unitary limit.

physical standpoint, this indirect extrapolation scheme is nothing different from the direct way, as both methods are renormalizing the system to the desired two-particle physics. However, we argue from a technical perspective that there is still a slight difference and the extrapolation of $C_{\Delta b_n}/C_{\Delta b_2}$ ratio is more uniform. This is because the underlying assumption behind the extrapolation of the ratio is that $C_{\Delta b_n}/C_{\Delta b_2}$ as a function of $1/N_\tau$ is smooth, and therefore it does not depend on the particle number n. In comparison, when taking the direct extrapolation of Δb_n as a function of $1/N_\tau$, the error term is n-dependent as there are different subspace contributions for different n.

Moreover, another advantage of the indirect method is related to the numerical error. At high N_τ, the polynomial $\Delta b_n(C)$ is of high degree in C with very large coefficients. Tuning such polynomial to reproduce a small Δb_2 (recall that $\Delta b_2^{\mathrm{UFG}} = 1/\sqrt{2} \approx 0.707$) results into C several orders of magnitude smaller, which will then be substituted into $\Delta b_n(C)$. On the contrary, using the ratio of two C at the same order of magnitude helps reduce the exposure to numerical errors. However, considering that we could always use the arbitrary precision calculations to circumvent this problem, its influences are mostly restricted to the application level.

3.2.2: Virial coefficients estimation

Using the methods described above, we report in this section the estimates for Δb_n, for $n = 3, 4, 5$ by extrapolating to the large-k limit with uncertainties. The results are shown in Fig. 3.4, where we parametrize the coupling strength with the ratio $\Delta b_2/\Delta b_2^{\mathrm{UFG}}$. The top panel shows the
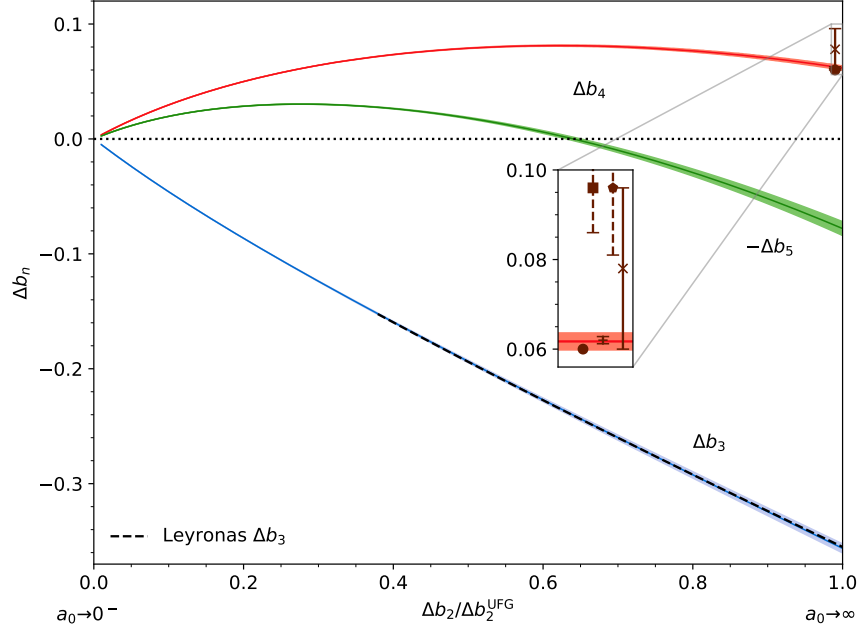
Figure 3.4: Our results for Δb_3 (blue), Δb_4 (red) and $-\Delta b_5$ (green) shown with error bands as functions of the coupling strength given by $\Delta b_2/\Delta b_2^{\mathrm{UFG}}$. [We plot $-\Delta b_5$ to avoid display interference with Δb_4 around unitarity.] The dashed line shows Δb_3 from Ref. [41]. The dark red cross (with errorbar) shows the Monte Carlo results of Ref. [21]: $\Delta b_4^{\mathrm{UFG}} = 0.078(18)$; the dark red plus sign (with small error bar) indicates the conjecture of Ref. [43]: $\Delta b_4^{\mathrm{UFG}} = 0.0620(8)$; finally, the dark red dot shows the approximate results of Ref. [46]: $\Delta b_4^{\mathrm{UFG}} = 0.06$.

results for whole-space virial coefficient Δb_n while the bottom panel shows the subspace virial coefficients Δb_{mj}.

Whole-space virial coefficients

As shown in Sec. 1.4.2, Δb_3 is by now well-understood, and multiple numerical as well as analytical estimations have been given, e.g. Refs. [41, 42, 45, 54, 111]. At unitarity, the unanimous result is $\Delta b_3^{\mathrm{UFG}} \simeq -0.3551\cdots$ [41, 54][4], while our calculation yields $\Delta b_3^{\mathrm{UFG}} = -0.356(4)$. Even though our result is not as precise as the previous unanimity, it only differs by 0.25%. Across the crossover from the noninteracting limit to unitarity, our calculations are in excellent agreement with Leyronas' analytic result [41] (black dashed line) in the regime where the comparison is available.

The red curve is our result for Δb_4, compared with prior theoretical estimates (solid error bar) and experimental determinations (dashed error bar) at unitarity $\Delta b_4^{\mathrm{UFG}}$. Our work extend the

---

[4]The result is truncated for simplicity but the accuracy is enough for our purpose.

results to arbitrary coupling between the noninteracting limit and the unitarity. At unitarity, we obtained $\Delta b_4^{\text{UFG}} = 0.062(2)$, which compares well at face value with every other theoretical estimate, namely Yan and Blume [21]: $\Delta b_4^{\text{UFG}} = 0.078(18)$; Endo and Castin [43]: $\Delta b_4^{\text{UFG}} = 0.0620(8)$, and Ngampruetikorn et al. [46]: $\Delta b_4^{\text{UFG}} = 0.06$. While the last two are a conjecture and an approximate result, respectively, Yan and Blume's is a Monte Carlo result with a comparatively large uncertainty encompassing all prior theoretical estimates. Our calculation, like Yan and Blume's, comes from a first-principle nonperturbative approach but does not incur statistical errors and thus provides a substantial reduction in the overall uncertainty (see also Sec. 2.2.1).

On the experimental side, Δb_4^{UFG} can be determined by fitting to experimental data on the equation of state, e.g. ENS [62]: 0.096(15), and MIT [61]: 0.096(10) (See Sec. 1.4.3 for details). However, those analyses face a challenging numerical problem, namely fitting a fourth-order polynomial with no knowledge of the size of higher order contributions or where the fourth order truly dominates. In fact, as will be discussed soon in Sec. 3.3.2, the assumption of negligible contributions to the density or pressure from $\mathcal{O}(z^5)$ and beyond terms are not supported by our calculations. While the Monte Carlo result of Ref. [21] overlaps with the above analyses, our result disagrees with them (as do Refs. [43, 46]). All the results discussed above are shown in the inset panel of Fig. 3.4, also plotted in Fig. 3.5 for a better visualization.

Lastly, we show the fifth-order virial coefficient as the green curve and flip its sign to fit the layout. We find that Δb_5 starts negative at weak coupling and changes sign from negative to positive around $\Delta b_2/\Delta b_2^{\text{UFG}} \simeq 0.63$. It then proceeds to grow in magnitude enough to overtake Δb_4. At unitarity we obtain $\Delta b_5^{\text{UFG}} = 0.078(6)$, which is the first estimate of this universal quantity, to the best of our knowledge. Crucially, such a large Δb_5 could easily interfere with the experimental determination of Δb_4, which would explain the discrepancies between our results and the experimental equation-of-state analyses of Δb_4. The large magnitude of Δb_5 is notable because the "normal" ordering $|\Delta b_3| > |\Delta b_4| > |\Delta b_5|$ is preserved from weak couplings up to $\Delta b_2/\Delta b_2^{\text{UFG}} \simeq 0.96$, but $|\Delta b_5| > |\Delta b_4|$ after that, in particular at unitarity.

Subspace virial coefficients

For Δb_4 and Δb_5, an interesting difference from Δb_3 is that they are not monotonic functions of the coupling strength. In particular, Δb_5 experienced a sign flip as the system undergoes from
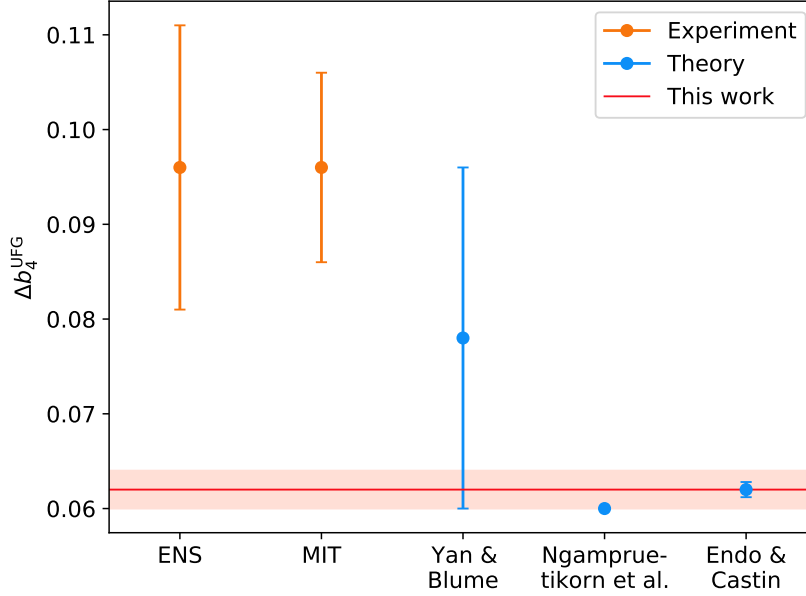
Figure 3.5: Comparison between our calculation of $\Delta b_4^{\mathrm{UFG}}$ and existing results. The red line is our estimation $\Delta b_4^{\mathrm{UFG}} = 0.062(2)$, with shaded region showing the uncertainty. The two orange dots are experimental determination from equation of states by the group from ENS [62] with 0.096(15) and MIT [61] with 0.096(10). The blue dots are numerical or analytical estimations by Yan & Blume [21] with 0.078(18), Ngampruetikorn [46] with 0.06, and Endo & Castin [43] with 0.0620(8).

noninteracting to the unitarity. To better understand the origin of behaviors, we need to dive into the different subspace configurations contributing to Δb_4 and Δb_5. In Fig. 3.6, we plot the subspace contributions to Δb_4 and Δb_5. For completeness, we also include $\Delta b_{21} = \Delta b_3/2$. Note that we flip the sign for Δb_{41} and Δb_{32} in the plot so that they could be more easily compared to their counterparts. Therefore, we roughly divide the plot into two parts with the top panel showing the $M + 1$ subspace contribution and the bottom the $M + 2$ subspace. Nearly all subspace coefficients are monotonic functions of the coupling strength, except for a small weak coupling region in the case of Δb_{32}.

The subspace contributions Δb_{mj} allow us to study the first steps of the "polaron sequence" Δb_{m1}. Beyond the qualitative resemblance of $|\Delta b_{m1}|$ for all m, we find that $|\Delta b_{m1}|$ decreases as m is increased for all the couplings we studied (see Table 3.2 in particular), which we interpret as due to the largely noninteracting majority particles (as the interaction is of zero range). In the $m \to \infty$ limit, the system effectively approaches the noninteracting limit. Furthermore, we observe that the sequence alternates in sign, which we conjecture will persist for arbitrary m.

For the Δb_{m2} sequence, we only have two samples but also observe the different sign between
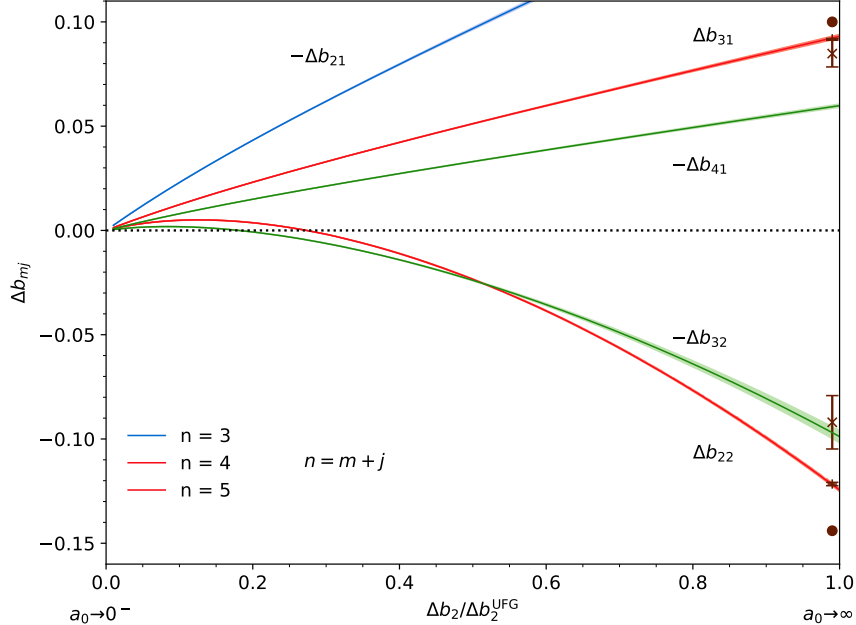
Figure 3.6: Subspace contributions Δb_{mj} as functions of the coupling strength. Our results are shown as error bands, color-coded as in the top plot by $n = m + j$: blue for Δb_{21}, red for Δb_{31} and Δb_{22}, and green for Δb_{41} and Δb_{32}. The red cross (with errorbar) shows Ref. [21]: $\Delta b_{31}^{\text{UFG}} = 0.0848(64)$ and $\Delta b_{22}^{\text{UFG}} = -0.0920(128)$; the red dot shows Ref. [46]: $\Delta b_{31}^{\text{UFG}} = 0.100$ and $\Delta b_{22}^{\text{UFG}} = -0.144$; finally, the red plus sign (with small error bar) shows Ref. [43]: $\Delta b_{31}^{\text{UFG}} = 0.09188(16)$ and $\Delta b_{22}^{\text{UFG}} = -0.1220(8)$. Our results are closest to the latter; we obtain $\Delta b_{31}^{\text{UFG}} = 0.0931(8)$ and $\Delta b_{22}^{\text{UFG}} = -0.1244(7)$.

Δb_{22} and Δb_{32} and $|\Delta b_{22}| > |\Delta b_{32}|$ for most couplings. Moreover, Δb_{m2} is more susceptible to the interaction strength than Δb_{m1}, leading to larger magnitudes for Δb_{m2} at unitarity.

In the subspace, we find more monotonic behavior of Δb_{mj} as a function of the coupling strength. For essentially all couplings studied, Δb_{31} is increasingly positive and Δb_{22} increasingly negative as unitarity is approached. Their competition eventually results in the non-monotonic behavior of Δb_4 in Fig. 3.4, and reaches its low value at unitarity.

Fig. 3.6 also yields a more detailed comparison with prior theoretical approaches at unitarity. Specifically, at the 95% confidence level, i.e. using the 2σ error bar discussed above,[5] our result for Δb_{31} overlaps with Endo and Castin [43] but not with Yan and Blume [21] nor with Ngampruetikorn *et al.* [46]. On the other hand, at the same level our Δb_{22} also overlaps with Endo and Castin [43] and marginally with Yan and Blume [21], but not with Ngampruetikorn et al. [46]. This analysis suggests that the closer agreement for Δb_4 at unitarity shown in Fig. 3.4 is due at

---

[5]with the caveat that it is strictly speaking unknown whether the errors are normally distributed

Table 3.2: Estimates for Δb_3 to Δb_5 in the unitary limit, including the subspace coefficients for the polarized case Δb_{mj}.

	$n = 3$	$n = 4$	$n = 5$
$\Delta b_n^{\mathrm{UFG}}$	-0.356(4)	0.062(2)	0.078(6)
$\Delta b_{(n-1)1}^{\mathrm{UFG}}$	-0.178(2)	0.0931(8)	-0.0598(7)
$\Delta b_{(n-2)2}^{\mathrm{UFG}}$	–	-0.1244(7)	0.0988(29)

least in part to error compensation between Δb_{31} and Δb_{22}.

As with Δb_4, the non-monotonicity of Δb_5 can also be traced back to the competition be-tween two sectors with (largely) monotonic but opposite behavior. Shown as the green curves in Fig. 3.6, Δb_{41} and Δb_{32} become progressively more negative and more positive, respectively, as the coupling is increased (with the exception of a small region at very weak couplings where Δb_{32} is negative). Thus, $\Delta b_5 = 2\Delta b_{41} + 2\Delta b_{32}$ becomes non-monotonic. Furthermore, the same factor for Δb_{41} and Δb_{32} indicates that the $(3 + 2)$ subspace plays a more dominant role compared to the four-particle case, contributing to the stronger non-monotonicity of Δb_5 and the sign flip. In other words, the $(3 + 2)$-space contributes to Δb_5 on the same footing as the $(4 + 1)$ space, while for Δb_4 the contribution from $(2 + 2)$-system is effectively halved compared to that from $(3 + 1)$-system. As a result, the $(3 + 2)$-space becomes more dominant as the interaction grows stronger.

Finally, we note that our analysis of Δb_{mj}, and their apparent more systematic behavior, sug-gests that the conjectures as in Ref. [56, 63, 64] on the high-order virial coefficients in the unitary limit may be refined by focusing on the subspaces rather than the full Δb_n.

Section 3.3: Thermodynamics and Tan's Contact of Unitary Fermi Gas

3.3.1: Pressure state equation

First of all, we examine the pressure equation of state, which is directly related to grand po-tential via $\Omega = -PV$, and therefore we have

$$\beta\Delta P = \frac{2}{\lambda_T^3} \sum_{n=2}^{\infty} \Delta b_n z^n. \tag{3.4}$$

Due to its direct connection with the grand potential, it offers a benchmark to check our estima-tions on the virial coefficients and examine the resummation methods.

In Fig. 3.7, we plot as a function of fugacity z the pressure P/P_0 in unit of its noninteracting
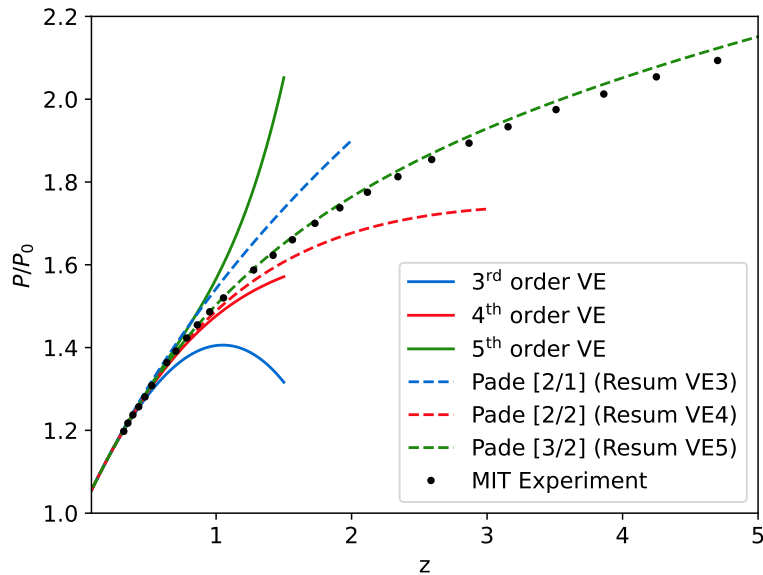
Figure 3.7: Pressure equation of state at unitarity as a function of the fugacity z showing our virial expansion results (error bands) compared with the data of Ref. [61].

counterpart P_0 given as

$$\beta P_0 = \frac{2}{\lambda_T^3} f_{5/2}(z), \tag{3.5}$$

where $f_{5/2}$ is the Fermi-Dirac function and calculated by numerically integrating the Fermi-Dirac integral instead of using the truncated polylogarithm series, i.e. the noninteracting physics is fully encoded. For reference, we also show the experimental determinations from Ref. [61]. The solid lines are the results using the truncated virial expansion. As expected, all three curves diverge from the experimental values as z increases, but higher-order expansion shows larger regime of convergence. We also examine the Padé resummations using different order of expansion. In each case, we choose the Padé approximant at either central or off-central order. Compared to the bare results, the resummed results present better agreements and larger regime of convergence. We observed the resummed third-order expansion nearly collapse with the bare fifth-order result for $z < 1$. In particular, the resummed fifth-order result agree quantitatively with the experimental determinations up until fugacity as large as $z \approx 3$, even after which the resummed result is still convergent and follows the trend to larger fugacity. Such excellent agreement indirectly
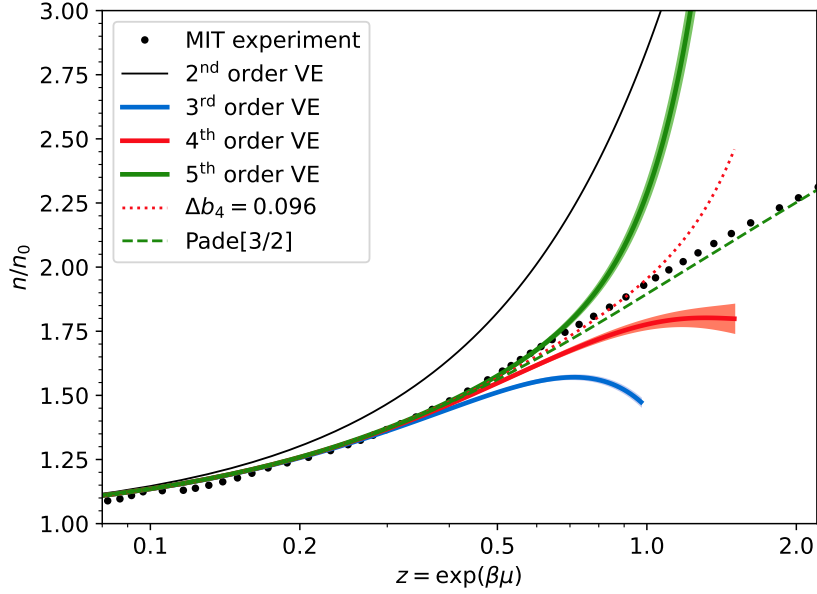
Figure 3.8: Density equation of state at unitarity as a function of the fugacity z showing our virial expansion results (error bands) compared with the data of Ref. [61]. The fourth-order virial expansion is also shown as red dotted line using the experimental determination for Δb_4 of 0.096 [61, 62]. At last, the green dashed line is the resummed fifth-order results with Padé order [3/2].

supports the accuracy of our estimations on Δb_n. Moreover, the surprising convergence of the resummed results shows a promising direction in applying QVE, i.e. by including to higher-order terms, whose contributions were previously considered negligible, and implementing mathematical techniques, we may improve the series convergence well beyond $z = 1$.

3.3.2: Density state equation

For the density equation of state as given in Eq.(1.34), the interaction-induced change in density is expressed as

$$\Delta n = \frac{Q_1}{V} \sum_{n=2}^{\infty} n \Delta b_n z^n = \frac{2}{\lambda_T^3} \sum_{n=2}^{\infty} n \Delta b_n z^n. \tag{3.6}$$

The noninteracting result is given in Eq. (1.27),

$$n^{(0)} = \frac{2}{\lambda_T^3} f_{\frac{3}{2}}(z), \tag{3.7}$$

where $f_{3/2}(z)$ is the Fermi-Dirac function and evaluated the same way as shown before. We plot the ratio $n/n^{(0)} = 1 + \Delta n/n^{(0)}$ as a function of fugacity z in Fig. 3.8 and compare with the experiment of Ref. [61].

The solid curves are results using the above series of different order at its face value, i.e. the truncated series, with the shaded region as the propagated error using the 2σ error in Δb_n. While our results at fourth order are somewhat farther away from the data than those of Ref. [21] (the red dashed curve), the fifth-order contribution considerably improves the agreement for $z = 0.5 - 0.73$. Such improvement further indicates the non-negligible fifth-order contribution. We also plot the truncated fourth-order series with the experimental determination $\Delta b_4 = 0.096$ as the red dotted line, which agrees with the experimental density nearly perfectly up until $z = 1$. Such agreement demonstrates how the experimental determination overestimates Δb_4 when neglecting the fifth- and higher-order contributions. The Padé-resummed result at order [3/2] are plotted as the black dashed line and find agreement with the experimental data up until $z = 4$ (the horizontal limit of the plot is capped at 2 for better comparison).

Lastly, in Fig. 3.9, we show a comparison of the density equation of state, following closely the style of Fig. 5 of Ref. [100]. By plotting the scaled density deviations from the third-order virial expansion $(n - n_{\text{virial}}^{(3)})/(8z^4)$, the authors of Ref. [100] showed how their diagrammatic Monte Carlo data compares with previous work on the fourth-order virial coefficient coming from experiments and theory. The red line shows the function $\Delta b_4 + z \cdot \Delta b_5$ and the shaded region encodes the uncertainty estimations. For small z, such linear relation successfully meet the diagrammatic results at $z = 0.2$. However, at z increases, the relation becomes apparently nonlinear, indicating the non-negligible role of higher-order terms.

3.3.3: Tan's contact

In a series of works [113–115] in 2008, Shina Tan derived a set of universal relations around a quantity referred as Tan's contact $\mathcal{I}$, or just contact for short. Physically the contact captures the the short-distance and high-frequency behavior of correlation functions for short-range interactions. Furthermore, Tan (and later others) reveals that via a set of universal relation, the contact are related to thermodynamic and other properties. For example, the famous tail of the momentum distribution relation states that the distribution of momentum has a power-law tail at large k
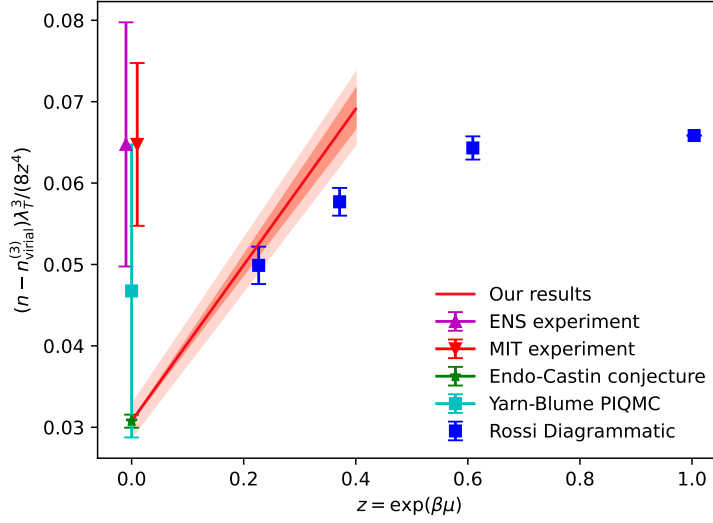
Figure 3.9: Density equation of state n of the unitary Fermi gas, relative to the corresponding third-order virial expansion, in units of the thermal wavelength λ_T, as a function of the fugacity z. The red solid line is $\Delta b_4 + \Delta b_5 z$ using our estimations. The shaded region represents the uncertainty, where the outermost light shaded region shows the uncertainty in both Δb_4 and Δb_5, while the darker shaded region shows only the uncertainty in Δb_5. For comparison, the same experimental results of Refs. [61, 62] are shown alongside the theoretical predictions of Refs. [21, 100, 112].

as (see also Ref. [116])

$$\mathcal{I} = \lim_{k \to \infty} k^4 n_s(k). \tag{3.8}$$

Through the adiabatic relation, the contact is connected to the energy through

$$\frac{\hbar^2}{4\pi m}\mathcal{I} = \left[\frac{\partial E}{\partial(-1/a_s)}\right]_{S,N} \tag{3.9}$$

The third relation relates the short-distance pair density to contact density as

$$\left\langle n_\uparrow(\mathbf{R} + \frac{1}{2}\mathbf{r})n_\downarrow(\mathbf{R} - \frac{1}{2}\mathbf{r})\right\rangle \to \frac{1}{16\pi^2}\left(\frac{1}{r^2} - \frac{2}{a_s r}\right)\mathcal{I}(\mathbf{R}). \tag{3.10}$$

In this sense, the contact density can be interpreted as the density of a two-body pair separated by a short distance $\mathbf{r}$. There are many more relations connecting the contact to various quantities and for more studies on the contact, see Tan's original works as well as e.g. Refs. [117–128] Due to its relations to that many quantities, the contact is a crucial piece of the thermodynamic

puzzle that complements conventional quantities and attracts significant attentions.

In this section, we consider only the system in 3D and will revisit the 1D and 2D case in the next chapter. In practice, we use the adiabatic relation to calculate Tan's contact, which differentiates with respect to the coupling $\lambda = \sqrt{\beta}/a_0$. As our results give Δb_n as a function of Δb_2 rather than the physical coupling, we also use the chain rule in the derivative. In the end, we have

$$\mathcal{I} = -\frac{4\pi}{\beta} \frac{\partial(\beta\Omega)}{\partial a_0^{-1}} = \frac{4\pi}{\sqrt{\beta}} \frac{\partial \ln \mathcal{Z}}{\partial \Delta b_2} \frac{\partial \Delta b_2}{\partial \lambda}, \tag{3.11}$$

Thus,

$$\mathcal{I} = \frac{8\pi^2}{\lambda_T} Q_1 \sum_{m=2}^{\infty} c_m z^m, \tag{3.12}$$

and we define the contact coefficient c_m as

$$c_m = \frac{1}{\sqrt{2\pi}} \frac{\partial \Delta b_m}{\partial \Delta b_2} \frac{\partial \Delta b_2}{\partial \lambda}. \tag{3.13}$$

For the second order, Beth-Uhlenbeck formula yields

$$\frac{\partial \Delta b_2}{\partial \lambda} = \sqrt{\frac{2}{\pi}} + \sqrt{2}\, \lambda\, e^{\lambda^2}(1 + \mathrm{erf}(\lambda)), \tag{3.14}$$

such that

$$c_2 = \frac{1}{\pi} + \frac{1}{\sqrt{\pi}}\, \lambda\, e^{\lambda^2}[1 + \mathrm{erf}(\lambda)]. \tag{3.15}$$

To evaluate higher-order c_n, we take the numerical differentiation to estimate $\partial \Delta b_n / \partial \Delta b_2$ for $n = 3, 4, 5$ at a fine mesh of $\Delta b_2 / \Delta b_2^{\mathrm{UFG}}$. Thanks to the analytical nature of our method, it takes no extra computations to adjust the mesh and therefore we could easily improve the quality of numerical differentiation in a systematical way. The results are shown as solid lines in Fig. 3.10.

Though the curves are overall smooth, there are some jigsaw-like shaded regions for Δb_4 near the unitary limit, which are the numerical artifacts due to the numerical differentiation. To that
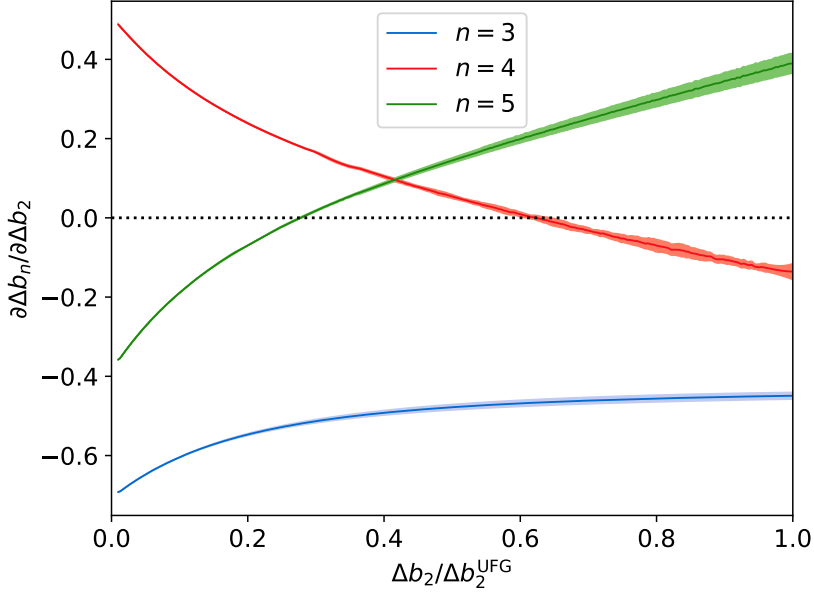
Figure 3.10: Derivative of Δb_n with respect to Δb_2 as a function of the coupling.

end, we implemented a second way to estimate the contact coefficients c_n without involving the numerical differentiation.

Recall that in our method, we have Δb_n as a polynomial of C in form of

$$\Delta b_n = \sum_{l}^{l_{\max}} A_l C^l, \tag{3.16}$$

where $l_{\max} = \lfloor n/2 \rfloor \cdot N_\tau$, then the derivative is

$$\frac{\partial \Delta b_n}{\partial \lambda} = \sum_{l=1}^{l_{\max}} l \cdot A_l C^{l-1} \frac{\partial C}{\partial \lambda} \equiv D \cdot \sum_{l=1}^{l_{\max}} l A_l C^{l-1}, \tag{3.17}$$

Now, we treat C and $D \equiv \partial C/\partial \lambda$ as two "independent" bare coupling strengths to be renormalized to the true physics. We take a two-pass renormalization process at each N_τ: firstly we renormalize C to reproduce the expected Δb_2 and then substitute the physical C into Eq. (3.17) to calculate D using the physical c_2 given in Eq. (3.15). In the end, we use the same extrapolation scheme to reach $N_\tau \to \infty$ limit to obtain the estimation for c_m.

In Fig. 3.11 we compare our results for the Tan contact with the both experimental measurements of Refs. [61, 129] and theoretical calculations of Refs. [130–134]. For easier comparisons

among different works, we use the dimensionless, thermodynamically intensive form $\mathcal{I}/(Nk_F)$ given as

$$\frac{\mathcal{I}}{Nk_F} = 3\pi^2(4\pi)^2 \frac{1}{k_F^4 \lambda_T^4} \sum_{n=2}^{\infty} c_n z^n = 3\pi^2 \left(\frac{T}{T_F}\right)^2 \sum_{n=2}^{\infty} c_n z^n, \tag{3.18}$$

where we used $Q_1 = 2V/\lambda_T^3$, $k_F^3 = 3\pi^2 n$ and $n = N/V$ in the first identity, and $T_F = k_F^2/2$ and $T = 2\pi/\lambda_T^2$ in the second one. The dimensionless temperature T/T_F is related to the dimensionless density ρ via

$$\rho \equiv \lambda_T^3 n/2 = 4/(3\sqrt{\pi})(T_F/T)^{3/2}, \tag{3.19}$$

which can be expressed as expansion

$$\rho = \rho_0 + \sum_{n=2}^{\infty} n\Delta b_n z^n, \tag{3.20}$$

and ρ_0 is the dimensionless noninteracting density, i.e. the Fermi-Dirac function $f_{3/2}(z)$ by itself.

Section 3.4: Spin-polarized unitary Fermi gas

Another system of great interests is the spin-polarized UFG for e.g. the potential exotic polarized superfluid phase (see e.g. Refs [135–137]) or its connection to the long-sought pseudogap phase (see Sec. 3.4.5). In Sec. 1.3.3, we introduce the notation $\mu = (\mu_\uparrow + \mu_\downarrow)/2$ as the average chemical potential, and $h = (\mu_\uparrow - \mu_\downarrow)/2$ as the polarization. Similarly, we defined $z = \exp(\beta\mu)$ and $z_s = \exp(\beta\mu_s)$ for $s = \uparrow, \downarrow$. With the GCPF expressed in terms of Δb_{mj} in Eq. (1.58), we then have

$$\ln(\mathcal{Z}/\mathcal{Z}_0) = Q_1 \sum_{m=2}^{\infty} \sideset{}{'}\sum_{ij} \Delta b_{ij} z_\uparrow^i z_\downarrow^j, \tag{3.21}$$

where the primed sum is subject to $i + j = m$ and $i, j > 0$. We will use a different summation index convention temporarily in this section to avoid the ambiguity from the density n. The whole-space index is now denoted as m while the subspace subscripts as i and j.

It is more common to express the series in terms of $z = \exp(\beta\mu)$ and $\exp(\beta h)$. For example,
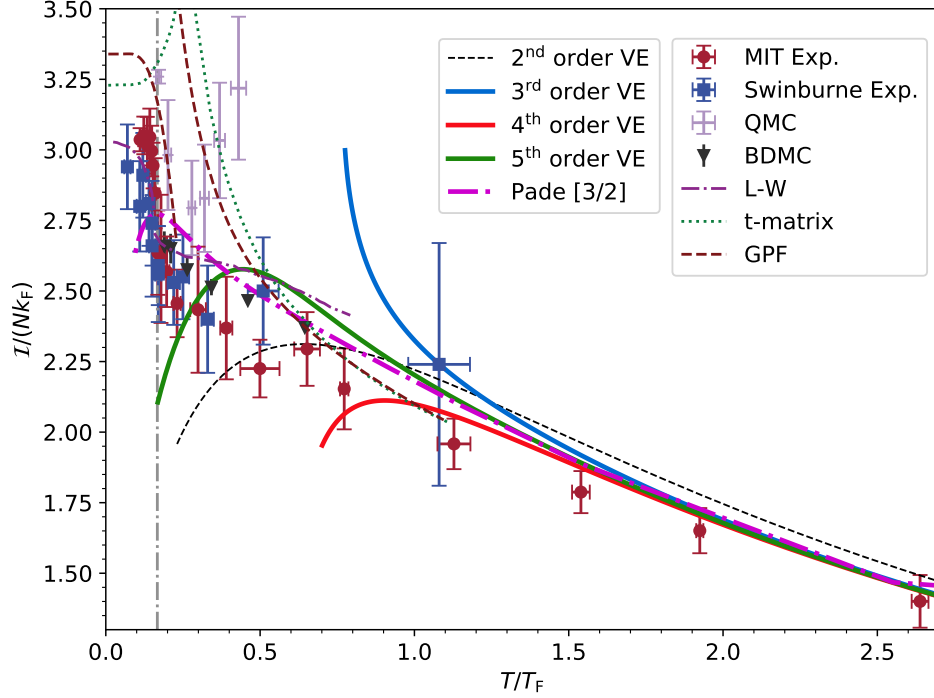
Figure 3.11: Dimensionless contact $\mathcal{I}/(Nk_F)$ as a function of the dimensionless temperature T/T_F. Our virial expansion results at different orders are shown as thick solid line in blue (3$^{\text{rd}}$ order), red (4$^{\text{th}}$ order), and green (5$^{\text{th}}$ order). The solid purple line is the result using Padé approximant at order [3/2] on the sum series to fifth order. The gray dashed line shows the critical temperature $T_c/T_F = 0.167$. Also shown are the experimental measurements from Ref. [61] (dark red data with error bars); the experimental measurements from Ref. [129] (dark blue squares); the Quantum Monte Carlo (QMC) estimates from Ref. [130] (light purple plus signs); the bold-diagrammatic QMC estimates from Ref. [131] (gray triangles); the Luttinger-Ward (LW) results from Ref. [132] (purple dash-dot line); the T-Matrix calculation from Ref. [133] (green dotted line); and the Gaussian-pair-fluctuation theory (GPF) estimates from Ref. [134] (dark red dashed line).

for $n = 3$, the primed sum is

$$\sum_{i+j=3} z_\uparrow^m z_\downarrow^j \Delta b_{ij} = z_\uparrow^2 z_\downarrow \Delta b_{21} + z_\uparrow z_\downarrow^2 \Delta b_{12} = z^3 \left[2 \cosh(\beta h) \right] \Delta b_{21}, \tag{3.22}$$

i.e. the polarized whole-space coefficient Δb_3 now becomes polarization-dependents as $\Delta b_3 = [2 \cosh(\beta \eta)] \Delta b_{21}$, which reduced to the unpolarized results $\Delta b_3 = 2 \Delta b_{21}$ in the limit $\beta h \to 0$. In such form, the series is converted to the polynomials in z with polarization-dependent coefficients, and therefore we can use the same procedures as in the spin-balanced case to the polarized Fermi gases.
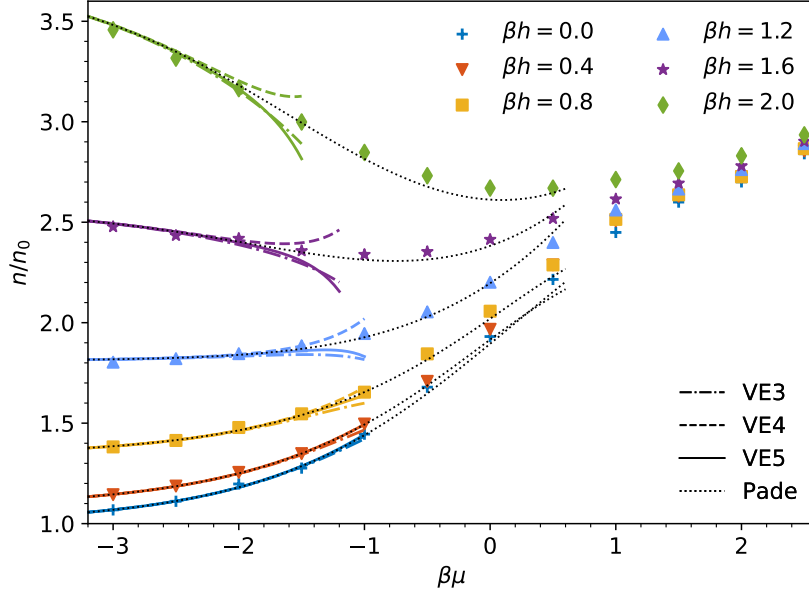
Figure 3.12: Density equation of state n of the unitary Fermi gas, shown in units of the noninteracting, unpolarized counterpart n_0, for several values of the chemical potential difference βh. The colored symbols are complex-Langevin results from Ref. [138] and the colored lines show the virial expansion at various orders: dashed-dotted line at third order, dashed line at fourth order, and solid line at fifth order. The black dotted line is the result of the [3/2] Padé resummation. The limiting value for $\beta\mu \to -\infty$ is known exactly and is given by $\cosh(\beta h)$.

3.4.1: Density equation of state

The polarized density is expressed in terms of subspace coefficients

$$\Delta n = \frac{2}{\lambda_T^3} \sum_{m=2}^{\infty} m {\sum_{ij}}' \Delta b_{ij} z_\uparrow^i z_\downarrow^j. \tag{3.23}$$

To apply the resummation technique, we rewrite the series in Eq. (3.23) in powers of as $z = \exp(\beta\mu)$ with coefficients as functions of $\exp(\beta h)$. In our case, we have the series up to the fifth order as

$$\sum_{m=2}^{5} m {\sum_{ij}}' \Delta b_{ij} z_\uparrow^i z_\downarrow^j$$
$$= z^2 \Delta b_{11} + z^3 \, 3[2\cosh(\beta h)\Delta b_{21}]$$
$$+ z^4 \, 4[2\cosh(2\beta h)\Delta b_{31} + \Delta b_{22}] + z^5 \, 5[2\cosh(3\beta h)\Delta b_{41} + 2\cosh(\beta h)\Delta b_{32}]. \tag{3.24}$$

In Fig. 3.12, we present our results for the polarized density equation of state in the unitary

limit and compare with the complex-Langevin results of Ref. [138]. The fifth-order expansion shows the best agreement compared to its lower-order counterparts, although the improvement is mostly marginal. When applying the Padé resummation technique, however, the agreement with the data is extended even beyond $\beta\mu = 0$. Notably, the change in curvature displayed by the data is reproduced by the Padé approximant. Beyond $\beta\mu = 0.6$, however, the Padé approximant progressively departs from the data.

3.4.2:   Tan's contact of spin-imbalanced system

In terms of subspace contributions, the contact is

$$\mathcal{I} = \frac{4\pi}{\beta} Q_1 \lambda_T \sum_{m=2}^{\infty} \sideset{}{'}\sum_{ij} c_{ij} z_\uparrow^i z_\downarrow^j, \tag{3.25}$$

where c_{mj} is defined as, in analogue to Eq. (3.13),

$$c_{ij} = \frac{1}{\sqrt{2\pi}} \frac{\partial \Delta b_{ij}}{\partial \Delta b_{11}} \frac{\partial \Delta b_{11}}{\partial \lambda}, \tag{3.26}$$

note that $\Delta b_2 = \Delta b_{11}$. The subspace contact coefficients c_{ij} are related to the whole-space contact coefficient c_m in the same way as the virial coefficients case.

The dimensionless contact is now defined as

$$\frac{\mathcal{I}}{2N_\downarrow k_{F\uparrow}} = 3\pi^2 \left(\frac{T}{T_{F\uparrow}}\right)^2 \left(\frac{n_\uparrow}{n_\downarrow}\right) \sum_{m=2}^{\infty} \sideset{}{'}\sum_{ij} c_{ij} z_\uparrow^i z_\downarrow^j. \tag{3.27}$$

where we used $k_{F\uparrow}^3 = 6\pi^2 n_\uparrow$. The dimensionless temperature $T/T_{F\uparrow}$ is related to the spin-$\uparrow$ dimensionless density $\rho_\uparrow$ via

$$\rho_\uparrow = \lambda_T^3 n_\uparrow = 4/(3\sqrt{\pi})(T_{F\uparrow}/T)^{3/2}, \tag{3.28}$$

and ρ_s is given by

$$\rho_s = f_{3/2}(z_s) + 2 \sum_{m=2}^{\infty} \sideset{}{'}\sum_{ij} [i\delta_{s,\uparrow} + j\delta_{s,\downarrow}] b_{ij} z_\uparrow^i z_\downarrow^j. \tag{3.29}$$

In practice, we fix the impurity concentration $n_\downarrow/n_\uparrow$ and, for a given $z_\uparrow$, one can first solve

73
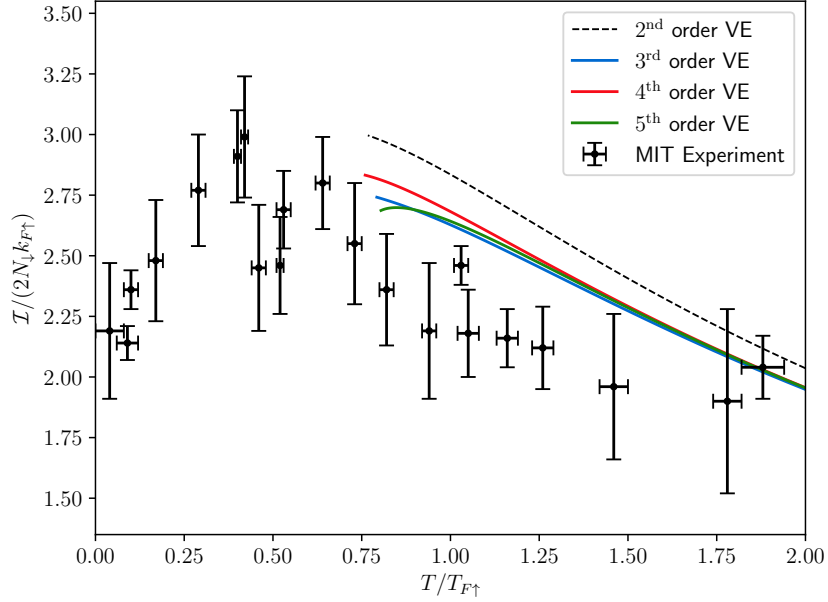
Figure 3.13: The spin-imbalanced contact $\mathcal{I}/(N_\downarrow k_{F\uparrow})$ as a function of temperature $T_{F\uparrow}/T$. The black circles shows the experimental measurements from Ref. [139] at impurity concentration of 10%, the solid curves are the results of virial expansion.

for $z_\downarrow$ using the above equations and then calculate the dimensionless contact $\mathcal{I}/(2N_\downarrow k_{F\uparrow})$ and dimensionless temperature $T/T_{F\uparrow}$. In Fig. 3.13, we compare the result of virial expansion to experimental measurements [139] with impurity concentration of 10%.

Finally, we note for future reference that, in the noninteracting limit,

$$\frac{\mathcal{I}}{2N_\downarrow k_{F\uparrow}} = 2^{3/2}\sqrt{\pi}\left(\sqrt{2}-1\right)\sqrt{\frac{T}{T_{F\uparrow}}}n_\uparrow\lambda_T^3. \tag{3.30}$$

3.4.3: Magnetization

Another set of properties of interest in the presence of the spin imbalance is the magnetic properties such as the magnetization $m = n_\uparrow - n_\downarrow$. We usually present the magnetization m in its dimensionless form

$$\overline{m} = \frac{m}{n(\beta h = 0)}. \tag{3.31}$$

where $n(\beta h = 0)$ is the density of the interacting system in the unpolarized limit $\beta h \to 0$. With Eq. (3.29), we calculate the dimensionless magnetization $\overline{m} = m/n(\beta h = 0)$ with QVE and plot

74

the results as a function of βh at $\beta \mu = -3, -2, -1$ and 0 in Fig. 3.14 and compared to a selection of QMC calculations from Ref. [138].

For $\beta \mu = -3, -2$ and -1, we plot the truncated QVE results at different order and observe (slightly) improved convergence and better agreement with the QMC result. At $\beta \mu = -1$, we find the results using QVE at its face value start to diverge for large βh, indicating the decreasing in radius of convergence as the polarization-dependent coefficients varies. At $\beta \mu = 0$, we omitted the truncated QVE results from the plot as the series diverge immediately at $\beta h = 0$.

The resummation technique is applied in the same way as shown in Eq. (3.24). In the end, we have the series up to the fifth order for the spin-up case as

$$
\begin{aligned}
\sum_{m=2}^{5} \sum_{ij}{}' i\, b_{ij} z_\uparrow^i z_\downarrow^j =& z^2 \Delta b_{11} + z^3 (2\mathrm{e}^{\beta h} + \mathrm{e}^{-\beta h}) \Delta b_{21} \\
& + z^4 \left[(3\mathrm{e}^{2\beta h} + \mathrm{e}^{-2\beta h}) \Delta b_{31} + 2\Delta b_{22} \right] \\
& + z^5 \left[(4\mathrm{e}^{3\beta h} + \mathrm{e}^{-3\beta h}) \Delta b_{32} + (3\mathrm{e}^{\beta h} + 2\mathrm{e}^{-\beta h}) \Delta b_{32} \right]
\end{aligned}
\tag{3.32}
$$

and a similar equation for the spin-down case with slightly different factors in the coefficient. We apply the Padé approximant at order [2/3] (purple dash-dotted lines) and find excellent agreement throughout all βh examined. We note that in Ref. [138], authors also studied the case of $\beta \mu = 1$ and 2. However even the resummed results failed to converge in this case, indicating that higher-order terms are needed, i.e. for denser system, the contribution from higher-body subsystem becomes more important.

3.4.4: Compressibility

Another set of important properties for a polarized system is the response properties. Here, we consider the spin and density susceptibility, which are denoted as χ_s and χ_n respectively, and defined as

$$
\chi_{n/s} = \frac{\partial(n_\uparrow \pm n_\downarrow)}{\partial(\mu_\uparrow \pm \mu_\downarrow)}
\tag{3.33}
$$

where $+$ sign is for χ_n and $-$ sign for χ_s. In this section, we will focus on the density susceptibility χ_n and leave χ_s to the next.

The density susceptibility is also called the normalized compressibility as it is related to the
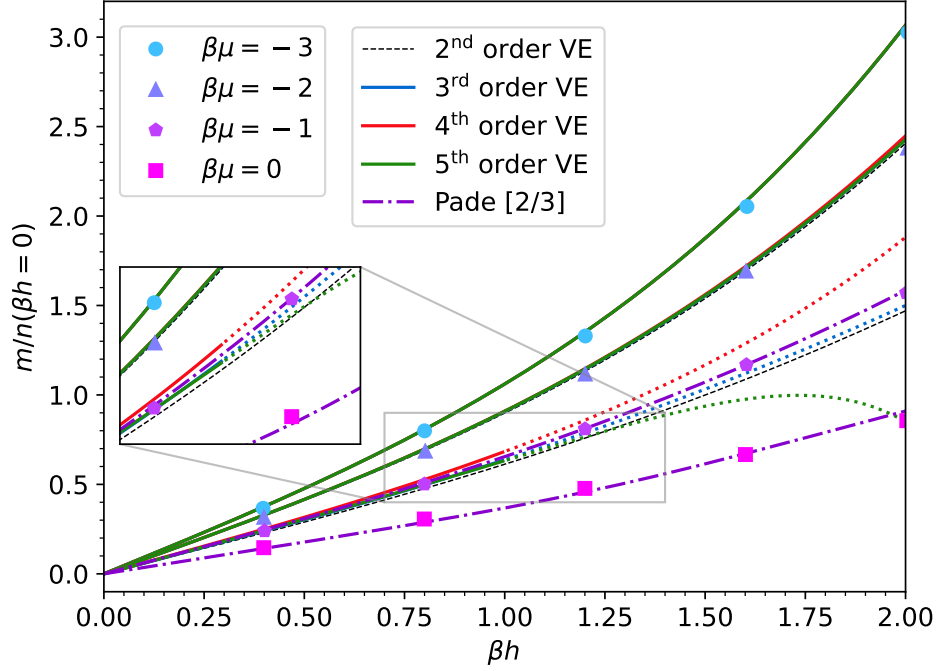
Figure 3.14: Dimensionless magnetization $\overline{m} = m/n_0(\beta h = 0)$ as a function of dimensionless chemical potential difference βh. The circles ($\beta\mu$ = -3), triangles ($\beta\mu$ = -2), pentagons ($\beta\mu$ = -1) and squares ($\beta\mu = 0$) are the QMC calculations from Ref. [138] for different values of $\beta\mu$. Note that only the results relevant to the virial expansion are presented here. The blue, red, and green curves show the result of truncated QVE at third, fourth, and fifth order respectively. The black dashed line is the second order QVE result for reference. For $\beta\mu = -1$, part of the curve is shown as a dotted line in the regime when the QVE at its face value starts to diverge for better visibility. Due to the immediate divergence, we do not show the truncated series results for $\beta\mu = 0$. The purple dash-dotted lines are the Padé approximation at order [2/3] for $\beta\mu = -1$ and 0, showing excellent agreement with the QMC calculations. The inset shows a closer view of the comparison between the virial expansion and QMC results, from which it is clear that the fifth-order virial expansion yields an improved estimate.

isothermal compressibility κ via

$$\chi_n = n^2 \kappa, \tag{3.34}$$

and κ is defined as

$$\kappa = -\frac{1}{V}\left[\frac{\partial V}{\partial P}\right]_T = \frac{\beta}{n^2}\left[\frac{\partial n}{\partial \beta\mu}\right]_T. \tag{3.35}$$

The partial derivative is expressed in form of series as

$$\frac{\partial n}{\partial(\beta\mu)} = \frac{\partial n_0}{\partial(\beta\mu)} + \sum_{m=2}^{\infty} m^2 \sum_{i+j=m} \Delta b_{ij} z_\uparrow^i z_\downarrow^j. \tag{3.36}$$

76

In Fig. 3.15, we present our estimates for the compressibility κ in the unitary limit as a function of T/T_F, represented in the dimensionless form scaled by its noninteracting counterpart $\kappa_0 = 3/(2n\epsilon_F)$. We compare our results with the experimental measurements from Ref. [61], the Luttinger-Ward calculations of Ref. [140], and the complex-Langevin results from Ref. [138], Similar as we did in Sec. 3.3.2, we investigated the performance of different the resummation methods for this more complicated observables. The results of Padé and Borel-Padé resummations show much better agreement with experimental data than the bare finite-order virial expansion, and work well beyond the convergence region $z \ll 1$ for the truncated series. Specifically, the resummations smoothly follow the trend of the experimental data up to fugacity as large as $z = 10$ (maximum fugacity shown in Fig. 3.15), which is surprising considering that the superfluid transition occurs at $z \simeq 10$. For Padé approximants at different orders, we compare [2/1] (use up to Δb_3), [2/2] (use up to Δb_4) and [3/2] (use up to Δb_5). Though the resummed [2/1] result deviates from others around $T/T_F \approx 1$, it shows comparable performance as the fifth-order virial expansion at its face value. The resummed fourth- and fifth order results agree with other works to very low temperature around 0.25. However, such agreement should be taken with a salt as there is no guarantee whether such convergence is coincidental. The improvements over the third-order resummation at [2/1] supports our early argument that the lack of higher-order coefficients limits systematic study of resummation method in the context of QVE.

One may have noticed that at low temperature, the resummed fifth-order result (green dash-dotted line) seems to perform worse compared to the fourth-order result (red dash-dotted line). Considering the uncontrollability of the resummed method, we cannot draw from it conclusions such as the central-order approximant is better or the fifth-order coefficients is not accurate. Further work on sixth- and higher-order coefficients are required for more systematic investigations.

We then compare the Borel-Padé method and the Padé method, and found no significant difference as the virial coefficients in 3D are not divergent. See Sec. 4.2.2 for an example that Borel method shows better performance. We also observed that it is more difficult to find solvable coefficients in the case of Borel-Padé method. Up to the fifth order expansion, we found only one order at which the Padé approximant exists, as shown in the plot.
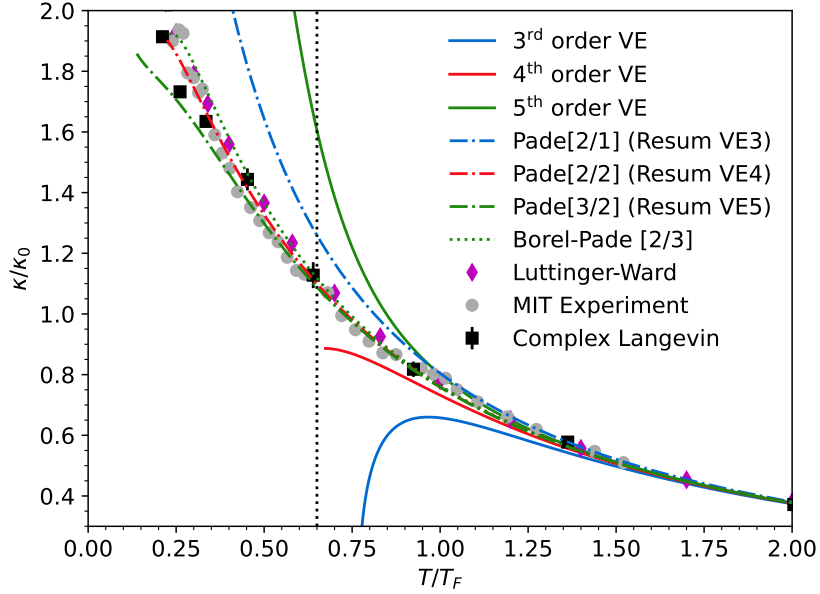
Figure 3.15: Compressibility κ of the unitary Fermi gas in units of its noninteracting, ground-state counterpart κ_0, as a function of the temperature T in units of the Fermi temperature T_F. Our results for the virial expansion for fugacity $z \in [0, 1]$ are shown as solid lines: blue for third order, red for fourth order, and green for fifth order. The dash-dotted lines are the result of Padé resummation, whose color follows the same convention and the order is diagonal or off-diagonal. The green dotted line is the result of a [2/3] Borel-Padé resummation, which is the only solvable case. Other resummation orders are omitted due to the appearance of poles on the real axis in the region of interest. The vertical dotted line corresponds to the approximate T/T_F where $z = 1$ for the three resummed results. The red circles show the data from the MIT experiment of Ref. [61]. The purple diamonds are the Luttinger-Ward calculations of Ref. [140]. The black squares are complex-Langevin results from Ref. [138].

3.4.5: Magnetic susceptibility and the pseudogap phase

Based on Eq. (3.33), the interaction-induced change in spin-susceptibility is expressed in terms of expansion as

$$\Delta\chi = \frac{\lambda_T^2}{8\pi} Q_1 \sum_{n=3}^{\infty} \sum_{m+j=n} (m-j)^2 \Delta b_{mj} z_\uparrow^m z_\downarrow^j, \tag{3.37}$$

where we omit the subscript in χ_s for simplicity. To apply the Padé resummation, we use the same scheme of rewriting the series in terms of $z = \exp(\beta\mu)$ and $\exp(\beta h)$[6].

In Fig. 3.16, we plot for the UFG the spin-susceptibility in its dimensionless form χ/χ_0, scaled by Pauli susceptibility χ_0 which is the noninteracting spin susceptibility at $T = 0$ and defined as

$$\chi_0 = 3n/(2\epsilon_F). \tag{3.38}$$

---

[6]Part of this section is based on the work published on Ref. [105]
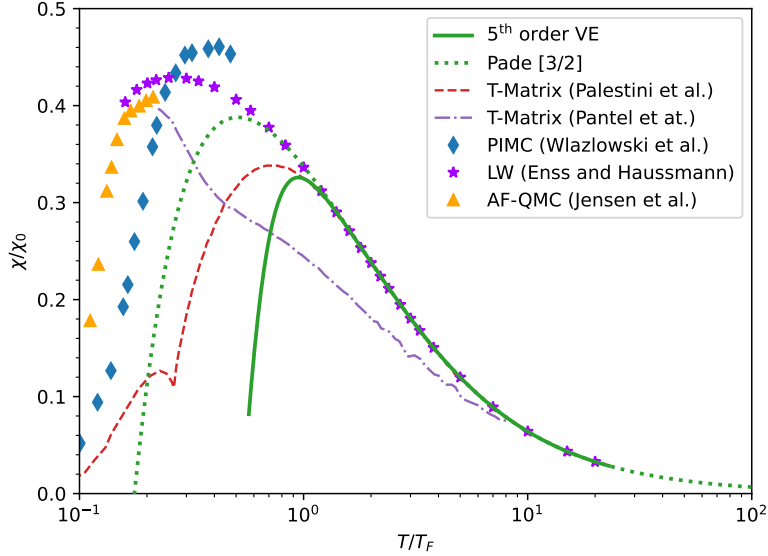
Figure 3.16: Spin susceptibility χ in units of the Pauli susceptibility χ_0 as a function of T/T_{F} for the UFG. The green solid curve is the fifth-order QVE at its face value, and the green dotted line is the Padé resummed results at order [3/2]. For comparison, we plot the t-matrix results from Ref. [141] (red dashed line) and Ref. [142] (purple dash-dotted line), the PIMC results from Ref. [143], the Luttinger-Ward results from Ref. [140], and the Auxiliary-Field QMC (AF-QMC) results from Ref. [144].

where $\epsilon_{\mathrm{F}} = T_{\mathrm{F}} = k_{\mathrm{F}}^2/2$ in the natural unit.

For clarity, we only present the best QVE results, i.e. the fifth-order truncated QVE and the resummed results at [3/2], and compare with a selection of existing results [140–144]. With the help with resummation method, we find agreement with the Luttinger-Ward results [140] up to around $T/T_F \approx 0.6$. Finally, we note that even though both the bare and resummed results displays the suppression of susceptibility at low temperature (the resummed results even shows a similar peak location compared to the PIMC result), such agreement should be taken only as coincidental due to onset of phase transition at such a low temperature. For other works omitted in the plot, see e.g. Refs. [145, 146] for theoretical calculations, and Refs. [147–149] for experimental measurements[7]. See also Ref. [105] for more details on the presented results.

In Fig. 3.17, we compare the QVE results with the CL results (see also Ref. [138]) at different polarizations βh. As βh increases, we find better agreement at lower temperature between the the resummed results and CL calculations. Mathematically, it is the result of the dominant role of

---

[7]Note that the results of Ref. [148] are at odds with all other values, which is presumably the result of trapping averaging.

polaron coefficients Δb_{m1}, which are better-behaved as seen in the subspace sequence. Physically, the increasing polarization effectively approaches to the noninteracting limit, whose information is better captured by fewer-body systems (which favors the resummation method).

As the polarization increases, we also observe from the CL results the emergency of a plateau of χ/χ_0. Even though less obvious, the QVE results also present a similar trend with a broad maximum. At lower temperature, the plateau turns into a rapid suppression, which could be the result of the onset of superfluid phase, or the pairing formed in the so-called pseudogap regime.

Though the precise definition or indicator of the pseudogap regime is still under debate [145, 150], a commonly accepted one is the gap between pairing temperature and the condensation temperature, as indicated in Fig. 1.1. Therefore, if the suppression is indeed from the pairing in the pseudogap regime[8], we expect a gap between the pairing temperature and the critical temperature of the superfluid phase transition. We defined the pairing temperature fuzzily as the region around the maximum location of χ/χ_0. Thanks to the analytic nature of our QVE results, we are able to define a smooth region without repeating calculations.

We present the Fig. 2 from Ref. [105] in Fig. 3.18. Here we only summarize the results related to the QVE and readers are recommended to Sec. V in Ref. [105] for more discussions. The squares represent the maximum location from the CL results for $\beta h = 0.0, 0.4$ and 0.8, where a sharp peak can be clearly determined. The surrounding lines are uncertainty estimation due to the discrete grid parameters used. For $\beta h > 0.8$, the plateau is more obvious and only the estimated region (the solid line) is given. Similarly, in the QVE results, the plateau emerges in the form of a broad peak region. We plot the shaded gray region using the conservative 99.7% of the maximum value. The selection of this value is purely artificial and has no statistical connection to the 3σ region. The gray dotted line indicates the regime where the resummation results are expected to fail at lower temperature.

In both panels, we see the overlap of the solid lines and the onset of superfluid phase. For the QVE results, the gap between the pairing temperature and superfluid phase is because of the conservative parameter (99.7% of the maximum value) used to define the broad shaded region.

Therefore, for $\beta h \geq 1.2$, the narrow room between the pairing temperature determined from

---

[8]another mechanism for the susceptibility suppression is the transition into superfluid phase
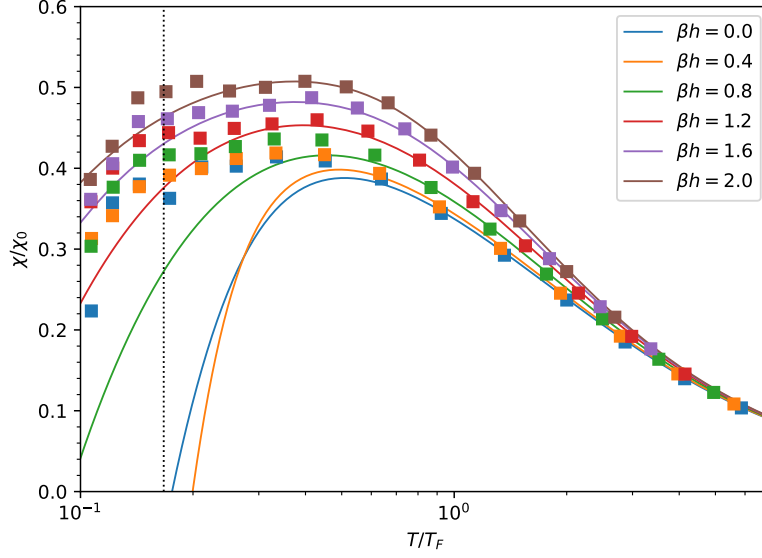
Figure 3.17: Spin susceptibility χ in units of the Pauli susceptibility χ_0 as a function of T/T_F for the spin-imbalanced Fermi gas with different polarization $\beta h = 0, 0.4, 0.8, 1.2, 1.6$ and 2.0. The vertical dotted line represents the critical temperature for the superfluid phase at $T/T_F \approx 0.167$ [61]. The colorful solid curves are the Padé-resummed fifth-order QVE at order $[3/2]$ and colorful squares are the CL results.

the susceptibility and the condensation temperature indicates the absence of the pseudogap regime.

If it even exists, we may only expect it develops at lower polarization in the regime $\beta h < 1.2$.
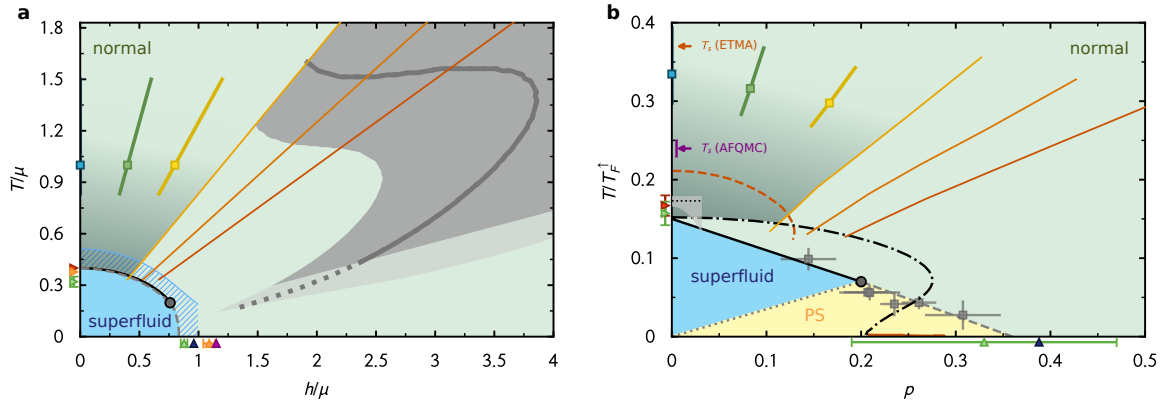
Figure 3.18: [Excerpt from Fig. 2 of Ref. [105], Reprinted with permissions. Copyright (2022) by the American Physical Society] Phase diagrams of the spin-polarized UFG. (a) Phase diagram spanned by the dimensionless temperature $(\beta\mu)^{-1}$ and the dimensionless Zeeman field h/μ. The black solid line depicts the second-order phase transition line from a fRG study [151] where the black dot represents the location of the critical point. The thick line reflects the spin-gap temperature T_s as obtained from the PRVE along with an uncertainty estimate (shaded area). (b) Phase diagram spanned by $T/T_{F,\uparrow}$ and the polarization as measured in experiment [152] (gray squares reflect experimental measurements, thick lines are the inferred phase boundaries) and compared to recent determinations via LW theory [153, 154] (dot-dashed line) as well as ETMA [146] (red dashed line). For the balanced limit T_s is shown as determined via AFQMC [145] and ETMA [146]. In both panels, squares reflect the maximum of the CL data and thick lines indicate the uncertainty estimate (see main text). The thin colored lines reflect the the observed plateau in the spin-susceptibility ($\beta h = 1.2, 1.6, 2.0$ from left to right, respectively). Critical values correspond to experimental values from the MIT group [61] (red triangles) and ENS group [62, 155] (green triangles), LW results [154] (orange triangle), FN-DMC calculations [156] (dark blue triangles), ϵ-expansion (purple triangle) and Worm-MC data [157] (light gray-shaded area). The black shaded areas in both panels mark potential pseudogap regions.

CHAPTER 4:   Homogeneous Fermi Gas: crossover in different dimensions

In this chapter, we move away from the UFG and investigate the spin-1/2 Fermi gas with different coupling strength and in different dimension. We begin with a short section on Δb_n up to $n = 7$ with semiclassical approximations. In particular, we study its behaviour as a function of dimension d. Then we take the large-N_τ limit and investigate the system in integer dimensions[1].

Section 4.1:   Semiclassical Δb_n up to seventh order and dimensional crossover

In last chapter when we studied the UFG, we presented only the results using virial coefficients extrapolated to $N_\tau \to \infty$ limit. However, despite of the lack of quantitative accuracy, the semi-classical approximation remains an essential tool which shreds light on the physics insights with reasonable computational costs, especially useful for higher-order coefficients. Moreover, with a small N_τ, we can write down the analytic formulas for Δb_n explicitly, making it much easier to manipulate parameters such as the dimension c. The last benefit of the semiclassical approximation is that we could express Δb_n in terms of Δb_2.[2] In other words, such analytic expressions qualitatively demonstrate the effect of two-body system on n-body systems.

In Ref. [90], with semiclassical approximation, i.e. at $N_\tau = 1$, Δb_n are expressed in terms of Δb_2 for $n = 3$ and 4 as

$$\Delta b_3 = -2^{1-\frac{d}{2}}\Delta b_2, \tag{4.1}$$

$$\Delta b_4 = 2(3^{-\frac{d}{2}}+2^{-d-1})\Delta b_2 + 2^{1-\frac{d}{2}}(2^{-\frac{d}{2}-1}-1)(\Delta b_2)^2, \tag{4.2}$$

where we also fix a typo in the coefficient of $(\Delta b_2)^2$ term of Δb_4 from the published version in Ref. [90].

We extended the calculation up to $n = 7$ at leading order (LO) and obtained the following

---

[1]This chapter is based on works published in Ref. [158, 159]

[2]For $N_\tau = 1$, it is straightforward to do so as Δb_2 is proportional to the bare coupling C. For $N_\tau = 2$, this relation becomes quadratic. Despite of more complicated formulas, it is still plausible to invert the relation into $C(\Delta b_2)$.

formulas

$$\Delta b_3 = -\, 2^{1-d/2}\Delta b_2, \tag{4.3}$$

$$\Delta b_4 = \left[2(3^{-d/2} + 2^{-d-1})\right]\Delta b_2 + \left[2^{1-d/2}(2^{-d/2-1} - 1)\right](\Delta b_2)^2, \tag{4.4}$$

$$\Delta b_5 = \left[-2(2^{-d} + 6^{-d/2})\right]\Delta b_2 + \left[4\left(2^{-d} + 3^{-d/2} - 7^{-d/2}\right)\right](\Delta b_2)^2, \tag{4.5}$$

$$\Delta b_6 = \left[2^{1-3d/2} + 3^{-d} + 2\cdot 5^{-d/2}\right]\Delta b_2$$
$$+ \left[-2^{1-3d/2} - 3\cdot 2^{1-d}(1 - 3^{-d/2}) - 2^{2-d/2}(3^{1-d/2} - 5^{-d/2})\right](\Delta b_2)^2$$
$$+ \left[2^{2-d} - 8\cdot 7^{-d/2} + 8\cdot 3^{-d/2-1}(1 + 2^{-d})\right](\Delta b_3)^3, \tag{4.6}$$

$$\Delta b_7 = \left[-2^{1-d/2}\left(6^{-d/2} + 5^{-d/2} + 3^{-d/2}\right)\right]\Delta b_2$$
$$+ \left[2^{4-3d/2} + 8\cdot 5^{-d/2} + 8\cdot 3^{-d/2}(3^{-d/2} + 2^{-d}) - 4(2^{-d}5^{-d/2}\right.$$
$$\left. -13^{-d/2} - 3\cdot 17^{-d/2})\right](\Delta b_2)^2$$
$$+ \left[-2^{3-3d/2} - 2^{3-d}(1 - 3^{1-d/2}) - 8\cdot 2^{-d/2}(3^{1-d/2} - 7^{-d/2})\right.$$
$$\left. -16\cdot 10^{-d/2}(2^{-d/2} - 1)\right](\Delta b_2)^3. \tag{4.7}$$

We also obtained the next-to-leading order (NLO) results, i.e. at $N_\tau = 2$, and express them in terms of the dimensionless coupling $\widetilde{C} = C/\lambda_T^d = (e^{\beta g_d/2} - 1)\ell^d/\lambda_T^d$. For clarity, we show here only the results up to the fifth order to avoid the cluttering.

$$\Delta b_2 = \widetilde{C} + 2^{\frac{d}{2}-1}\widetilde{C}^2, \tag{4.8}$$

$$\Delta b_3 = -\, 2^{1-\frac{d}{2}}\widetilde{C} + \left(1 - \frac{2^{1+d}}{5^{\frac{d}{2}}}\right)\widetilde{C}^2, \tag{4.9}$$

$$\Delta b_4 = 2(3^{-\frac{d}{2}} + 2^{-d-1})\widetilde{C} + \left(3^{1-\frac{d}{2}} + 2^{-d-1} - \frac{3}{2^{\frac{d}{2}}}\right)\widetilde{C}^2$$
$$+ \left(1 + 2^{1-\frac{d}{2}} - \frac{2^{d+2}}{5^{\frac{d}{2}}}\right)\widetilde{C}^3 + \left(\frac{3}{4} - \frac{2^d}{3^{\frac{d}{2}}}\right)\widetilde{C}^4, \tag{4.10}$$

$$\Delta b_5 = -\left(2^{1-d} + \frac{2^{1-\frac{d}{2}}}{3^{\frac{d}{2}}}\right)\widetilde{C}$$
$$+ \left(\frac{7}{2^d} - \frac{2^{1+d}}{3^{\frac{3d}{2}}} + \frac{7}{3^{\frac{d}{2}}} - \frac{2}{7^{\frac{d}{2}}} - \frac{2^{1+d}}{11^{\frac{d}{2}}} - 3\cdot\frac{2^{1+d}}{19^{\frac{d}{2}}}\right)\widetilde{C}^2$$
$$+ \left[2^{1-d} - 2^{1-\frac{d}{2}} + 4\cdot 3^{1-\frac{d}{2}} - 2^{\frac{d}{2}+2}\left(\frac{2}{3^d} + 5^{-\frac{d}{2}} - 7^{-\frac{d}{2}}\right)\right]\widetilde{C}^3$$

84

$$+\left(1 + 2^{2-\frac{d}{2}} - 2^{1+d}\, 3^{1-d} - 3 \cdot \frac{2^{1+d}}{5^{\frac{d}{2}}} - \frac{4^d}{3^d\, 5^{\frac{d}{2}}} + \frac{3^{1-\frac{d}{2}} 4^d}{7^{\frac{d}{2}}} + 3 \cdot \frac{2^{1+2d}}{29^{\frac{d}{2}}}\right) \widetilde{C}^4. \tag{4.11}$$

The above formulas can also be expressed in powers of Δb_2 $((\Delta b^2)^{1/2}$ to be specific) by inverting Eq. (4.8):

$$\tilde{C} = 2^{-\frac{d}{2}}\left(\sqrt{1 + 2^{\frac{d}{2}+1}\Delta b_2} - 1\right). \tag{4.12}$$

which is the solution yielding the positive $\tilde{C}$ corresponding to the positive Δb_2 for the attractive Fermi gas.

Based on the analytic structure, we note that just as in the $N_\tau = 1$ case, in the $N_\tau = 2$ case Δb_2 is always positive and Δb_3 is always negative, for positive $\tilde{C}$ in $d = 1, 2, 3$. The behavior of Δb_4 and Δb_5, however, is less obvious as (partly) a result from the competing subspace contributions.

In Fig. 4.1, we plot the coefficients as a function of dimension and study the behavior of Δb_n in the dimension crossover. The left panel corresponds to stronger coupling where we renormalized the bare coupling to $\Delta b_2 = 1/\sqrt{2}$, i.e. the system becomes the UFG in 3D. The right panel shows the case in weaker coupling where the bare coupling is renormalized to $\Delta b_2 = 1/(5\sqrt{2})$. Experimentally, the dimension crossover can be realized by imposing anisotropic trapping potential. In the left panel, we also compare with the results in integer dimensions by Refs. [21, 41, 46, 90]. In 1D and 2D, we interpolated their results to the same physical coupling strength to match our choice of Δb_2. For Δb_3, we found that the NLO results accurately capture the crossover behavior. The LO results deviates from the existing results but shows qualitatively correct trend. In the case of Δb_4, as we explained in Sec. 3.2.2, the LO result is closer to the existing estimation at unitarity (3D), but both LO and NLO results show similar trend in the dimension crossover. Furthermore, the difference between the LO and NLO results grows larger as the coupling strength become stronger and the particle number increases. In particular, the dependence on particle number implies larger $N_{\tau,\mathrm{max}}$ needed to achieve a similar accuracy, one of the major technical difficulties for the calculation of higher-order coefficients.
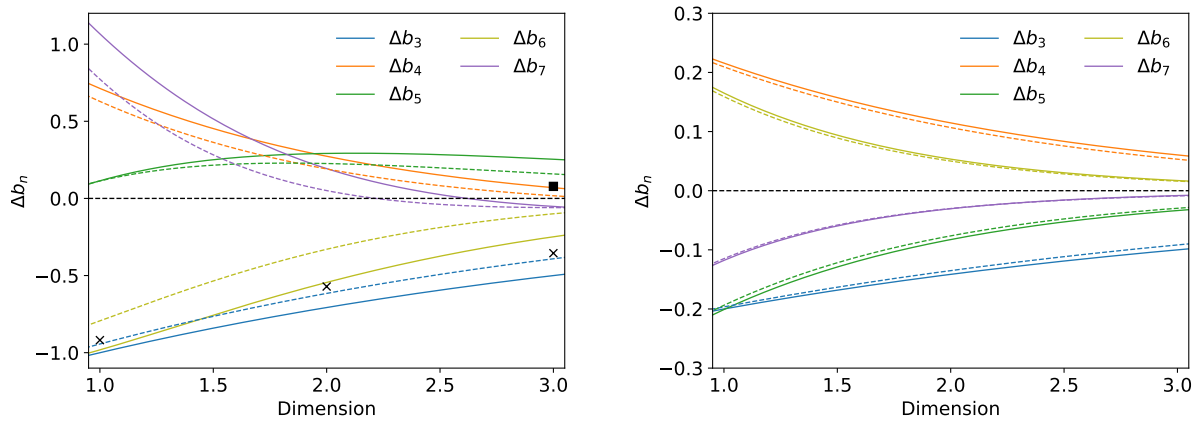
Figure 4.1: Interaction-induced change in virial coefficients $\Delta b_3 - \Delta b_7$ as a function of the spatial dimension d, at LO and NLO (solid and dashed lines, respectively). The left panel shows the results at unitarity, i.e. with $\widetilde{C}$ renormalized to $\Delta b_2^{\mathrm{UFG}} = 1/\sqrt{2}$ and the right panel shows the weak coupling case with $\Delta b_2 = 1/(5\sqrt{2})$. In the left panel, the crosses represent Δb_3 as follows: Monte Carlo results in 1D from Ref. [90], diagrammatic results in 2D from Ref. [46], and exact results in 3D [41]. The square shows the Δb_4 result of Ref. [21].

Section 4.2: Systems in different dimensions

In this section we move to the integer dimensions. Similar to the last chapter, in each spatial dimension, we present our estimations of Δb_n up to $n = 5$ after extrapolating to the $N_\tau \to \infty$ limit, and demonstrate applications centered around quantities such as the density equation of state, Tan contact, and the isothermal compressibility. The exception is the 3D case, where only the coefficients are presented as we have examined its application comprehensively in the last chapter. Furthermore, we focus largely on unpolarized systems (the exceptions being the density equation of state in 1D), but also provide the subspace decomposition of Δb_4 and Δb_5, which extend the applicability of the polarized system as shown in Sec. 3.4.

4.2.1: 1D System

Virial coefficients in 1D

The Beth-Uhlenbeck formula takes the form as Eq. (1.34) [26, 27]

$$\Delta b_2^{1\mathrm{D}} = -\frac{1}{2\sqrt{2}} + \frac{e^{\lambda_1^2/4}}{2\sqrt{2}}[1 + \mathrm{erf}(\lambda_1/2)]. \tag{4.13}$$

where the physical coupling $\lambda_1 = 2\sqrt{\beta}/a_0$ with the 1D scattering length a_0.

In Fig. 4.2, we show the scaled virial coefficients as a function of λ_1 for both whole- and sub-

Figure 4.2: **Top**: Virial coefficients Δb_n for $n = 3 - 5$ for the 1D attractive Fermi gas as a function of the dimensionless coupling λ_1. To fit the scale, the Δb_ns are scaled by $\exp(-q\beta\epsilon_b)$, where q is the maximum number of spin-↑↓ pairs. The $k = 2$ results are shown as dashed lines, $k = 3$ as dashed-dotted lines, and the $k \to \infty$ extrapolation with solid lines. Results for Δb_3 appear in blue, Δb_4 in red, and Δb_5 in green (as labeled). Blue squares and red stars show the QMC results for Δb_3 and Δb_4, respectively, from Ref. [90]. **Bottom**: Subspace contributions Δb_{mj} as functions of the coupling strength, scaled by $\exp(-j\beta\epsilon_b)$. Our results are shown as labeled error bands, color-coded as in the top plot by $n = m + j$: blue for $-\Delta b_{21}$, red for Δb_{31} and Δb_{22}, and green for $-\Delta b_{41}$ and $-\Delta b_{32}$. Specific cases are inverted in sign for clarity and to avoid overlaps.

space. Unlike the 3D case where the two-body bound state threshold is the unitarity, in 1D and 2D, the two-body bound state forms as soon as the interaction is turned on. The virial coefficients will tend to grow exponentially with the binding energy, as is evident at second order from the Beth-Uhlenbeck formula. To capture that behavior, we scaled our virial coefficients by the inverse Boltzmann weight $\exp(-q\beta\epsilon_B)$ of the available particle pairs $q = \lfloor n/2 \rfloor$ (i.e. $q = 1$ for Δb_3 and $q = 2$ for Δb_4 and Δb_5), where $\epsilon_B = 1/a_0^2$ is the binding energy of the two-body system.

In the top panel of Fig. 4.2, we show the whole-space results Δb_n and find excellent agreements with the QMC data of Ref. [90] for Δb_3 and Δb_4. For the latter, the QMC calculations are very limited and stop beyond at $\lambda_1 \simeq 1.0$ (where the QMC method begins to break down), whereas our present results go well beyond that region.

The resulting mild behavior at strong coupling shows that indeed the scaling factor captures the shape of Δb_n as the coupling grows stronger. Beyond that leading contribution, however, Δb_3 is controlled by the atom-dimer scattering properties, just as Δb_4 is controlled by dimer-dimer properties, and so on.

Same as the 3D case, we find that Δb_3 is of constant sign, whereas Δb_4 and Δb_5 change sign at strong enough coupling, as a result of the competition between positive and negative contributions coming from the subspaces Δb_{mj}. In terms of magnitudes, we observed that $|\Delta b_5| \approx |\Delta b_4|$ for all coupling strengths examined.

The Δb_{mj} are shown in the bottom panel of Fig. 4.2. The alternating sign as observed in the 3D case holds true for both Δb_{m1} and Δb_{m2} subspace sequences, though all curves are no longer monotonic in 1D. The sequence $|\Delta b_{m1}|$ follows essentially the same trend as a function of the coupling for all m, and magnitudes are increasingly suppressed for increasing m, i.e. following the "normal ordering". The suppression is similar to that in the 3D case: at large m both $|\Delta b_{m1}|$ and $|\Delta b_{m2}|$ must approach the noninteracting values (i.e. zero) as the majority of the particles do not interact due to Pauli blocking. In the case of Δb_{m2}, the inverted ordering, i.e. $|\Delta b_{32}| > |\Delta b_{22}|$, holds for wider range until the crossing point at $\lambda_1 \approx 4$, which is presumably the result of enhanced interaction effects in the low dimension[3].

Applications in 1D

Density equation of state at finite polarization - In Fig. 4.3 we show our estimates for the density equation of state for attractively interacting fermions at finite polarization in 1D using QVE (see Sec. 3.4.1 for the formalism), . We compare our results with those of Ref. [160] obtained with the complex Langevin method. The fifth-order virial expansion provides a modest improvement over the third and fourth orders. However, for all the available polarizations the agreement with the data is reasonable as long as $\beta\mu$ is sufficiently small. The resummed results (dotted lines) uses Padé approximant at order [2/3] and it extends the agreement to larger $\beta\mu \approx -1$. Recall that in the 3D case where we find agreements up to $\beta\mu = 0.7$. Such difference is a manifestation of the enhanced interaction effects in the low-dimensional systems. This example shows

---

[3]However, due to different definition of physical coupling λ in different dimensions (differed by a constant factor), it is not straightforward to make a direct comparison. Therefore we only make a qualitative argument here.
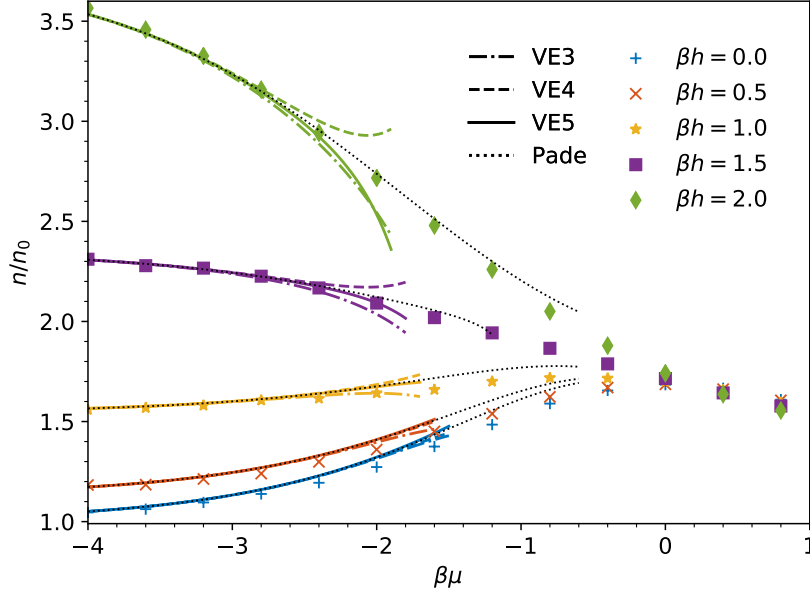
Figure 4.3: Density equation of state n of the attractive 1D Fermi gas, shown in units of the noninteracting, unpolarized counterpart n_0 with coupling strength $\lambda_1 = 1.0$, for several values of the chemical potential difference $\beta h = \beta(\mu_\uparrow - \mu_\downarrow)/2$. The colored symbols are complex-Langevin results from Ref. [160] and the colored lines show the virial expansion at various orders: dashed-dotted line at third order (VE3), dashed line at fourth order (VE4), and solid line at fifth order (VE5). The black dotted line is the result of the [3/2] Padé resummation. The Padé approximant for $\beta h = 1.5$ contains a pole close to $\beta\mu = -1.2$; the corresponding dotted line is therefore cut off at that value. The limiting value for $\beta\mu \to -\infty$ is known exactly and is given by $\cosh(\beta h)$.

one of the major limitations of the resummation technique: it is deterministic and depends only on the series coefficients. In other words, we have to accept the results as they are: there is no systematic way to improve the region of convergence, nor a way to determine the correctness *a priori*.

Contact - In 1D, the contact is given by [118]

$$\mathcal{I} = \frac{2}{\beta} \frac{\partial(\beta\Omega)}{\partial a_0}, \tag{4.14}$$

such that its virial expansion becomes

$$\mathcal{I} = \frac{4\pi}{\lambda_T^3} Q_1 \sum_{m=2}^{\infty} c_m z^m, \tag{4.15}$$

89
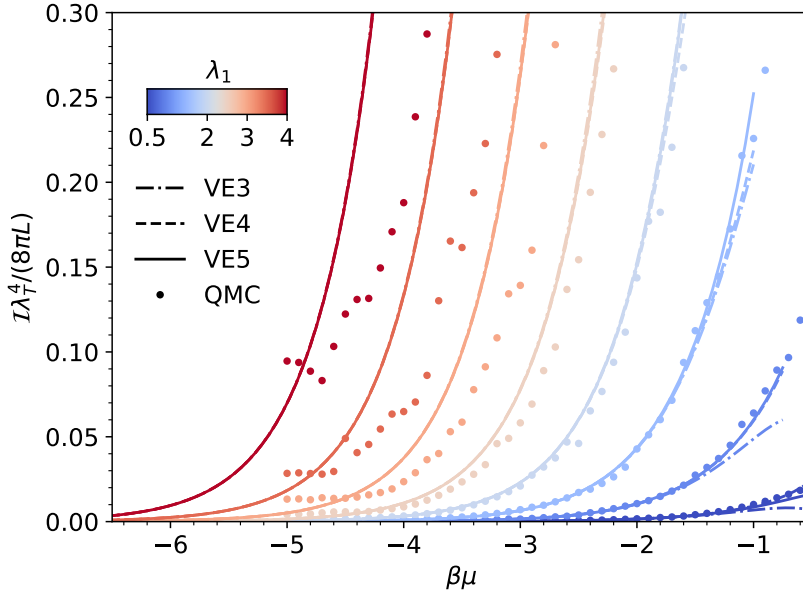
Figure 4.4: Tan contact $\mathcal{I}$, in the dimensionless form $\mathcal{I}\pi\beta^2/(2L\lambda_1^2)$, as a function of $\beta\mu$, for the attractive 1D Fermi gas. The dots show the QMC results of Ref.[26] and the curves show the virial expansion at various orders, following the same line style as in Fig. 4.3. The color encodes the coupling strength of from $\lambda_1 = 0.5$ (dark blue) to $\lambda_1 = 4.0$ (dark red) in steps of 0.5. From bottom to top, the curves and data correspond to $\lambda_1 = 0.5, 1.0, 1.5, 2.0, 2.5, 3.0, 3.5,$ and 4.0.

and

$$c_m = \sqrt{\frac{\pi}{2}}\lambda_1^2 \frac{\partial \Delta b_m}{\partial \lambda_1}. \tag{4.16}$$

The Beth-Uhlenbeck formula in Eq. (4.13) yields

$$c_2 = \frac{\lambda_1^2}{4} + \frac{\sqrt{\pi}}{8}e^{\lambda_1^2/4}\lambda_1^3[1 + \mathrm{erf}(\lambda_1/2)], \tag{4.17}$$

as first shown in Ref. [26]. Using the λ_1 dependence of our results for Δb_n, we obtained the virial expansion of $\mathcal{I}$ up to fifth order.

In Fig. 4.4 we show the dimensionless, intensive form of the contact, $\mathcal{I}\pi\beta^2/(2L\lambda_1^2)$ as a function of temperature in the virial expansion. At weak couplings ($\lambda_1 \leq 2.0$), the virial expansion shows good agreement with the QMC results of Ref.[26]. However, as the coupling strength increases, the disparity becomes significant, which is not completely unexpected as both methods face challenges in the strong coupling regime: the radius of convergence of the QVE can be very
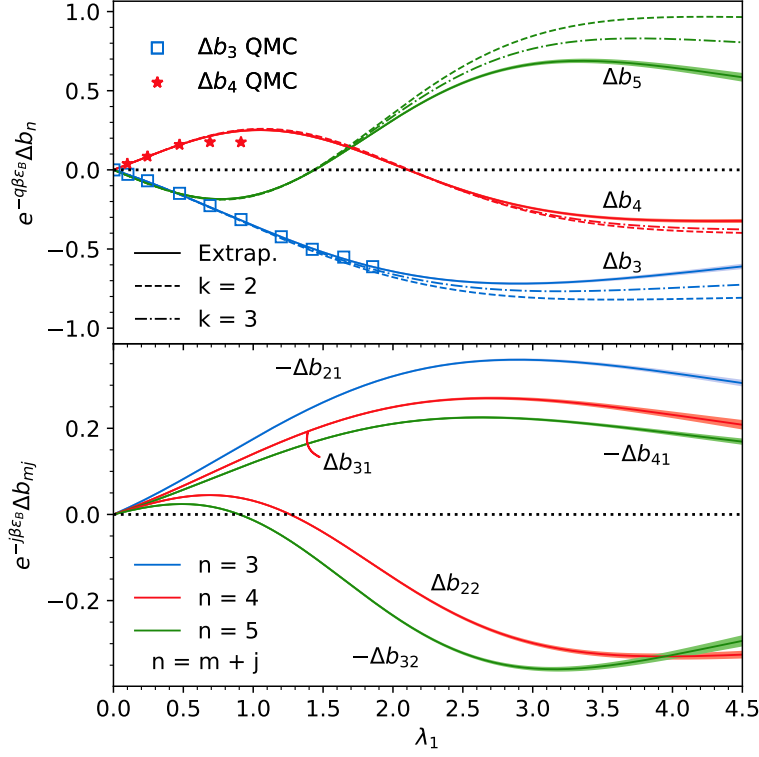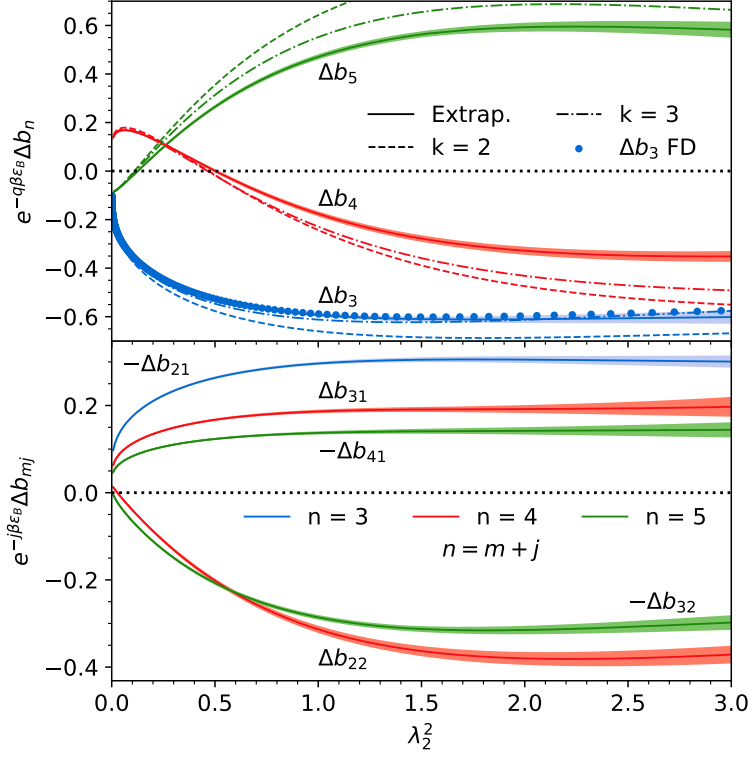
Figure 4.5: **Top**: Virial coefficients Δb_n for $n = 3 - 5$ for the 2D attractive Fermi gas, as a function of the square of the dimensionless coupling λ_2. To fit the scale, Δb_ns are scaled by $\exp(-q\beta\epsilon_b)$, where q is the maximum number of spin-↑↓ pairs, and Δb_{mj} are scaled by $\exp(-j\beta\epsilon_b)$. The $N_\tau = 2$ results are shown as dashed lines, $N_\tau = 3$ as dashed-dotted lines and the $N_\tau \to \infty$ extrapolation with solid lines. Results for Δb_3 appear in blue, for Δb_4 in red, and for Δb_5 in green (as labeled). The diagrammatic result for Δb_3 from Ref. [30] appear as blue dots. **Bottom**: Subspace contributions Δb_{mj} as functions of the coupling strength. Our results are shown as labeled error bands, color-coded as in the top plot by $n = m + j$: blue for $-\Delta b_{21}$, red for Δb_{31} and Δb_{22}, and green for $-\Delta b_{41}$ and $-\Delta b_{32}$.

small, such that the expansion ceases to be useful even at very negative $\beta\mu$; on the other hand, the lattice QMC method may suffer from increasing lattice-spacing effects at strong coupling, due to the reduced size of the two-body bound state. We also noted that as coupling increases, the differences between QVE results at different order become negligible, resulting from the dominant role of two-body bound state.
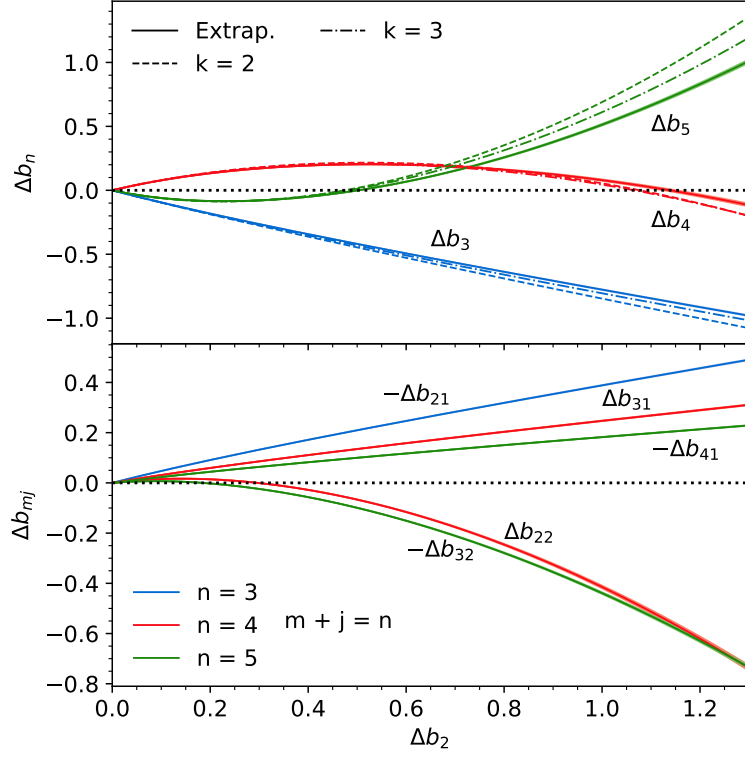
Figure 4.6: Weak-coupling zoom-in on Fig. 4.5, not including the $\exp(-q\beta\epsilon_B)$ factor and plotted as a function of Δb_2. The right edge of the horizontal axis corresponds to $\lambda_2 \simeq 0.588$. The line type, color, and labeling is the same as that of Fig. 4.2.

4.2.2: 2D System

Virial coefficients in 2D

The 2D Beth-Uhlenbeck result is shown in Eq. (1.69)

$$\Delta b_2^{2D} = e^{\lambda_2^2} - \int_0^\infty \frac{dy}{y} \frac{2e^{-\lambda_2^2 y^2}}{\pi^2 + 4\ln^2 y}, \qquad (4.18)$$

where the physical coupling $\lambda_2^2 = \beta\epsilon_B$, and ϵ_B is the binding energy of the two-body system.

In Fig. 4.5 we show our results for Δb_n as a function of λ_2^2 for the 2D attractive Fermi gas (see e.g. the review Ref. [161]). As in 1D, we scaled the coefficients by $\exp(-q\beta\epsilon_B)$, where $q = \lfloor n/2 \rfloor$ is the maximum number of available spin-↑↓ pairs.

In the top panel, we find similar behaviors of the whole-space coefficients, just as in 1D and 3D: Δb_3 remains negative for all the couplings studied; Δb_4 and Δb_5 change sign at strong enough

coupling and their magnitudes are similar save that $|\Delta b_5|$ is slightly larger, the same as the case in 1D and 3D. For reference, we plot the diagrammatic results of Δb_3 by Ref. [30] as blue dots, and find agreement across the coupling strength studied.

The subspace contributions Δb_{mj} are shown in the bottom panel of Fig. 4.5 and parallel the behaviors in the other two dimensions. Furthermore, $|\Delta b_{m1}|$ and $|\Delta b_{m2}|$ follow consistent trends as a function of the coupling across all m (with the expected suppression as m is increased). In fact, once the $\exp(-q\beta\epsilon_B)$ factor is included, $|\Delta b_{m1}|$ and $|\Delta b_{m2}|$ are approximately constant as the coupling is increased, hinting the dominant role of the two-body bound state. Also, compared to the 1D case, the Δb_{m2} sequence is closer to the 3D case, where the crossing point between the "inverted ordering" and "normal ordering" occurs early at weak coupling, and both curves show (nearly) monotonic trends.

Finally, as the details at weak coupling are elusive in the scale of Fig. 4.5, we zoom in the weakly coupling regime and plot in Fig. 4.6 the raw values of Δb_n as functions of Δb_2, whose range corresponds roughly to $\lambda_2^2 \in [0, 0.6]$. All the coefficients tend smoothly to zero as the coupling is weakened. The non-perturbative behavior at weak coupling is completely captured by Δb_2.

Applications in 2D

Density equation of state at zero polarization - We firstly investigated the density equation of state in absence of polarization and compare our results with several theoretical and experimental works.

In Fig. 4.7, we plot the dimensionless density n/n_0 as a function of $\beta\mu$ at different coupling strength, which is represented by the bound-state energy $\beta\epsilon_B$. For reference, we compare our estimations with the QMC results of Ref. [162] and the Luttinger-Ward results of Ref. [163]. The agreement with the QMC data is outstanding. With the exception of the weakest coupling $\beta\epsilon_B = 0.1$, where the QMC results likely incur volume effects due to the large size of the two-body bound state (although small, this discrepancy remains unresolved), the virial expansion is systematically closer to the QMC data than to the Luttinger-Ward results. At weak coupling, especially at $\beta\epsilon_B = 0.5$ (green), we observed significant improvements from the Padé resummation method, whose results agree with QMC calculation even at large $\beta\mu \approx 2$. Moreover, for all the couplings
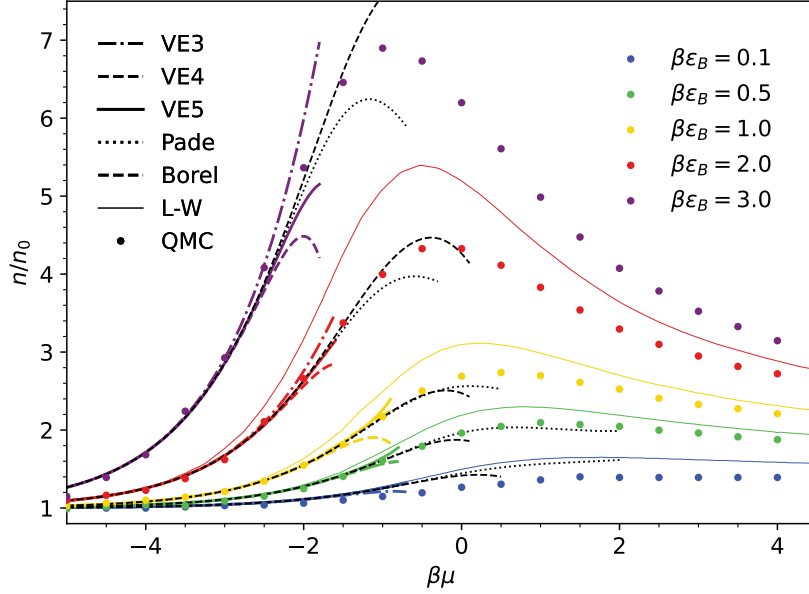
Figure 4.7: Density equation of state n, shown in units of the noninteracting counterpart n_0 at different coupling strength $\lambda_2^2 = \beta\epsilon_B$ in 2D. The colored dots are the QMC results from Ref. [162], the colored thin line shows the Luttinger-Ward result of Ref. [163], and the colored thick lines are virial expansions at different orders (same line style as in previous Fig. 4.3). The black dotted lines and dashed lines are the results, respectively, of Padé and Borel resummation of order $[3/2]$ using the virial coefficients up to the fifth order.

considered, the Padé and Borel resummations substantially extend the region of agreement to approximately $\beta\mu \approx 0$. But as the coupling is increased, the Borel-resummed results outperformed the Padé-resummed ones, showing better agreements with the QMC calculations, while both resummation methods yields qualitative correct trend. Such difference is because of the exponential contribution from the bound-state to the virial coefficients. Therefore, the factorial damping factor used in the Borel method makes it more suitable in this case.

In Figs. 4.8 and 4.9, we compare our results with the experimental data of Refs. [164] and [165], respectively. In all cases, the agreement is remarkable in the regions where the virial expansion is expected to work. Naturally, that region is pushed to progressively more negative $\beta\mu$ as the coupling is increased; in other words, the radius of convergence of the virial expansion decreases as the coupling increases. However, it is also clear that, beyond weak and intermediate couplings (roughly up to $\beta\epsilon_B = 3.0$), the benefits of pushing the virial expansion up to fifth order start to diminish, if the virial expansion is taken at face value. We find, on the other hand, that Padé and Borel resummations dramatically enhance the usefulness of the virial coefficients. As shown in Fig. 4.8 (left and center panels in particular), the resummed results agree not only qualitatively
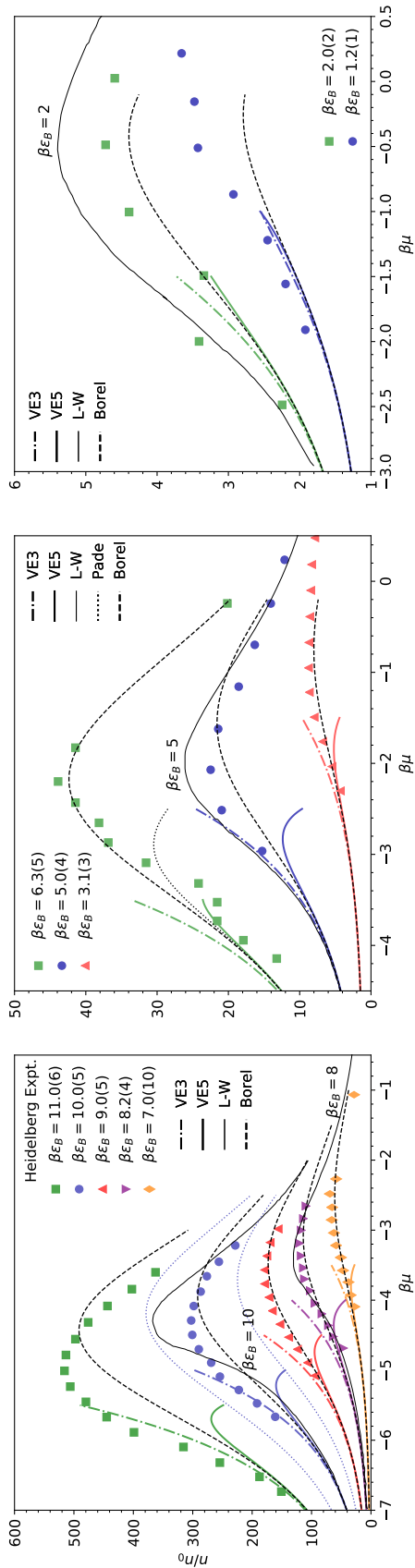
Figure 4.8: Density equation of state n of the 2D attractive Fermi gas, shown in units of the noninteracting counterpart n_0 at different coupling strength $\lambda_2^2 = \beta\epsilon_B$ in 2D. From bottom to top, the curves and data correspond to $\beta\epsilon_B = 0.1, 0.5, 1.0, 2.0,$ and 3.0. The colored symbols are the results of experimental analyses from Ref. [164] and the colored lines show the virial expansion at different orders (following the same line style as in previous figures). [Note: the fourth-order case is omitted from this figure only for the clarity.] The black dashed lines are the results of Borel resummation of order [3/2] using coefficients up to the fifth order. The thin black solid lines are the Luttinger-Ward results of Ref. [163], around which the nearby labels indicate the corresponding $\beta\epsilon_B$. Only the central value of our estimates is used in these plots; the relative-error on the virial coefficients from continuous-time extrapolation can reach 15% at the strongest couplings shown in the left panel, although that does not translate into a significant change in the scale shown. Also in the left panel, the blue dotted lines show our Borel-resummed results at $\beta\epsilon_B = 9.5$ (lower) and 10.5 (upper) respectively, which enclose the experimental points completely (in agreement with the experimental uncertainty on $\beta\epsilon_B$). In the middle panel, we also present the [3/2] Padé result as a black dotted line for $\beta\epsilon_B = 6.3$ to demonstrate the performance difference between the two resummation techniques at strong coupling. Ref. [164] also provides data at $\beta\epsilon_B = 0.45(5)$, but mostly at large $\beta\mu > 0$ and therefore not shown here.
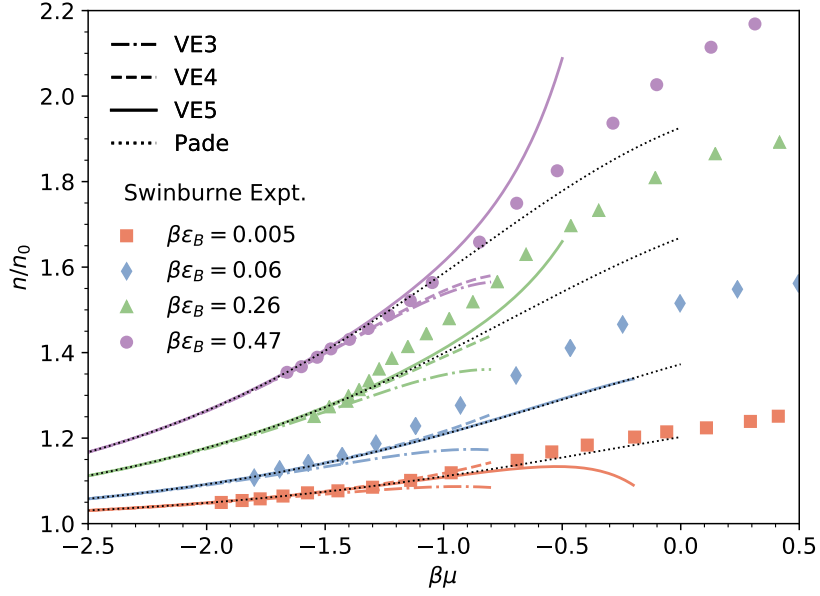
Figure 4.9: Density equation of state n, shown in units of the noninteracting counterpart n_0 at different coupling strength $\lambda_2^2 = \beta\epsilon_B$ in 2D. The colored symbols are the results of experimental analyses from Ref. [165] and the colored lines are virial expansions at different orders (the same line style applied). The black dotted lines and dashed lines are the results, respectively, of Padé and Borel resummation of order [3/2] using coefficients up to the fifth order.

but in several cases also quantitatively with the experimental data.

Contact - In 2D, the contact is [32]

$$\mathcal{I} = \frac{2\pi}{\beta} \frac{\partial(\beta\Omega)}{\partial \ln(a_0/\lambda_T)}, \tag{4.19}$$

such that its virial expansion becomes

$$\mathcal{I} = \frac{(2\pi)^2}{\lambda_T^2} Q_1 \sum_{m=2}^{\infty} c_m z^m, \tag{4.20}$$

where

$$c_m = \lambda_2 \frac{\partial \Delta b_m}{\partial \lambda_2}. \tag{4.21}$$
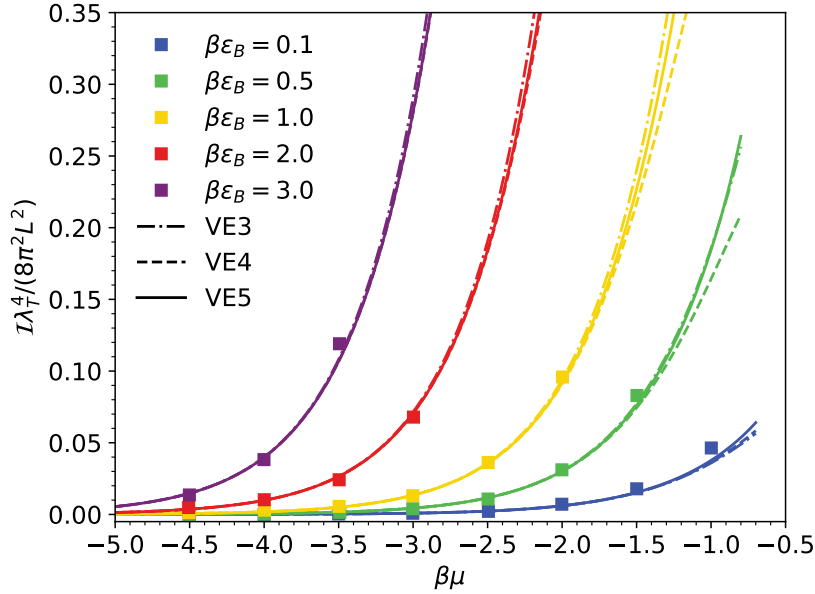
Figure 4.10: Contact $\mathcal{I}$, represented in the dimensionless form $\mathcal{I}\lambda_T^4/(8\pi^2 L^2)$, as a function of $\beta\mu$ in 2D. The squares are the QMC results of Ref. [162] and the lines are the results of virial expansion at various orders (dash-dot for third order, dashed for fourth order, and solid for fifth order). From bottom to top, the data shown corresponds to coupling strengths $\beta\epsilon_B = 0.1$, 0.5, 1.0, 2.0, and 3.0.

The Beth-Uhlenbeck formula yields

$$c_2 = 2\lambda_2^2 e^{\lambda_2^2} \left[1 + 2 \int_0^\infty dy \frac{y e^{-\lambda_2^2(y^2+1)}}{\pi^2 + 4\ln^2 y} \right], \tag{4.22}$$

as shown in Refs. [30, 162]. Using the λ_2 dependence of our results for Δb_n, we obtained the virial expansion of $\mathcal{I}$ up to fifth order.

In Fig. 4.10 we show the dimensionless, intensive form of the contact, $\mathcal{I}\lambda_T^4/(8\pi^2 L^2)$, as a function of $\beta\mu$ in the virial expansion and compared with the QMC results from Ref. [162]. As with the equation of state shown above, the agreement with the QMC data is remarkable in the region where the virial expansion is expected to work well. Moreover, our results extend the discrete QMC calculations to larger region as smooth analytical curves.

4.2.3: 3D System

In Fig. 3.4 and Fig. 3.6, we plot Δb_n and Δb_{mj} respectively as a function of $\Delta b_2/\Delta b_2^{\text{UFG}}$. Here, we present the same coefficients but as a function of the physical coupling strength $\lambda_3 = \sqrt{\beta}/a_0$ in the same fashion as that in 1D and 2D. For the attractive system we studied, λ_3 takes
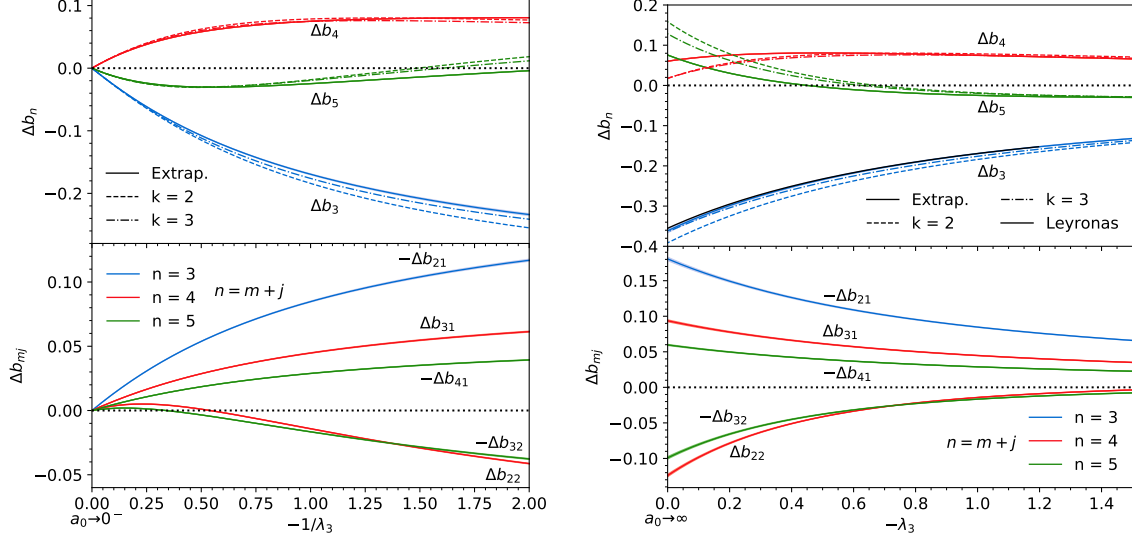
Figure 4.11: **Left:** Δb_n for $n = 3 - 5$ for the 3D Fermi gas in the weak-coupling regime, as a function of the dimensionless coupling λ_3. The $k = 2$ results are shown with dashed lines, $k = 3$ with dashed-dotted lines, and the $k \rightarrow \infty$ extrapolation with solid lines. Results for Δb_3 appear in blue, for Δb_4 in red, and for Δb_5 in green, as labeled, following the same convention as Fig. 4.2. **Right:** Δb_n for $n = 3 - 5$ for the 3D Fermi gas in the vicinity of the unitary regime ($a_0 \rightarrow \infty$, which corresponds to $\lambda_3 = 0$), as a function of the dimensionless coupling λ_3. The exact result for Δb_3 from Ref. [41] appears as a thin solid black line. The $k = 2$ results are shown with dashed lines, $k = 3$ with dashed-dotted lines, and the $k \rightarrow \infty$ extrapolation with solid lines. Results for Δb_3 appear in blue, for Δb_4 in red, and for Δb_5 in green, following the same convention as Fig. 4.2.

a negative value. The limit $-1/\lambda_3 \rightarrow 0$ corresponds to the noninteracting limit $a_0 \rightarrow 0^-$, and the limit $-\lambda_3 \rightarrow 0$ corresponds to the unitary limit $a_0 \rightarrow -\infty$.

In Fig. 4.11, we present our results for Δb_n as a function of λ_3. The left figure shows Δb_n as a function of $-1/\lambda_3$ to display the weak coupling regime, and in the right figure we plot the vicinity around the unitary limit ($\lambda_3 = 0$) as a function of λ_3, where the same results from Ref. [41] is also presented. The bottom panels show the subspace decomposition of Δb_n into Δb_{mj}. The qualitative similarities with lower dimensions are clear. As in 3D there is no two-body bound states formed in the regime we investigated[4], we do not need to scale the coefficients by the factor $\exp(-q\beta\epsilon_B)$.

---

[4]The bound state formed after the unitary limit, see Sec. 1.1.1 for details

CHAPTER 5: Harmonically trapped Fermi gas

In the last two chapters, we discussed the homogeneous Fermi gases under different settings. In this chapter, we move one step further to put the homogeneous system under an external harmonic trap, which is a common setup in ultracold experiments. From a theoretical standpoint, The external trap is also a common setup not only because it matches the experimental configuration but also as the trap behaves as a regulator and actually makes the calculation easier.

In this chapter, we generalize the AA method to deal with the harmonic trapped system, to which end we need to evaluate the trace in the coordinate space. We will show that, unlike the case for conventional methods, this extra term actually makes our calculation more expensive. We present the virial coefficients as a function of trapping frequency and demonstrate with an example to calculate physical observables with QVE.

Section 5.1: Non-interacting trapped Fermi gas and the homogeneous limit

The Hamiltonian for the trapped Fermi gas is very similar to that for the homogeneous system, except for a non-zero external potential term,

$$\hat{H} = \hat{T} + \hat{V}_{\text{ext}} + \hat{V} \equiv \hat{H}_0 + \hat{V} \tag{5.1}$$

with the same $\hat{T}$ and $\hat{V}$ as shown in Eq. (1.4) and (1.6) respectively. We also denote $\hat{H}_0 \equiv \hat{T} + \hat{V}_{\text{ext}}$ as the noninteracting Hamiltonian. In our work, we consider only the isotropic trap but the formalism and methodology can be generalized to anisotropic trap without much effort. For the isotropic harmonic potential, $\hat{V}_{\text{ext}}$ is

$$\hat{V}_{\text{ext}} = \int d^3r \, \frac{1}{2} m\omega^2 \mathbf{r}^2 \left[\hat{n}_\uparrow(\mathbf{r}) + \hat{n}_\downarrow(\mathbf{r}) \right], \tag{5.2}$$

where ω is the trap frequency and $\mathbf{r}$ is the radial distance.

In the absence of inter-particle interactions, the system becomes a quantum harmonic oscillator, whose Hamiltonian $\hat{H} = \hat{H}_0 = \hat{T} + \hat{V}_{\text{ext}}$ is diagonalizable in the subspace with eigenstate

denoted as $|\mathbf{n}_1\mathbf{n}_2\cdots\mathbf{n}_{M+N}\rangle \equiv |\{\mathbf{n}\}\rangle$, where the bold face $\mathbf{n}_i$ represents the energy level vector in d dimension for the ith particle. In this basis, referred to as the HO basis, we have

$$\hat{H}_0\,|\{\mathbf{n}\}\rangle = \epsilon(\{\mathbf{n}\})\,|\{\mathbf{n}\}\rangle, \tag{5.3}$$

and the total energy is

$$\epsilon(\{\mathbf{n}\}) = \sum_{i=1}^{M+N} \epsilon(\mathbf{n}_i), \tag{5.4}$$

where the single particle energy $\epsilon_{\mathbf{n}_i}$ is

$$\epsilon(\mathbf{n}_i) = \omega \sum_{j=1}^{d}\left([\mathbf{n}]_j + \frac{1}{2}\right). \tag{5.5}$$

Similar as the homogeneous case, we take the Fock trace using the HO basis and obtain $\ln\mathcal{Z}$ as

$$\ln\mathcal{Z} = 2\sum_{\mathbf{n}} \ln\left(1 + z e^{-\beta\omega d/2}\prod_{j=1}^{d} e^{-\beta\omega[\mathbf{n}]_j}\right) \tag{5.6}$$

where the summation over bold face $\mathbf{n}$ is over all dimensions from 0 to ∞. Then expand the logarithm in terms of z,

$$
\begin{aligned}
\ln\mathcal{Z} &= 2\sum_{\mathbf{n}}\sum_{k=1}^{\infty}\left[\frac{(-1)^{k+1}}{k}e^{-\beta\omega dk/2}\prod_{j=1}^{d}e^{-\beta\omega k[\mathbf{n}]_j}\right] \\
&= 2\sum_{k=1}^{\infty}\frac{(-1)^{k+1}}{k}e^{-\beta\omega dk/2}\sum_{\mathbf{n}}\prod_{j=1}^{d}e^{-\beta\omega k[\mathbf{n}]_j} \\
&= 2\sum_{k=1}^{\infty}\frac{(-1)^{k+1}}{k}e^{-\beta\omega dk/2}\left(\sum_{n}e^{-\beta\omega kn}\right)^{d} \\
&= 2\sum_{k=1}^{\infty}\frac{(-1)^{k+1}}{k}\left[\frac{1}{2\sinh(\beta\omega k/2)}\right]^{d}.
\end{aligned}
\tag{5.7}
$$

The last piece is the single-particle function Q_1 as given by

$$Q_1 = 2Q_{10} = 2\sum_{\mathbf{n}} e^{-\beta\epsilon(\mathbf{n})} = 2e^{-\beta\omega d/2}\left(\sum_n e^{-\beta n\omega}\right)^d = 2\left[\frac{1}{2\sinh(\beta\omega/2)}\right]^d \tag{5.8}$$

Substitute the above equations into $\ln\mathcal{Z} = Q_1\sum_{n=1} b_n z^n$ and compare order by order, in the end, we obtain the virial coefficients of noninteracting, harmonically trapped spin-1/2 fermions in d spatial dimensions as

$$b_{n,T}^{(0)}(\beta\omega) = \frac{(-1)^{n+1}}{n}\left[\frac{\sinh(\beta\omega/2)}{\sinh(\beta\omega n/2)}\right]^d. \tag{5.9}$$

In the homogeneous limit $\beta\omega \to 0$, the virial coefficient becomes[1]

$$b_{n,T}^{(0)}(\beta\omega \to 0) = \frac{(-1)^{n+1}}{n^{d+1}}, \tag{5.10}$$

Compared to Eq. (1.47), the trapped noninteracting virial coefficient $\Delta b_{n,T}$ is related to the homogeneous one $b_n^{(0)}$ through

$$b_{n,T}(\beta\omega \to 0) = n^{-d/2}b_n, \tag{5.11}$$

as also shown in e.g. Refs. [24, 54, 166, 167].

One may have noticed that there is no superscript (0) in the above equation. It is because this relation actually holds true for interacting Fermi gas in the unitary limit as well. An intuitive explanation is that, due to the divergence of $(k_F a_s)^{-1}$, the unitary virial coefficients are temperature-independent, just as the case for the noninteracting coefficients. For a more mathematical explanation, see e.g. Ref. [24].

Section 5.2: Interacting trapped system

Compared to the interacting homogeneous system, the interacting trapped Fermi gas shares nearly the same formalism and methods with $\hat{H}_0$ in the place of $\hat{T}$. However, the $\hat{H}_0$ is diagonal in its own HO basis instead of the momentum space, and therefore extra attentions are re-

---

[1]See also Ref. [24] for a alternative derivation of noninteracting coefficients using the Local Density Approximation (LDA).

quired. In this section, we will review one essential concept, the Mehler's kernel, for the interacting trapped system, which allows us to apply the AA method to the trapped case. The only difference is that we are now working in the coordinate space, which further impose several technical challenges. Lastly, although we will only discuss the trapped unitary Fermi gas at unitarity in this chapter, we note that the formalism and method presented are generally applicable.

5.2.1: Mehler's kernel

As mentioned above, we will work in the coordinate space for the trapped Fermi gas. This is because if we project it to the coordinate space, we can write the partition function in a compact fashion using the so-called Mehler's formula [168].[2] Taking the single-particle partition function in 1D for example, the trace in the coordinate space yields,

$$Q_{10} = \sum_x \langle x | e^{-\beta \hat{H}_0} | x \rangle = \sum_x \sum_{n=0}^{\infty} \langle x | n \rangle \, \langle n | e^{-\beta \hat{H}_0} | n \rangle \, \langle n | x \rangle = \sum_{n=0}^{\infty} e^{-\beta \epsilon(n)} |\phi_n(x)|^2, \tag{5.12}$$

where the 1D wavefunction for the oscillator $\phi_n(x)$ is explicitly written as

$$\phi_n(x) = \frac{1}{\sqrt{2^\pi n!}} \left(\frac{\omega}{\pi} \right)^{1/4} e^{-\omega x^2/2} H_n(\sqrt{\omega} x), \tag{5.13}$$

where H_n is Hermite polynomial.

Eq. (5.12) is a special case of the Mehler's formula. Its general form states

$$E(x, y) = \sum_{n=0}^{\infty} \frac{(\alpha/2)^n}{n!} H_n(x) H_n(y) = \frac{1}{\sqrt{1-\alpha^2}} \exp\left(-\frac{\alpha^2(x^2 + y^2) - 2\alpha xy}{1 - \alpha^2} \right). \tag{5.14}$$

Setting $x = y$ and define

$$G(k, y) = \sum_{n=0}^{\infty} \frac{e^{-kn}}{2^n n!} [H_n(y)]^2 = \frac{\exp\left[2y^2/(1 + e^k) \right]}{\sqrt{1 - e^{-2k}}}, \tag{5.15}$$

Eq. (5.12) can then be expressed as

$$Q_{10} = \sum_{n=0}^{\infty} e^{-\beta \epsilon(n)} |\phi_n(x)|^2 = \sqrt{\frac{\omega}{\pi}} e^{-\beta\omega/2 - \omega x^2} G(\beta\omega, \sqrt{\omega} x). \tag{5.16}$$

---

[2]The following paragraphs summarizes the derivations in Ref. [169].

More generally, when $x \neq y$ and the system is in d dimensions, the matrix element in the coordinate space can be written as

$$\langle \mathbf{x}|e^{-\beta \hat{H}_0}|\mathbf{y}\rangle = \sum_{\mathbf{n}=0}^{\infty} \langle \mathbf{x}|\mathbf{n}\rangle \langle \mathbf{n}|e^{-\beta \hat{H}_0}|\mathbf{n}\rangle \langle \mathbf{n}|\mathbf{y}\rangle \equiv \rho(\mathbf{x},\mathbf{y}). \tag{5.17}$$

$\rho(\mathbf{x},\mathbf{y})$ is called the Mehler kernel and takes the form of

$$\rho(\mathbf{x},\mathbf{y}) = \frac{1}{\lambda_T^3} \left[\frac{\beta \omega}{\sinh(\tau\omega)} \right]^{3/2} \exp[-\mathbf{Z}^T B \mathbf{Z}], \tag{5.18}$$

where $\mathbf{Z}^T = (\mathbf{x}^T/\lambda_T, \mathbf{y}^T/\lambda_T)$, and matrix B is

$$B = \frac{\pi\beta\omega}{\sinh(\tau\omega)} \begin{pmatrix} \cosh(\tau\omega)\mathbb{1} & -\mathbb{1} \\ -\mathbb{1} & \cosh(\tau\omega)\mathbb{1} \end{pmatrix}, \tag{5.19}$$

with $\mathbb{1}$ is the d-dimensional identity matrix.

5.2.2: Automated-algebra method in coordinate space

With the Mehler kernel, we can represent the transfer matrix in a compact from. For the simplest example, the transfer matrix of the (1+1) system is written as,

$$\begin{aligned}
[\mathcal{M}_{11}]_{\mathbf{XY}} &= \langle \mathbf{x}_1 \mathbf{x}_2 | e^{-\tau \hat{H}_0} e^{-\tau \hat{V}} | \mathbf{y}_1 \mathbf{y}_2 \rangle \\
&= \rho(\mathbf{x}_1, \mathbf{y}_1)\rho(\mathbf{x}_2, \mathbf{y}_2) \left[\mathbb{1} + C\delta(\mathbf{y}_1 - \mathbf{y}_2) \right],
\end{aligned} \tag{5.20}$$

where $C = (e^{\tau g} - 1)$ is the same coupling constant as defined before. It is now clear that the physics meaning of Mehler kernel is just the propagator for the quantum harmonic oscillator.

The AA method works in the coordinate space in nearly the same way as it in the momentum

space. The general form of the matrix element is

$$
\begin{aligned}
[\mathcal{M}_{MN}^{N_\tau}]_{\mathbf{X}^0 \mathbf{X}^{N_\tau}} &= \left\langle \mathbf{X}^0 \middle| \prod_{N_\tau} e^{-\tau \hat{H}_0} e^{-\tau \hat{V}} \middle| \mathbf{X}^{N_\tau} \right\rangle \\
&= \sum_{\mathbf{X}^1 \mathbf{X}^2 \dots \mathbf{X}^{N_\tau - 1}} [M_{MN}]_{\mathbf{X}^0 \mathbf{X}^1} [M_{MN}]_{\mathbf{X}^1 \mathbf{X}^2} \cdots [M_{MN}]_{\mathbf{X}^{N_\tau - 1} \mathbf{X}^{N_\tau}} \\
&= \sum_{\mathbf{X}^1 \mathbf{X}^2 \dots \mathbf{X}^{N_\tau - 1}} \rho(\mathbf{X}^0, \mathbf{X}^1) \rho(\mathbf{X}^1, \mathbf{X}^2) \cdots \rho(\mathbf{X}^{N_\tau - 1}, \mathbf{X}^{N_\tau}) \\
&\quad \times f_{MN}(\mathbf{X}^0, \mathbf{X}^1) f_{MN}(\mathbf{X}^2, \mathbf{X}^2) \cdots f_{MN}(\mathbf{X}^{N_\tau - 1}, \mathbf{X}^{N_\tau})
\end{aligned}
\tag{5.21}
$$

where $\rho(\mathbf{X}^\tau, \mathbf{X}^{\tau+1})$ is a shorthand for the product

$$
\rho(\mathbf{X}^\tau, \mathbf{X}^{\tau+1}) = \rho(\mathbf{x}_1^\tau, \mathbf{x}_1^{\tau+1}) \rho(\mathbf{x}_2^\tau, \mathbf{x}_2^{\tau+1}) \cdots \rho(\mathbf{x}_{M+N}^\tau, \mathbf{x}_{M+N}^{\tau+1})
\tag{5.22}
$$

and $f_{MN}(\mathbf{X}^\tau, \mathbf{X}^{\tau+1})$, in analogue to Eq. (2.27), is the coordinate representation of the interaction operator $e^{-\beta \hat{V}}$. We summarize the explicit expressions in Appendix. C.

All the other steps in the AA method for the homogeneous systems hold valid to evaluate the above expression. As we are now working in the coordinate representation, all terms will yield the same volume order. Therefore, we can no longer use the volume power counting for the analytic volume cancellation. In other words, we have to evaluate both connected and disconnected diagrams when calculating Q_N, which greatly increases the computational costs. However, it has no impact to the accuracy as all terms in the cancellation are still analytic polynomials.

In the end, the virial coefficients are expressed as a polynomial in C, just as in the homogeneous case. At each N_τ, we renormalize the bare coupling C to reproduce exactly the second-order coefficient Δb_2 such that the line of constant physics is followed in the extrapolation to $N_\tau \to \infty$, for each $\beta\omega$. At unitary, the second-order virial coefficient can be obtained by analytically solving the spectrum of a trapped two-body system [24], and the final expression is

$$
\Delta b_{2,T}(\beta\omega) = \frac{1}{4} \operatorname{sech}\left(\frac{\beta\omega}{2}\right).
\tag{5.23}
$$

In the homogeneous limit, it approaches

$$\Delta b_{2,T}(\beta\omega \to 0) = \frac{1}{4} \tag{5.24}$$

agreeing with the relation $\Delta b_{2,T}(\beta\omega \to 0) = 2^{-3/2}\Delta b_2$ as in Eq.(5.11) with the homogeneous $\Delta b_2 = 1/\sqrt{2}$ in the unitary limit.

Section 5.3: Results

5.3.1: Trapped virial coefficients

The AA method is purely analytic in theory, which means the resulting expressions can be written as symbolic functions of $\beta\omega$. However, it requires the symbolic evaluation of determinants, which is more expensive than the numerical evaluations. Therefore, at lower decomposition order when the computational costs is reasonable, we still performed the symbolic calculation and report the analytic results at $N_\tau = 1, 2$ as analytical functions of $\beta\omega$. However, when extrapolating to the large-N_τ limit, the larger-N_τ results are required. In this case, we selected multiple trap frequency samples and carried out the numerical evaluations as a compromise.

Analytic expressions at leading- and next-leading-order

At first, we report the analytical results as symbolic expressions of coupling strength C, trapping frequency $\beta\omega$, and the spatial dimension d at leading- and next-to-leading order. Higher-order calculations are also feasible with reasonable computational costs, but the resulting formulas are too long to fit properly in the dissertation.

At leading order $N_\tau = 1$, the analytic formulas for Δb_3 and Δb_4 were firstly reported in Ref. [169] by the other students from the same group, where the authors found qualitative agreement between the semiclassical results and the numerical results using PIMC [21][3]. Considering the effectiveness of semiclassical approximation observed in the previous works, these formulas offers benchmarks for calculations at larger N_τ and for systems with higher particle number for which no existing results are available.

We present below the leading-order expressions for subspace virial coefficients up to four-

---

[3]In the large $\beta\omega$ regime, quantitative agreements were observed as well.

Table 5.1: The maximum temporal steps $N_{\tau,\max}$ calculated with automated-algebra method for trapped Fermi gas.

Q_{MN}	Q_{11}	Q_{21}	Q_{31}	Q_{22}	Q_{41}	Q_{32}
$N_{\tau,\max}$	21	20	16	12	12	8

particle systems, and leave the formulas of the fifth-order coefficient and the next-to-leading order results to Appendix. D.

$$\Delta b_2 = \Delta b_{11} = \frac{1}{2} \frac{C}{\lambda_T^d} \left[\frac{\beta\omega}{2\sinh(\beta\omega)} \right]^{d/2}, \tag{5.25}$$

$$\Delta b_{21} = -\frac{\Delta b_2}{[2\cosh(\beta\omega) + 1]^{d/2}}. \tag{5.26}$$

$$\Delta b_{31} = \frac{2^{-d/2}\Delta b_2}{\cosh^{d/2}(\beta\omega)\,[2\cosh(\beta\omega) + 1]^{d/2}}, \tag{5.27}$$

$$\Delta b_{22} = \frac{2^{-3d/2}\Delta b_2}{\cosh^{d/2}(\beta\omega)\cosh^d(\beta\omega/2)} \left\{ 1 + 2^{d/2}\Delta b_2 \left[\cosh^{d/2}(\beta\omega) - 2^{d/2+1}\cosh^d(\beta\omega/2) \right] \right\} \tag{5.28}$$

All formulas up to the fifth order at both $N_\tau = 1$ and 2 are plotted in Fig. 5.1, together with the extrapolated numerical results.

Here we limit our discussion to the comparison between the analytic formulas, and further discussions on their comparison to the numerical (extrapolated) results are left to the next subsection, Compared the two analytical results (black dotted and dashed lines respectively) to the extrapolated results (blue dotted lines), we note that results at higher N_τ does not immediately or necessarily converge to the expected results, rather, we observed that the results could move *away* from the $N_\tau \to \infty$ limit before the asymptotic regime is reached, usually for $N_\tau > 2$. In particular, in the case of Δb_4 the next-to-leading order results are actually worse than the leading-order ones, which was never observed in the homogeneous system.

Only until some high value of N_τ, the convergence reaches the asymptotic regime and starts to decrease monotonically as N_τ increase. Thus, it is important to investigate as large N_τ as possible, even if low values are qualitatively correct. In Table. 5.1, we summarized the maximum temporal steps $N_{\tau,\max}$ explored for each subspace.
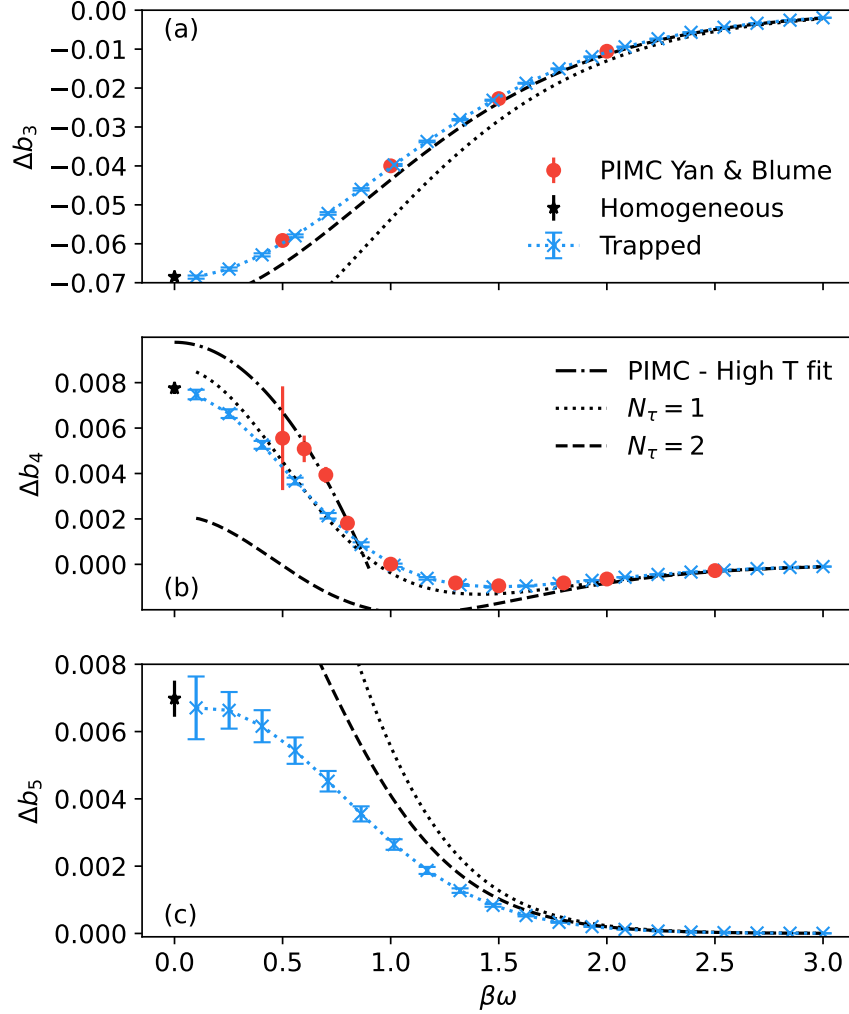
Figure 5.1: (a) Δb_3, (b) Δb_4, and (c) Δb_5 as functions of $\beta\omega$, for a trapped unitary Fermi gas. Our results are shown with blue crosses and error bars, joined by a blue dotted line. The data by Yan and Blume from Ref. [21] appears as red circles for (a) Δb_3 and (b) Δb_4, in both cases with error bars. The dashed-dotted line in the panel (b) shows a high-temperature fit to the data of Ref. [21]. Black stars with error bars show the our homogeneous results in , firstly reported in Ref. [104]. The dotted (dashed) line shows the $N_\tau = 1$ ($N_\tau = 2$) results given analytically in Appendix B. The latter show that, for Δb_3, increasing N_τ from 1 to 2 shows a clear improvement, whereas the case of Δb_4 is a cautionary tale: as N_τ goes from 1 to 2, the results move away from our final answer (blue crosses). In fact, it is not until $N_\tau = 5$ that Δb_4 reaches the asymptotic regime one can use for extrapolation. Ref. [56] presented a large-$\beta\omega$ asymptotic formula for Δb_n, but its validity is well outside the $0 < \beta\omega < 3$ region studied here.

107

Numerically extrapolated results in $N_\tau \to \infty$ limit

In Fig. 5.1 we show our results for (a) Δb_3, (b) Δb_4, and (c) Δb_5 for the trapped UFG as a function of $\beta\omega$. The error bars represent the uncertainty in the $N_\tau \to \infty$ extrapolation. The same error estimation scheme as that for the homogeneous case is used by taking the difference between the maximum and minimum predictions of polynomial extrapolation at different degree. For Δb_3 and Δb_4 we used polynomial fitting at degrees from 2 to 5, and for Δb_5 at degrees 2 and 3, as the $N_{\tau,\max}$ is more limited and the higher-degree polynomial fittings introduce uncontrolled artifacts.

Our results for Δb_3 are in superb agreement with the quantum Monte Carlo data of Ref. [21] over all trapping frequencies. For Δb_4 the story is slightly different: even though there is good agreement with Ref. [21] for $\beta\omega \geq 1$, a clear difference remains at low frequencies. We will return to explain this discrepancy very soon below. Finally, we predict Δb_5 as a function of $\beta\omega$, which has not been explored by any other literatures to the best of our knowledge.

For all virial coefficients in the homogeneous limit $\beta\omega \to 0$, we find good agreement with the homogeneous estimation (black stars) reported in Chap. 3. In the case of Δb_5 in the homogeneous limit, the error bar of the trapped virial coefficients (blue cross) appears much larger than the previous results. It is from the different $N_{\tau,\max}$ used for each subspace, especially for the $(3+2)$ subspace, due to the increasing computational costs as explained before.

As the HO potential confines the system, it naturally increases its kinetic energy, effectively reducing the interaction effects. This suggests that, for a given interaction strength, the VE should enjoy better convergence properties when a trapping potential is turned on (as argued also in Ref. [24]). Indeed, although our results indicate that $\Delta b_4 \simeq \Delta b_5$ and, moreover, for $0.3 < \beta\omega < 1.4$ we find $\Delta b_5 > |\Delta b_4|$, we also find that $|\Delta b_2| \gg |\Delta b_3| \gg |\Delta b_4|$. Specifically, at unitarity we find $\Delta b_3^{\mathrm{T}} = -0.0685(8)$, $\Delta b_4^{\mathrm{T}} = 0.00775(25)$, and $\Delta b_5^{\mathrm{T}} = 0.0070(5)$. Notably, the factor $n^{-3/2}$ in Eq. (5.11) restores the "normal order" $|\Delta b_3^{\mathrm{T}}| > |\Delta b_4^{\mathrm{T}}| > |\Delta b_5^{\mathrm{T}}|$, in contrast to the homogeneous case (see Sec. 3.2.2), supporting the notion that trapping potentials enhance the convergence of the virial expansion [54].

To better understand the differences in Δb_4 between our results and Ref. [21], we zoom in to study the subspace contributions Δb_{31} and Δb_{22}, as plotted in Fig. 5.2 (a). As pointed out in Ref. [21], these contributions partially cancel each other out. The increasing (effective) interact-
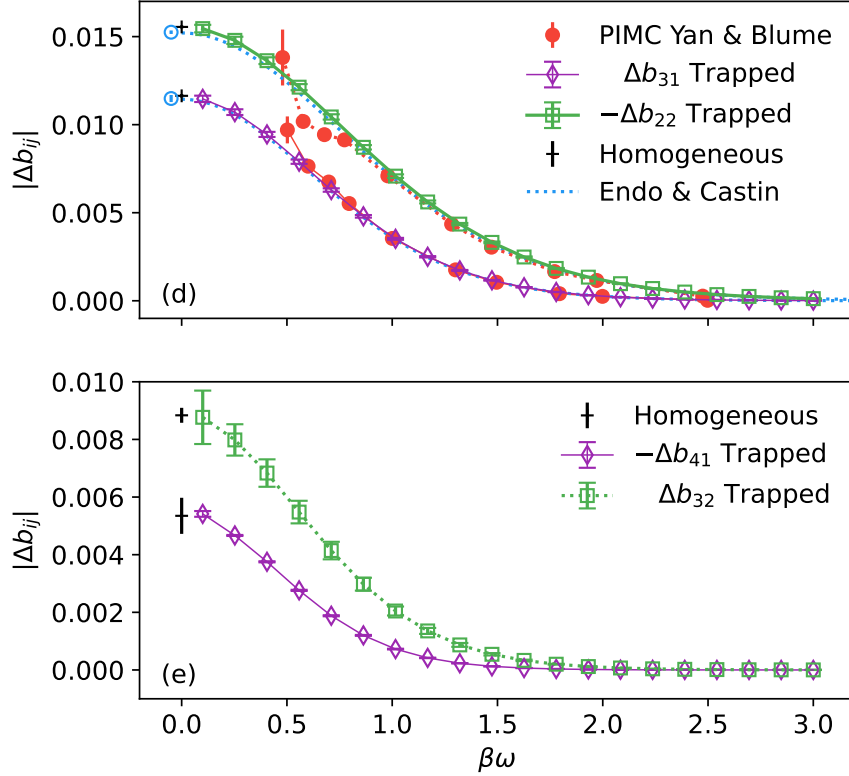
Figure 5.2: **(a)** Δb_{31} (blue diamonds) and $-\Delta b_{22}$ (green squares) as functions of $\beta\omega$, compared with the PIMC results of Ref. [21] (red circles joined by solid line for Δb_{31} and joined by a dotted line for Δb_{22}). The black crosses show our homogeneous results at $\beta\omega = 0$, as firstly reported in Ref. [104], The blue dotted lines are the results from Ref. [43] and the open circle represents the $\beta\omega \to 0$ limit. **(b)** $-\Delta b_{41}$ (blue diamonds) and Δb_{32} (green squares) as functions of $\beta\omega$. The black cross shows the results at $\beta\omega = 0$ from Ref. [104].

ing effects leads to the observed larger uncertainty as $\beta\omega$ decreases. Clearly, the largest difference arises in the determination of Δb_{22}, which is not unexpected as a contact interaction in that this subspace is less susceptible to Pauli blocking than Δb_{31}.

Similarly, in Figure 5.2 (b), we show our results for Δb_{41} and Δb_{32}, whose behavior parallels Δb_{31} and Δb_{22} in that they enter with different signs but similar magnitude, thus leading to increased uncertainty in the final result for Δb_5. Due to the different $N_{\tau,\max}$ used, the size of the error bars of Δb_{32} is larger than that of Δb_{41} as expected. But it may come as a surprise when compared to the case of the homogeneous results, where we reported less uncertainty for Δb_{32} than Δb_{41}. This is because that for the homogeneous results, both subspace coefficients were calculated at the same $N_\tau = 9$ order. In contrast, in the trapped case we achieved $N_\tau = 12$ for Δb_{41} but only $N_\tau = 8$ for Δb_{32}, due to the increasing computational cost.
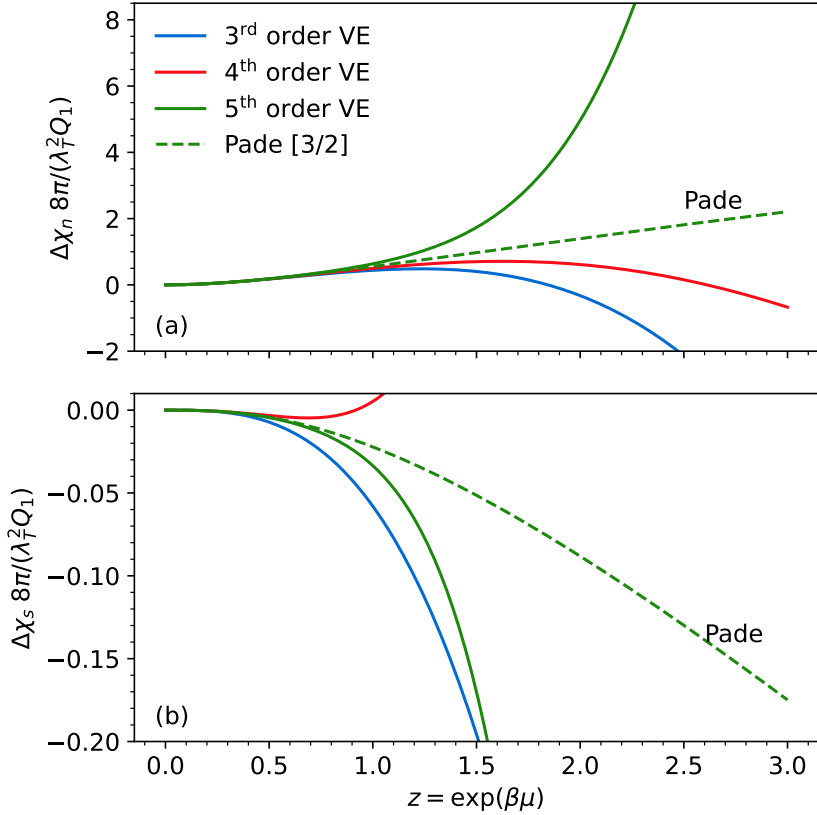
Figure 5.3: Density and spin susceptibilities as a function of fugacity at $\beta\omega \approx 0.55$ **(a)** Interaction effects on the density susceptibility $\Delta\chi_n$, in units of $8\pi/(\lambda_T^2 Q_1)$, as a function of the fugacity z for a harmonically trapped unitary Fermi gas at $\beta\omega = 1$. The second, third, fourth, and fifth-order VE results are shown, respectively, with dotted, dashed, dash-dotted, and solid lines. The Padé resummed result (with a [3/2] approximant) is shown as a blue line. **(b)** Interaction effects on the magnetic susceptibility $\Delta\chi_s$ as a function of z, for the same parameters as in the panel (a). The second-order VE is omitted because it is identically zero for $\Delta\chi_s$.

5.3.2: Density and spin susceptibilities

Lastly, to present an example of observable calculation, we plot the density and spin suscepti-bilities as defined in Eq. (3.33) in Fig. 5.3. The results are similar as the homogeneous case that we found divergent bare QVE results and the (seemingly) convergent resummed result. How-ever, due to the lack of existing benchmark results, we cannot decide if the seemingly convergent Padé curve is following the correct physics, neither can we narrow down the boundary that the resummed results start to deviate from the true physics. This is an excellent example showing the limitation of the current resummation method, leaving an open question for more investigations.

CHAPTER 6: Conclusion and outlook

In this dissertation, we focused on spin-1/2 Fermi gases using the QVE. To evaluate the higher-order coefficients in this expansion, we developed a nonperturbative, semi-analytical method we call Automated-Algebra. We firstly investigated the homogeneous system under different settings, with particular attention on the universal unitary limit. With this method, we estimated virial coefficients up to the unprecedented fifth order. For the third-order coefficient, we found excellent agreement with previous work with as low as 0.25% relative error at unitarity, the strongest interacting regime leading to largest calculation error. Our estimates of the fourth-order coefficient helped resolve a long-debated discrepancy among experimental determinations and different theoretical predictions. Moreover, our results generalized beyond all existing results at unitarity by extending to arbitrary coupling strength and arbitrary spatial dimension. At fifth-order, ours is the first quantitatively accurate estimation to the best of our knowledge (aside from a few precise estimates based on conjectures). We concluded that the non-negligible fifth-order contribution explains the large discrepancy in the determinations of the fourth-order coefficient, for which the fifth order coefficient was assumed to be small.

Using the high-order expansion, we investigated multiple observables, including but not limited to the density, Tan's contact and susceptibilities, and found good agreement with existing experimental and theoretical studies at high temperatures. Moreover, the higher-order coefficients allowed us to incorporate resummation techniques into our analysis, greatly extending the applicability of the QVE to lower-temperature regimes. In some situations, we found agreement with experimental results and Monte Carlo data up to temperature as low as the critical temperature of the superfluid transition. In particular, we demonstrated with an example how our calculations helped in the search of long-sought pseudogap regime, via the study of spin susceptibility, whose maximum and suppression are indicators of fermion pairing. The analytic expressions of coefficients help to yield smooth estimations of susceptibility, complementing the existing discrete results from stochastic methods.

We also generalized our method to harmonically trapped systems and calculated up to the

fifth order in that case as well, also for the first time. Once again benefitting from the analytic nature of our method, we observed nontrivial improvements in our fourth-order results as a function of external trapping frequency, especially in the regime close to the homogeneous limit, where the existing results suffered from severe statistical noises and extrapolation issues.

To summarize, we developed a new method to calculate high-order coefficients in the QVE. With those high-order coefficients and resummation methods, we found agreement between QVE and other methods in regimes unimagined before. Our work presents a potential direction for further investigations of QVE: with higher-order coefficients available, the QVE can be more than a benchmark method as used so far. Rather, with the analytic nature and relatively cheap computational cost, the QVE could serve as an ideal method for exploring novel phenomena, such as exploring phase diagrams or predicting at least qualitatively correct results in more general settings.

As a newly developed method, we look forward to the potential of the AA method in many other fields that have not been covered in this dissertation. One interesting direction is to explore its generalization to other observables. As the first step, a natural direction is to introduce local dependence. For example, one of our ongoing projects works on generalizing the global density $\langle \hat{n} \rangle$ to more "local" (in momentum space) $\langle \hat{n}(\mathbf{k}) \rangle$, i.e. the momentum distribution. The formalism described in Sec. 2.2.3 is generally valid. The main challenge is technical: due to the dependency on external variable $\mathbf{k}$, we need to either incorporate symbolic determinant evaluation for analytic results, or following the case of harmonic trapped system, repeat calculations at discrete values of $\mathbf{k}$ for numerical results.

Another kind of observables that attract of great interests is the calculation of correlations. One such example is the static structure factor, which attract attention from the astrophysics and nuclear matter communities for its connection to the differential cross section.

The vector (axial) static structure factor is defined as the Fourier transformation of spatial density-density (spin-spin) correlation

$$
\begin{aligned}
S_V(\mathbf{q}) &= \int \mathrm{d}^3\mathbf{r}\, e^{-i\mathbf{q}\cdot\mathbf{r}} \left\langle \delta n(\mathbf{r}, 0)\delta n(\mathbf{0}, 0) \right\rangle \\
S_V(\mathbf{q}) &= \int \mathrm{d}^3\mathbf{r}\, e^{-i\mathbf{q}\cdot\mathbf{r}} \left\langle \delta S_z(\mathbf{r}, 0)\delta S_z(\mathbf{0}, 0) \right\rangle
\end{aligned}
\tag{6.1}
$$

112

where $\delta n = n - \langle n \rangle$ and $\delta S_Z = S_z - \langle S_z \rangle$.

In a recent work, authors applied Monte method in large fugacity regime ($z = 1.0$ and 1.5) [170, 171], leaving an interesting open question to compare with the resummed QVE results. To apply the AA method, we can firstly perform the Fourier transformation analytically, converting the problem into an observable in the momentum space, which shares a similar structure as the momentum distribution as described above.

Beyond the static properties, we also wish to generalize the QVE and our method to the dynamical process. In a recent work [172], the authors successfully applied the second-order QVE to study the quantum quench process, leaving an open question to explore higher order with our semi-analytic method.

It is easy to incorporate the real-time evolution in our formalism by extending Eq. (2.59) to

$$W_N(t) = \text{tr}_N(e^{-\beta \hat{H}_0} e^{it\hat{H}} \hat{O} e^{-it\hat{H}}). \tag{6.2}$$

We can also incorporating the time-dependence into the static structure factor, i.e. the dynamic structure factor, which is shown to offer non-negligible correction to the differential cross section in some energy range [173]. The dynamic structure factor is defined as the Fourier transformation of spatial-temporal correlation, i.e.

$$\begin{aligned} S_V(\mathbf{q}, \omega) &= \int \text{d}^3\mathbf{r} e^{-i(\mathbf{q}\cdot\mathbf{r}-\omega t)} \langle \delta n(\mathbf{r}, t) \delta n(\mathbf{0}, 0) \rangle, \\ S_V(\mathbf{q}, \omega) &= \int \text{d}^3\mathbf{r} e^{-i(\mathbf{q}\cdot\mathbf{r}-\omega t)} \langle \delta S_z(\mathbf{r}, t) \delta S_z(\mathbf{0}, 0) \rangle. \end{aligned} \tag{6.3}$$

An even more complicated observable after the dynamic structure factor is the viscosity, which has been investigated recently with a second-order QVE [174–176].

Another goal on our wish list is to extend our work to other systems, in particular neutron matter (or even nuclear matter in the future). Connected through the universality at unitarity, many existing works [12, 35, 177–183] achieved success probing the neutron matter using the zero-range UFG system. However, for the zero-range approximation to hold true, we assume that the length scales follow $k_F a_s \gg 1$ and $k_F r_e \ll 1$. For neutrons, the scattering length $a_s = -18.5 \pm 0.3$fm and $r_e = 2.7$fm, limiting the universal regime to dilute ends with density $n < 10^{-4}$fm^{-3}[12].

To extend the QVE to denser regime, we have to incorporate the finite range correction term by introducing extra coupling parameters in the model.

Other systems of interest include e.g. four-component Fermi gas in 1D, which shows a one-dimensional analog of the BCS-BEC crossover [184], as well as the bosonic systems such as the Unitary Bose Gas [111, 185]. The four-component Fermi gas requires a four-body contact interaction, which has already been implemented in our method. But for the bosonic system, the interaction includes both two- and three-body forces to stabilize the system, which requires further investigation and code development.

APPENDIX A: COMPARISON BETWEEN THE TWO RENORMALIZATION PROCEDURES

In Sec. 2.2.4, we presented two different renormalization procedures. We claimed without demonstration that we will use the procedure I, i.e. renormalize to Δb_2. Here, we take a closer look to the procedure II and compare its results support our argument.

At first, we construct the transfer matrix using the coupling obtained with procedure I, i.e. the renormalized C tuned to $\Delta b_2^{\mathrm{UFG}}$. The largest eigenvalue $\bar{\lambda}_0$ of that matrix is then compared with the value λ_0 dictated by Lüscher's formula. In Fig. A.1, we plot the ratio $\bar{\lambda}_0/\lambda_0$ as a function of $1/N_\tau$ at different values of $x = \beta/L^2$. As $x \to 0$, which corresponds to the continuum limit, we find the ratio approaches 1, proving the equivalence of two procedures in the continuum limit.
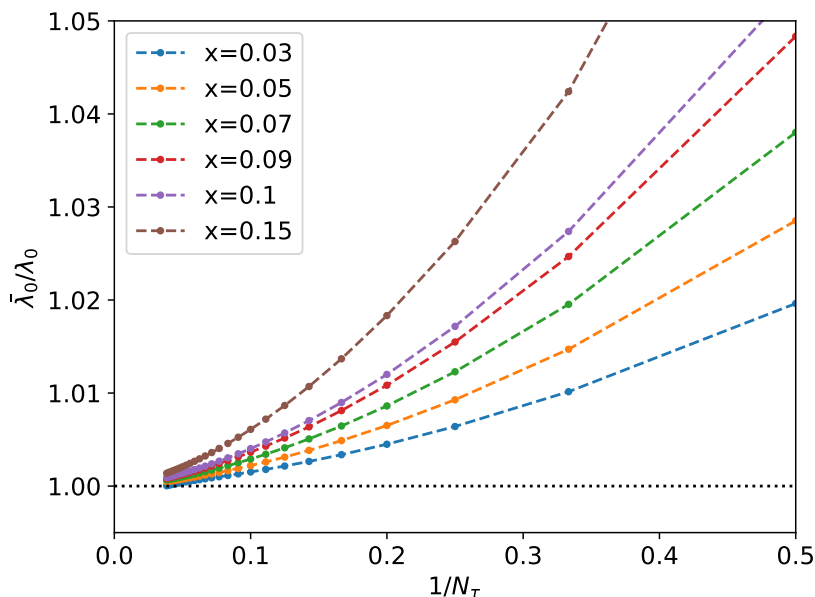
Figure A.1: The ratio between the largest eigenvalue $\bar{\lambda}_0$ of transfer matrix obtained for $\tilde{C}$ tuned to $\Delta b_2^{\mathrm{UFG}}$ and the one corresponding to Lüscher's formula λ_0, as functions of the discretization order k, shown as $1/k$, for several values of the parameter $x = \beta/L^2$.

To check their effects on the final estimations, we plot in Fig. A.2 and A.3 the estimations Δb_n using procedure II as a function of x. For comparison, we also plot the results using procedure I, which are expected to be consistent to each other in the $x \to 0$ limit.

In the left panel of Fig. A.2, we show a calculation of Δb_2 at unitarity using procedure II and

compare it to the analytic $\Delta b_2^{\mathrm{UFG}}$. As $x \to 0$, we find that Δb_2 differs from the analytic value by less than 0.25%. In the right panel, we show the corresponding results for Δb_3 and compare with the procedure I estimation (horizontal red line with shaded region representing the uncertainty). We find that the results of both procedures are consistent with each other within the uncertainties, with a slight deviation of $\approx 1\%$. Similarly, in Fig. A.3, we show the results for Δb_4 (left panel) and Δb_5 (right panel) and we find consistent results for both cases as well.

In summary, the two procedures are consistent in the continuum limit. In our examination, the procedure II differed from the analytic results with a minor error in the continuum limit, which partially explain the deviations in Δb_n for $n \geq 3$ with a similar magnitude. In addition, the procedure I does not require an extra extrapolation to $x \to 0$ limit, saving from another source of systematical errors. From a physical standpoint, in procedure I, Δb_2 can be interpreted as encoding the whole spectrum, rather than the lowest state as in procedure II, and is therefore more appropriate for the finite-temperature systems.
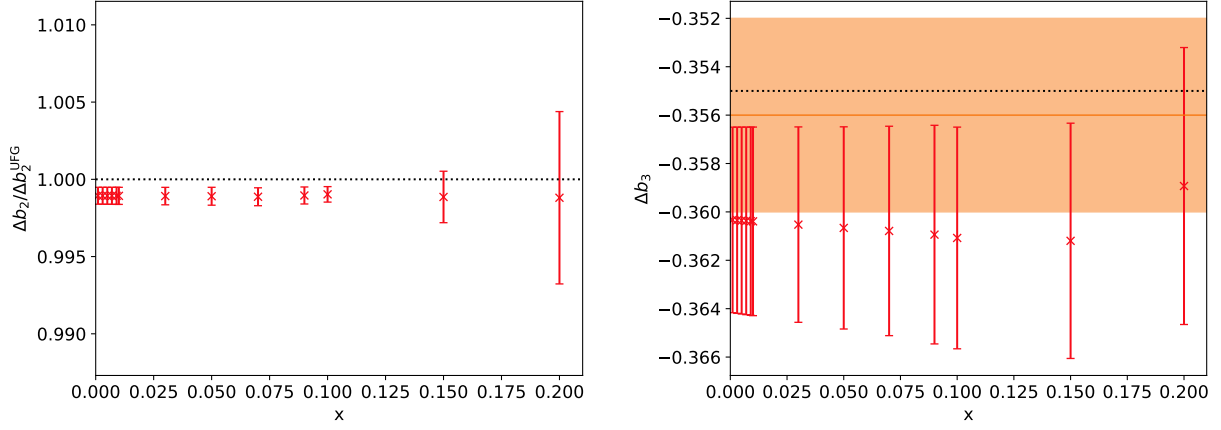
Figure A.2: **Left**: Results for Δb_2 (red error bars) at unitarity using our renormalization procedure II and the extrapolation scheme explained in the previous section, as a function of x. **Right**: Same as left but for Δb_3 (red error bars) compared with our renormalization procedure I (orange error band); the dotted line shows $\Delta b_3 = 0.3551$ (note that the entire vertical scale in this plot covers a range that is about 4% of the expected value).
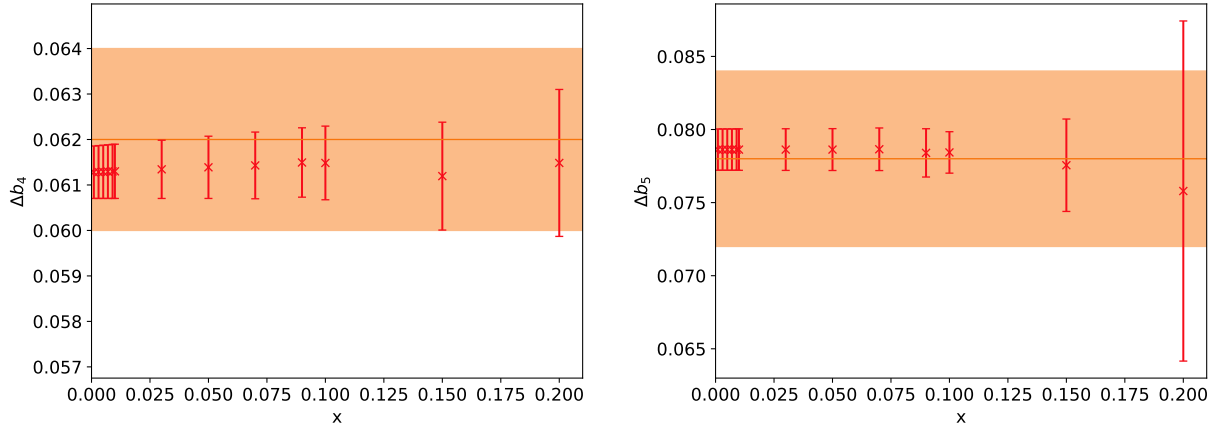
Figure A.3: **Left**: Results for Δb_4 (red error bars) at unitarity using our renormalization procedure II and the extrapolation scheme explained in the previous section, as a function of x, compared with our renormalization procedure I (orange error band). **Right**: Same as left but for Δb_5. Note: the entire vertical scales in these plots cover ranges of 11% (left) and 30% (right) of the final reported values of Δb_4 and Δb_5, respectively.

APPENDIX B: USEFUL EXPRESSIONS FOR VIRIAL COEFFICIENTS AND PARTITIONS FUNCTIONS

Section B.1: High-order virial expansion formulas

For completeness, we provide here some of the formulas which we omitted in the main text for the sake of brevity and clarity. These are model independent, except as noted below. The complete expressions for b_5, b_6, and b_7 in terms of the corresponding canonical partition functions and prior virial coefficients can be written as

$$Q_1 b_5 = Q_5 - (b_4 + b_2 b_3)Q_1^2 - (b_2^2 + b_3)\frac{Q_1^3}{2} - b_2\frac{Q_1^4}{3!} - \frac{Q_1^5}{5!}, \tag{B.1}$$

$$Q_1 b_6 = Q_6 - \left(b_5 + \frac{b_3^2}{2} + b_2 b_4\right)Q_1^2 - \left(\frac{b_2^3}{6} + \frac{b_4}{2} + b_3 b_2\right)Q_1^3$$
$$- \left(\frac{b_2^2}{2} + \frac{b_3}{3}\right)\frac{Q_1^4}{2!} - b_2\frac{Q_1^5}{4!} - \frac{Q_1^6}{6!}, \tag{B.2}$$

$$Q_1 b_7 = Q_7 - (b_6 + b_2 b_5 + b_3 b_4)Q_1^2 - \left(\frac{b_3^2}{2} + \frac{b_5}{2} + b_2 b_4 + \frac{b_3 b_2^2}{2}\right)Q_1^3$$
$$- \left(\frac{b_2^3}{6} + \frac{b_4}{6} + \frac{b_3 b_2}{2}\right)Q_1^4 - \left(b_2^2 + \frac{b_3}{2}\right)\frac{Q_1^5}{12} - b_2\frac{Q_1^6}{5!} - \frac{Q_1^7}{7!}, \tag{B.3}$$

whereas the change in the above due to interactions (assuming here two-body interactions) are given by

$$Q_1 \Delta b_5 = \Delta Q_5 - \Delta(b_4 + b_2 b_3)Q_1^2 - \frac{1}{2}\Delta\left(b_2^2 + b_3\right)Q_1^3 - \frac{\Delta b_2}{3!}Q_1^4, \tag{B.4}$$

$$Q_1 \Delta b_6 = \Delta Q_6 - \Delta\left(b_5 + \frac{b_3^2}{2} + b_2 b_4\right)Q_1^2 - \Delta\left(\frac{b_2^3}{6} + \frac{b_4}{2} + b_3 b_2\right)Q_1^3$$
$$- \Delta\left(\frac{b_2^2}{4} + \frac{b_3}{6}\right)Q_1^4 - \frac{\Delta b_2}{4!}Q_1^5, \tag{B.5}$$

$$Q_1 \Delta b_7 = \Delta Q_7 - \Delta(b_6 + b_2 b_5 + b_3 b_4)Q_1^2 - \Delta\left(\frac{b_3^2}{2} + \frac{b_5}{2} + b_2 b_4 + \frac{b_3 b_2^2}{2}\right)Q_1^3$$
$$- \Delta\left(\frac{b_2^3}{6} + \frac{b_4}{6} + \frac{b_3 b_2}{2}\right)Q_1^4 - \Delta\left(\frac{b_2^2}{12} + \frac{b_3}{24}\right)Q_1^5 - \frac{\Delta b_2}{5!}Q_1^6. \tag{B.6}$$

To use these, it is useful to have the following:

$$\Delta(b_n)^2 = \Delta(b_n^2) + 2b_n^{(0)}\Delta b_n, \tag{B.7}$$

$$\Delta(b_n)^3 = \Delta(b_n^3) + 3b_n^{(0)}\Delta(b_n^2) + 3(b_n^{(0)})^2\Delta b_n, \tag{B.8}$$

$$\Delta(b_n b_m) = \Delta b_n \Delta b_m + b_n^{(0)} \Delta b_m + b_m^{(0)} \Delta b_n, \tag{B.9}$$

$$\Delta(b_n b_m^2) = \Delta b_n (\Delta b_m)^2 + b_n^{(0)} (\Delta b_m)^2 + 2 b_m^{(0)} \Delta b_n \Delta b_m + 2 b_n^{(0)} b_m^{(0)} \Delta b_m + (b_m^{(0)})^2 \Delta b_n. \tag{B.10}$$

APPENDIX C: TRANSFER MATRIX FOR HARMONICALLY TRAPPED SYSTEMS

Section C.1: Three-particle space

Here we will need

$$\exp\left(-\tau\hat{V}\right)|\mathbf{X}) = \left[\mathbb{1} + C(\delta(\mathbf{x}_1 - \mathbf{x}_3) + \delta(\mathbf{x}_2 - \mathbf{x}_3))\right]|\mathbf{X}), \tag{C.1}$$

where $\mathbf{X} = (\mathbf{x}_1, \mathbf{x}_2, \mathbf{x}_3)$ is a collective index, and we use $|\mathbf{X})$ to denote a state of distinguishable particles (i.e. no antisymmetrization among the $\mathbf{x}_i$ labels). We thus obtain

$$[\mathcal{M}_{21}]_{\mathbf{x}_1,\mathbf{x}_2,\mathbf{x}_3;\mathbf{y}_1,\mathbf{y}_2,\mathbf{y}_3} = \rho(\mathbf{x}_1,\mathbf{y}_1)\rho(\mathbf{x}_2,\mathbf{y}_2)\rho(\mathbf{x}_3,\mathbf{y}_3)\left[\mathbb{1} + C(\delta(\mathbf{y}_1 - \mathbf{y}_3) + \delta(\mathbf{y}_2 - \mathbf{y}_3))\right]. \tag{C.2}$$

Section C.2: Four-particle space

Here we distinguish the 3+1 subspace from the 2+2 subspace.

For the 3+1 case,

$$\exp\left(-\tau\hat{V}\right)|\mathbf{X}) = \left[\mathbb{1} + C(\delta(\mathbf{x}_1 - \mathbf{x}_4) + \delta(\mathbf{x}_2 - \mathbf{x}_4) + \delta(\mathbf{x}_3 - \mathbf{x}_4))\right]|\mathbf{X}), \tag{C.3}$$

where $\mathbf{X} = (\mathbf{x}_1, \mathbf{x}_2, \mathbf{x}_3, \mathbf{x}_4)$, and so we obtain

$$\begin{aligned}[\mathcal{M}_{31}]_{\mathbf{X},\mathbf{Y}} =&\rho(\mathbf{x}_1,\mathbf{y}_1)\rho(\mathbf{x}_2,\mathbf{y}_2)\rho(\mathbf{x}_3,\mathbf{y}_3)\rho(\mathbf{x}_4,\mathbf{y}_4) \\ &\times \left[\mathbb{1} + C(\delta(\mathbf{y}_1 - \mathbf{y}_4) + \delta(\mathbf{y}_2 - \mathbf{y}_4) + \delta(\mathbf{y}_3 - \mathbf{y}_4))\right].\end{aligned} \tag{C.4}$$

For the 2+2 case, on the other hand,

$$\begin{aligned}\exp\left(-\tau\hat{V}\right)|\mathbf{X}) =& \left[\mathbb{1} + C(\delta(\mathbf{x}_1 - \mathbf{x}_3) + \delta(\mathbf{x}_1 - \mathbf{x}_4) + \delta(\mathbf{x}_2 - \mathbf{x}_3) + \delta(\mathbf{x}_2 - \mathbf{x}_4)) \right. \\ &+ \left. C^2(\delta(\mathbf{x}_1 - \mathbf{x}_3)\delta(\mathbf{x}_2 - \mathbf{x}_4) + \delta(\mathbf{x}_1 - \mathbf{x}_4)\delta(\mathbf{x}_2 - \mathbf{x}_3))\right]|\mathbf{X}),\end{aligned} \tag{C.5}$$

such that

$$[\mathcal{M}_{22}]_{\mathbf{X},\mathbf{Y}} = \rho(\mathbf{x}_1,\mathbf{y}_1)\rho(\mathbf{x}_2,\mathbf{y}_2)\rho(\mathbf{x}_3,\mathbf{y}_3)\rho(\mathbf{x}_4,\mathbf{y}_4)$$

$$\times \left[\mathbb{1} + C(\delta(\mathbf{y}_1 - \mathbf{y}_3) + \delta(\mathbf{y}_1 - \mathbf{y}_4) + \delta(\mathbf{y}_2 - \mathbf{y}_3) + \delta(\mathbf{y}_2 - \mathbf{y}_4))\right. \tag{C.6}$$

$$\left. + C^2(\delta(\mathbf{y}_1 - \mathbf{y}_3)\delta(\mathbf{y}_2 - \mathbf{y}_4) + \delta(\mathbf{y}_1 - \mathbf{y}_4)\delta(\mathbf{y}_2 - \mathbf{y}_3))\right].$$

Section C.3:   Five-particle space

Here we distinguish the 4+1 subspace from the 3+2 subspace.

For the 4+1 case,

$$\exp\left(-\tau\hat{V}\right)|\mathbf{X}\rangle \;=\; \left[\mathbb{1} + C(\delta(\mathbf{x}_1 - \mathbf{x}_5) + \delta(\mathbf{x}_2 - \mathbf{x}_5) + \delta(\mathbf{x}_3 - \mathbf{x}_5) + \delta(\mathbf{x}_4 - \mathbf{x}_5))\right]|\mathbf{X}\rangle, \quad \text{(C.7)}$$

where $\mathbf{X} = (\mathbf{x}_1, \mathbf{x}_2, \mathbf{x}_3, \mathbf{x}_4, \mathbf{x}_5)$, such that

$$[\mathcal{M}_{41}]_{\mathbf{X},\mathbf{Y}} = \rho(\mathbf{x}_1,\mathbf{y}_1)\rho(\mathbf{x}_2,\mathbf{y}_2)\rho(\mathbf{x}_3,\mathbf{y}_3)\rho(\mathbf{x}_4,\mathbf{y}_4)\rho(\mathbf{x}_5,\mathbf{y}_5) \times$$

$$\left[\mathbb{1} + C(\delta(\mathbf{y}_1 - \mathbf{y}_5) + \delta(\mathbf{y}_2 - \mathbf{y}_5) + \delta(\mathbf{y}_3 - \mathbf{y}_5) + \delta(\mathbf{y}_4 - \mathbf{y}_5))\right] \tag{C.8}$$

For the 3+2 case, on the other hand,

$$\exp\left(-\tau\hat{V}\right)|\mathbf{X}\rangle$$

$$= \left\{\mathbb{1} + C\left[\delta(\mathbf{x}_1 - \mathbf{x}_4) + \delta(\mathbf{x}_1 - \mathbf{x}_5) + \delta(\mathbf{x}_2 - \mathbf{x}_4) + \delta(\mathbf{x}_2 - \mathbf{x}_5) + \delta(\mathbf{x}_3 - \mathbf{x}_4) + \delta(\mathbf{x}_3 - \mathbf{x}_5)\right]\right.$$

$$+ C^2\left[\delta(\mathbf{x}_1 - \mathbf{x}_4)\delta(\mathbf{x}_2 - \mathbf{x}_5) + \delta(\mathbf{x}_1 - \mathbf{x}_5)\delta(\mathbf{x}_2 - \mathbf{x}_4)\right. \tag{C.9}$$

$$\left.\left. + \delta(\mathbf{x}_1 - \mathbf{x}_4)\delta(\mathbf{x}_3 - \mathbf{x}_5) + \delta(\mathbf{x}_1 - \mathbf{x}_5)\delta(\mathbf{x}_3 - \mathbf{x}_4)\right]\right\}|\mathbf{X}\rangle,$$

such that

$$[\mathcal{M}_{32}]_{\mathbf{X},\mathbf{Y}} = \rho(\mathbf{x}_1,\mathbf{y}_1)\rho(\mathbf{x}_2,\mathbf{y}_2)\rho(\mathbf{x}_3,\mathbf{y}_3)\rho(\mathbf{x}_4,\mathbf{y}_4)\rho(\mathbf{x}_5,\mathbf{y}_5) \times$$

$$\left[\mathbb{1} + C(\delta(\mathbf{y}_1 - \mathbf{y}_4) + \delta(\mathbf{y}_1 - \mathbf{y}_5) + \delta(\mathbf{y}_2 - \mathbf{y}_4) + \delta(\mathbf{y}_2 - \mathbf{y}_5) + \delta(\mathbf{y}_3 - \mathbf{y}_4) + \delta(\mathbf{y}_3 - \mathbf{y}_5)) + \right.$$

$$C^2(\delta(\mathbf{y}_1 - \mathbf{y}_4)\delta(\mathbf{y}_2 - \mathbf{y}_5) + \delta(\mathbf{y}_1 - \mathbf{y}_5)\delta(\mathbf{y}_2 - \mathbf{y}_4) + \delta(\mathbf{y}_1 - \mathbf{y}_4)\delta(\mathbf{y}_3 - \mathbf{y}_5) + \delta(\mathbf{y}_1 - \mathbf{y}_5)\delta(\mathbf{y}_3 - \mathbf{y}_4) \tag{C.10}$$

APPENDIX D: ANALYTIC EXPRESSIONS OF TRAPPED VIRIAL COEFFICIENTS AT LEADING- AND NEXT-TO-LEADING ORDER

As mentioned in Sec. 5.3.1, we present formulas for the subspace virial coefficients at leading-($N_\tau = 1$) and next-to-leading ($N_\tau = 2$) Trotter-Suzuki decomposition for arbitrary spatial dimension d, trapping frequency $\beta\omega$, and coupling strength (parameterized by Δb_2). For completeness, the results that have already been reported in the main text are presented as well.

Section D.1:   Analytic expressions at leading order

$$\Delta b_{11} = \frac{C}{\lambda_T^d} \left(\frac{\beta\omega}{\sinh(\beta\omega)}\right)^{d/2} \frac{1}{2 \times 2^{d/2}}, \tag{D.1}$$

$$\Delta b_{21} = -\frac{\Delta b_2}{[2\cosh(\beta\omega) + 1]^{d/2}}, \tag{D.2}$$

$$\Delta b_{31} = \frac{2^{-d/2} \Delta b_2}{\cosh^{d/2}(\beta\omega)\,[2\cosh(\beta\omega) + 1]^{d/2}}, \tag{D.3}$$

$$\Delta b_{22} = \frac{2^{-3d/2}\Delta b_2}{\cosh^{d/2}(\beta\omega)\cosh^d(\beta\omega/2)} \tag{D.4}$$

$$\times \left\{1 + 2^{d/2}\Delta b_2\left[\cosh^{d/2}(\beta\omega) - 2^{d/2+1}\cosh^d(\beta\omega/2)\right]\right\}, \tag{D.5}$$

$$\Delta b_{41} = -\frac{2^{-d/2}\Delta b_2}{\cosh^{d/2}(\beta\omega)\,[2\cosh(\beta\omega) + 2\cosh(2\beta\omega) + 1]^{d/2}}, \tag{D.6}$$

$$\Delta b_{32} = -\Delta b_2\left[\frac{\cosh(\beta\omega) - 1}{2\cosh^2(2\beta\omega) - \cosh(\beta\omega) - 1}\right]^{d/2} \tag{D.7}$$

$$+ 2(\Delta b_2)^2 \left\{\frac{1}{[1 + 2\cosh(\beta\omega) + 2\cosh(2\beta\omega)]^{d/2}} + \frac{2^d}{[7 + 8\cosh(2\beta\omega)]^{d/2}}\right.$$

$$\left. - \frac{2^d}{[11 + 16\cosh(\beta\omega) + 8\cosh(2\beta\omega)]^{d/2}}\right\}.$$

Section D.2: Analytic expressions at next-to-leading order

$$\Delta b_{11} = \frac{C}{\lambda_T^d}\left(\frac{\beta\omega}{\sinh(\beta\omega)}\right)^{d/2}\frac{1}{2^{d/2}} + \left(\frac{C}{\lambda_T^d}\right)^2\left(\frac{(\beta\omega)^2}{\sinh^2(\beta\omega/2)}\right)^{d/2}\frac{1}{2^{d+1}} \tag{D.8}$$

$$\begin{aligned}
\Delta b_{21} =& \frac{C}{\lambda_T^d}\left(\frac{\beta\omega}{\sinh(\beta\omega)}\right)^{d/2}\frac{-1}{[2+4\cosh(\beta\omega)]^{d/2}}\\
&+\left(\frac{C}{\lambda_T^d}\right)^2\left(\frac{(\beta\omega)^2}{\sinh^2(\beta\omega/2)}\right)^{d/2}\left\{\frac{1}{2^{d+1}}\frac{1}{[1+2\cosh(\beta\omega)]^{d/2}}+\frac{-1}{[7+8\cosh(\beta\omega)]^{d/2}}\right\}
\end{aligned} \tag{D.9}$$

$$\begin{aligned}
\Delta b_{31} =& \frac{C}{\lambda_T^d}\left(\frac{\beta\omega}{\sinh(\beta\omega)}\right)^{d/2}\frac{1}{2^d}\frac{1}{[(1+\cosh(\beta\omega)+\cosh(2\beta\omega))]^{d/2}}\\
&+\left(\frac{C}{\lambda_T^d}\right)^2\left(\frac{(\beta\omega)^2}{\sinh^2(\beta\omega/2)}\right)^{d/2}\left\{\frac{1}{[10+14\cosh(\beta\omega)+8\cosh(2\beta\omega)]^{d/2}}\right.\\
&\left.+\frac{-1}{4^d}\frac{1}{[2\cosh^2(\beta\omega/2)\cosh(\beta\omega)]^{d/2}}+\frac{1}{2^{2d+1}}\frac{1}{[\cosh^2(\beta\omega/2)(1+2\cosh(\beta\omega))]^{d/2}}\right\}
\end{aligned} \tag{D.10}$$

$$\begin{aligned}
\Delta b_{22} =& \frac{C}{\lambda_T^d}\left(\frac{\beta\omega}{\sinh(\beta\omega)}\right)^{d/2}\frac{1}{4^d}\frac{1}{[\cosh^2(\beta\omega/2)\cosh(\beta\omega)]^{d/2}}\\
&+\left(\frac{C}{\lambda_T^d}\right)^2\left(\frac{(\beta\omega)^2}{\sinh^2(\beta\omega/2)}\right)^{d/2}\\
&\quad\times\left\{\frac{1}{2^{3d+1}}\frac{1}{[\cosh^4(\beta\omega/2)]^{d/2}}+\frac{-1}{[32\cosh^2(\beta\omega/2)\cosh(\beta\omega)]^{d/2}}\right.\\
&\quad\left.+\frac{2}{[\cosh^2(\beta\omega/2)(16+32\cosh(\beta\omega))]^{d/2}}+\frac{-2}{[10+14\cosh(\beta\omega)+8\cosh(2\beta\omega)]^{d/2}}\right\}\\
&+\left(\frac{C}{\lambda_T^d}\right)^3\left(\frac{(\beta\omega)^3}{\sinh^3(\beta\omega/2)}\right)^{d/2}\\
&\quad\times\left\{\frac{-4}{[24\cosh(\beta\omega/2)+16\cosh(3\beta\omega/2)]^{d/2}}+\frac{2}{[64\cosh^3(\beta\omega/2)]^{d/2}}+\left[\frac{\sinh(\beta\omega/2)}{8\sinh(2\beta\omega)}\right]^{d/2}\right\}\\
&+\left(\frac{C}{\lambda_T^d}\right)^4\left(\frac{(\beta\omega)^4}{\sinh^4(\beta\omega/2)}\right)^{d/2}\left\{\frac{-1}{[16+32\cosh(\beta\omega)]^{d/2}}+\frac{3}{4}\frac{1}{[64\cosh^2(\beta\omega/2)]^{d/2}}\right\}
\end{aligned} \tag{D.11}$$

$$\begin{aligned}
\Delta b_{41} =& \frac{C}{\lambda_T^d}\left(\frac{\beta\omega}{\sinh(\beta\omega)}\right)^{d/2}\frac{-1}{[4(1+2\cosh(\beta\omega)+\cosh(2\beta\omega)+\cosh(3\beta\omega))]^{d/2}}\\
&+\left(\frac{C}{\lambda_T^d}\right)^2\left(\frac{(\beta\omega)^2}{\sinh^2(\beta\omega/2)}\right)^{d/2}\left\{\frac{-1}{[13+20\cosh(\beta\omega)+14\cosh(2\beta\omega)+8\cosh(3\beta\omega)]^{d/2}}\right.
\end{aligned}$$

$$+\frac{1}{[4(3+6\cosh(\beta\omega)+4\cosh(2\beta\omega)+2\cosh(3\beta\omega)]^{d/2}}$$
$$+\frac{-1}{[23+40\cosh(\beta\omega)+24\cosh(2\beta\omega)+8\cosh(3\beta\omega)]^{d/2}}$$
$$+\frac{1}{2}\frac{1}{[4\cosh^2(\beta\omega/2)(4+8\cosh(\beta\omega)+8\cosh(2\beta\omega)]^{d/2}}\Bigg\} \tag{D.12}$$

$$
\begin{aligned}
\Delta b_{32} =\ & \frac{C}{\lambda_T^d}\left(\frac{\beta\omega}{\sinh(\beta\omega)}\right)^{d/2}\frac{-1}{[6+12\cosh(\beta\omega)+8\cosh(2\beta\omega)+4\cosh(3\beta\omega)]^{d/2}} \\
& + \left(\frac{C}{\lambda_T^d}\right)^2\left(\frac{(\beta\omega)^2}{\sinh^2(\beta\omega/2)}\right)^{d/2}\Bigg\{\frac{1}{[4\cosh^2(\beta\omega/2)(4+8\cosh(\beta\omega)+8\cosh(2\beta\omega))]^{d/2}} \\
& + \frac{1}{[\cosh^2(\beta\omega/2)(28+32\cosh(2\beta\omega))]^{d/2}} \\
& + \frac{-1}{[\cosh^2(\beta\omega/2)(44+64\cosh(\beta\omega)+32\cosh(2\beta\omega))]^{d/2}} \\
& + \frac{-2}{[23+40\cosh(\beta\omega)+24\cosh(2\beta\omega)+8\cosh(3\beta\omega)]^{d/2}} \\
& + \frac{1}{[\cosh^2(\beta\omega)(28+32\cosh(\beta\omega))]^{d/2}} \\
& + \frac{2}{[8\cosh^2(\beta\omega/2)(3+3\cosh(\beta\omega)+4\cosh(2\beta\omega))]^{d/2}} \\
& + \frac{-1}{[(1+2\cosh(\beta\omega))^2(7+8\cosh(\beta\omega))]^{d/2}} \\
& + \frac{1}{2}\frac{1}{[4(3+6\cosh(\beta\omega)+4\cosh(2\beta\omega)+2\cosh(3\beta\omega))]^{d/2}}\Bigg\} \\
& + \left(\frac{C}{\lambda_T^d}\right)^3\left(\frac{(\beta\omega)^3}{\sinh^3(\beta\omega/2)}\right)^{d/2}\Bigg\{\frac{1}{[\cosh(\beta\omega)(8+32\cosh(\beta\omega))]^{d/2}}\left[\frac{\sinh(\beta\omega/2)}{\sinh(\beta\omega)}\right]^{d/2} \\
& + \frac{-2}{[76\cosh(\beta\omega/2)+16(3\cosh(3\beta\omega/2)+\cosh(5\beta\omega/2))]^{d/2}} \\
& + \frac{-2}{[16\cosh(\beta\omega/2)(1+2\cosh(\beta\omega)+2\cosh(2\beta\omega))]^{d/2}} \\
& + \frac{2}{[4\cosh(\beta\omega/2)(5+12\cosh(\beta\omega)+8\cosh(2\beta\omega))]^{d/2}} \\
& + \frac{6}{[8\cosh(\beta\omega/2)\cosh(\beta\omega)(7+8\cosh(\beta\omega))]^{d/2}} \\
& + \frac{-4}{[4\cosh(\beta\omega/2)(15+22\cosh(\beta\omega)+8\cosh(2\beta\omega))]^{d/2}} \\
& + \frac{1}{[32\cosh^3(\beta\omega/2)(1+4\cosh(\beta\omega))]^{d/2}}\Bigg\} \\
& + \quad \text{see next page}
\end{aligned}
$$

$$+ \quad \left(\frac{C}{\lambda_T^d}\right)^4 \left(\frac{(\beta\omega)^4}{\sinh^4(\beta\omega/2)}\right)^{d/2} \left\{ \frac{-3}{[60 + 88\cosh(\beta\omega) + 32\cosh(2\beta\omega)]^{d/2}} \right.$$

$$+ \frac{3}{[41 + 72\cosh(\beta\omega) + 32\cosh(2\beta\omega)]^{d/2}} + \frac{1}{[33 + 40\cosh(\beta\omega) + 32\cosh(2\beta\omega)]^{d/2}}$$

$$+ \frac{1}{2}\frac{1}{[16(1 + 2\cosh(\beta\omega) + 2\cosh(2\beta\omega))]^{d/2}} + \frac{-1}{[4(1 + 4\cosh(\beta\omega))^2]^{d/2}}$$

$$+ \frac{-2}{[20 + 48\cosh(\beta\omega) + 32\cosh(2\beta\omega)]^{d/2}} + \frac{2}{[32\cosh^2(\beta\omega/2)(1 + 4\cosh(\beta\omega))]^{d/2}}$$

$$\left. + \frac{-1}{2}\frac{1}{[(7 + 8\cosh(\beta\omega))^2]^{d/2}} + \frac{1}{2}\frac{1}{[25 + 48\cosh(\beta\omega) + 32\cosh(2\beta\omega)]^{d/2}} \right\} \quad (\text{D}.13)$$

APPENDIX E: DIAGRAMMATIC REPRESENTATION OF AA METHOD

In this appendix, we present a diagrammatic representation of the expressions encountered when evaluating partition functions in AA method. Even though it is not practically useful for calculations at large N_τ due to the rapidly increasing complexities, it remains a convenient method at low N_τ and provides a bridge to Feynman diagrams.

Below, we take the ΔQ_{21} at $N_\tau = 2$ for example. For each time slice, we have

$$\langle p_1 p_2 p_3 | \exp\left(-\tau \hat{T}\right) \exp\left(-\tau \hat{V}\right) | q_1 q_2 q_3 \rangle$$
$$= \exp[-\tau \epsilon(p_1)] \exp[-\tau \epsilon(p_2)] \exp[-\tau \epsilon(p_3)] \langle p_1 p_2 p_3 | \exp\left(-\tau \hat{V}\right) | q_1 q_2 q_3 \rangle, \tag{E.1}$$

where the momentum representation of the interaction operator is

$$\langle p_1 p_2 p_3 | \exp\left(-\tau \hat{V}\right) | q_1 q_2 q_3 \rangle = \delta_{p_1,q_1} \delta_{p_2,q_2} \delta_{p_3,q_3} + C(\delta_{p_1+p_3,q_1+q_3} \delta_{p_2,q_2} + \delta_{p_2+p_3,q_2+q_3} \delta_{p_1,q_1}). \tag{E.2}$$

The subscripts $1, 2$ represent the spin-$\uparrow$ particles, subscript 3 the spin-$\downarrow$ particle. For simplicity, we consider only the 1D case but the generalization to arbitrary d dimension is straightforward by converting all variables to vectors.

We define the rules to represent the interaction matrix such that the line represents one momentum variable (not the propagator), the node represent one delta terms, and from left to right represents the imaginary time direction.

Therefore, the first term of Eq. (E.2) is represented as

where we usually omit the node for free particles, i.e. those who are not participating the interaction,

And the $\mathcal{O}(C)$ term is represented as

(E.4)

As argued in Sec. 2.2, the particles at intermediate imaginary time steps can be treated as classical. Correspondingly, the expansion of $\mathcal{M}^{N_\tau}$ is to connect the diagrams order by order.

In case of $N_\tau = 2$, the expression is up to the $\mathcal{O}(C^2)$ order. The $\mathcal{O}(C^0)$ order corresponds to the noninteracting case and is the same for arbitrary N_τ:

(E.5)

where we use the open circle to represent the propagator. A form closer to the Feynman diagram is to take the l.h.s. in Eq. (E.3),

(E.6)

Now the closed line, such as the one in the middle, represents the propagator just as in the Feynman diagram. However, as in our case the propagator is the decomposition $\exp(-\tau\epsilon)$, we prefer the form as in Eq. (E.5) for easier factor counting.

So far, we obtained the diagram representing the matrix element $[\mathcal{M}_{21}]^2$, and the last step is to evaluate the traces as shown in Eq. (2.50),

$$Q_{21} = \frac{1}{2!} \sum_{abc} \left\{ \left[\mathcal{M}_3^{N_\tau} \right]_{abc,abc} - \left[\mathcal{M}_3^{N_\tau} \right]_{abc,bac} \right\},$$

(E.7)

where we will call the first one the normal trace while the second "twisted" trace.

Diagrammatically, taking the trace corresponds to connect the open ends and leads to the final form of the diagram. For the normal trace, we use the boundary condition that $p_i = q_i, \forall i$ (see Eq. (2.73)), leading to the diagram
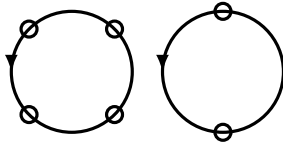
$$\tag{E.8}$$

where the arrow represents one integral variable and the number of open circles represents the factor in the propagator. The diagrams are implicitly multiplied together. The above diagram hence represents the integral

$$\left(\frac{L}{2\pi}\right)^3 \int dp_1 dp_2 dp_3 \ \exp[-2\tau\epsilon(p_1)]\exp[-2\tau\epsilon(p_2)]\exp[-2\tau\epsilon(p_2)]. \tag{E.9}$$
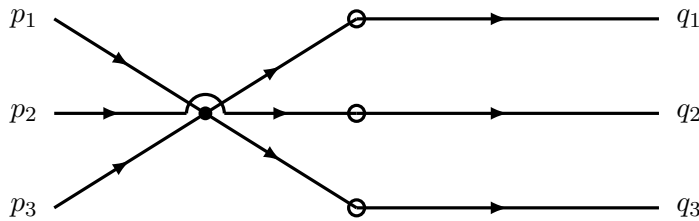
With $\tau = N_\tau/2$, the above integral is just $Q_{10}^3(\beta)$.

Similarly, for the "twisted" trace, we connect q_2 to p_1 and q_1 to p_2 (see Eq. (2.74)), which introduces a twisted knots, hence the name. The q_3 is normally connected to p_3. The resulting diagram is

$$\tag{E.10}$$

corresponding to $Q_{10}(2\beta)Q_{10}(\beta)$.

At $\mathcal{O}(C)$ order, by using the cyclic symmetry yields, we only need to consider one situation, i.e. $\mathcal{K}_0\mathcal{K}_1$ with degeneracy of 2, and it corresponds to two diagrams. The first diagram is

$$\tag{E.11}$$

and after taking the trace, we have the normal trace diagram as

$$(E.12)$$

where the first two-loop diagram represent the integral

$$\left(\frac{L}{2\pi}\right)^2 \int dp_1 dp_2 \exp[-2\tau\epsilon(p_1)] \exp[-2\tau\epsilon(p_1)] = Q_{10}^2(\beta).$$

$$(E.13)$$

The twisted trace diagram is
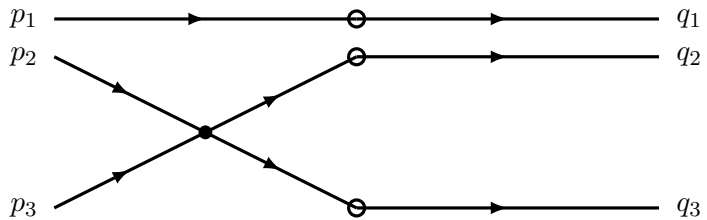
$$(E.14)$$

corresponding to the integral

$$\left(\frac{L}{2\pi}\right)^2 \int dp_1 dp_2 \exp[-4\tau\epsilon(p_1)] \exp[-2\tau\epsilon(p_1)] = Q_{10}(2\beta)Q_{10}(\beta).$$

$$(E.15)$$

Here we find that the normal trace diagram is disconnected and scales at L^3, while the twisted trace diagram is connected and scales at L^2. This is the diagrammatic representation of the analytic volume cancellation, as discussed in Sec. 1.3.2.

The second diagram is

$$(E.16)$$

whose trace is exactly the same as in Eq. (E.12) and (E.14).

At $\mathcal{O}(C^2)$, there are four different diagrams while two of them are identical to each other under cyclic symmetry. The two self-multiplication terms, and shares the same diagram (same under particle permutation symmetry)

$$\text{(E.17)}$$

The normal trace diagram is disconnected

$$\text{(E.18)}$$
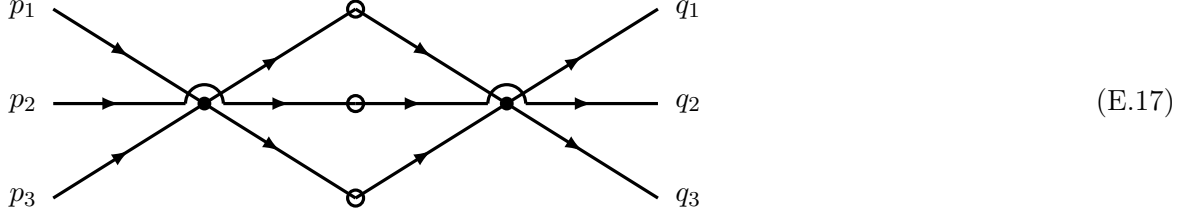
where the first "beach ball" diagram represents the integral

$$\left(\frac{L}{2\pi}\right)^3 \int \mathrm{d}p_1 \mathrm{d}p_2 \mathrm{d}p_3 \exp[-\tau\epsilon(p_1)] \exp[-\tau\epsilon(p_2)] \exp[-\tau\epsilon(p_3)] \exp[-\tau\epsilon(p_1 + p_2 - p_3)]. \quad \text{(E.19)}$$

Note that in the "beach ball" diagram, each line should also carry one open circle, but we omitted for clarity.

The twisted trace diagram is connected and also a "beach ball" diagram with different weights

$$\text{(E.20)}$$

where we again omitted the single open circle in the other three lines. Similarly, the corresponding integral is

$$\left(\frac{L}{2\pi}\right)^3 \int \mathrm{d}p_1 \mathrm{d}p_2 \mathrm{d}p_3 \exp[-3\tau\epsilon(p_1)] \exp[-\tau\epsilon(p_2)] \exp[-\tau\epsilon(p_3)] \exp[-\tau\epsilon(p_1 + p_2 - p_3)]. \quad \text{(E.21)}$$

The two cross-term diagrams at $\mathcal{O}(C^2)$ are also equivalent due to the cyclic symmetry and is

in form of
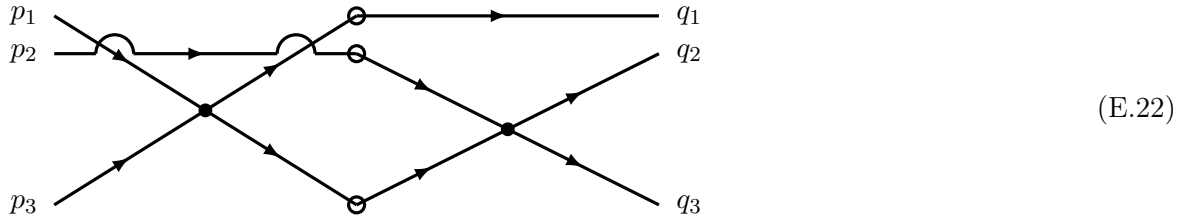
(E.22)

The normal trace diagram is
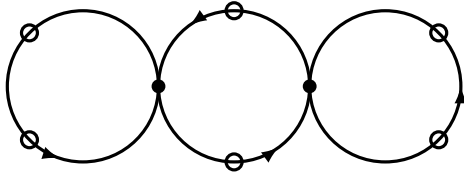
(E.23)

corresponding to the integral

$$\left(\frac{L}{2\pi}\right)^3 \int \mathrm{d}p_1 \mathrm{d}p_2 \mathrm{d}p_3 \exp[-2\tau\epsilon(p_1)] \exp[-2\tau\epsilon(p_2)] \exp[-2\tau\epsilon(p_3)] = Q_{10}^3(\beta).$$

(E.24)

And the twisted trace diagram is the same "beach ball" diagram as in Eq. (E.20).

REFERENCES

[1] D. M. Eagles, *Possible Pairing without Superconductivity at Low Carrier Concentrations in Bulk and Thin-Film Superconducting Semiconductors*, Physical Review **186**, 2, 456 (1969).

[2] A. J. Leggett, *COOPER PAIRING IN SPIN-POLARIZED FERMI SYSTEMS*, Le Journal de Physique Colloques **41**, C7, C7 (1980).

[3] P. Noziéres and S. Schmitt-Rink, *Bose condensation in an attractive fermion gas: From weak to strong coupling superconductivity*, Journal of Low Temperature Physics **59**, 3-4, 195 (1985).

[4] Y. Ohashi and A. Griffin, *BCS-BEC Crossover in a Gas of Fermi Atoms with a Feshbach Resonance*, Physical Review Letters **89**, 13, 130402 (2002).

[5] C. A. Regal, M. Greiner, and D. S. Jin, *Observation of Resonance Condensation of Fermionic Atom Pairs*, Physical Review Letters **92**, 4, 040403 (2004).

[6] M. W. Zwierlein, C. A. Stan, C. H. Schunck, S. M. F. Raupach, A. J. Kerman, and W. Ketterle, *Condensation of Pairs of Fermionic Atoms near a Feshbach Resonance*, Physical Review Letters **92**, 12, 120403 (2004).

[7] M. Randeria and E. Taylor, *Crossover from Bardeen-Cooper-Schrieffer to Bose-Einstein Condensation and the Unitary Fermi Gas*, Annual Review of Condensed Matter Physics **5**, 1, 209 (2014).

[8] M. Randeria, N. Trivedi, A. Moreo, and R. T. Scalettar, *Pairing and spin gap in the normal state of short coherence length superconductors*, Physical Review Letters **69**, 13, 2001 (1992).

[9] N. Trivedi and M. Randeria, *Deviations from Fermi-Liquid Behavior aboveTcin 2D Short Coherence Length Superconductors*, Physical Review Letters **75**, 2, 312 (1995).

[10] G. A. Baker, *Neutron matter model*, Physical Review C **60**, 5, 054311 (1999).

[11] L. B. Madsen, *Effective range theory*, American Journal of Physics **70**, 8, 811 (2002).

[12] C. Horowitz and A. Schwenk, *The virial equation of state of low-density neutron matter*, Physics Letters B **638**, 2-3, 153 (2006).

[13] I. Bloch, J. Dalibard, and W. Zwerger, *Many-body physics with ultracold gases*, Reviews of Modern Physics **80**, 3, 885 (2008).

[14] R. Grimm, M. Weidemüller, and Y. B. Ovchinnikov, *Optical Dipole Traps for Neutral Atoms*, in *Advances In Atomic, Molecular, and Optical Physics*, 95–170, (Elsevier, 2000).

[15] J. M. Diederix and H. T. C. Stoof, *Thermodynamics of Trapped Imbalanced Fermi Gases at Unitarity*, in *The BCS-BEC Crossover and the Unitary Fermi Gas*, 477–502, (Springer Berlin Heidelberg, 2011).

[16] H. Moritz, T. Stöferle, K. Günter, M. Köhl, and T. Esslinger, *Confinement Induced Molecules in a 1D Fermi Gas*, Physical Review Letters **94**, 21, 210401 (2005).

[17] C. Chin, R. Grimm, P. Julienne, and E. Tiesinga, *Feshbach resonances in ultracold gases*, Reviews of Modern Physics **82**, 2, 1225 (2010).

[18] S. Kuhr, *Zooming in on Ultracold Matter*, Physics **12**, 36 (2019).

[19] L. W. Cheuk, M. A. Nichols, M. Okan, T. Gersdorf, V. V. Ramasesh, W. S. Bakr, T. Lompe, and M. W. Zwierlein, *Quantum-Gas Microscope for Fermionic Atoms*, Physical Review Letters **114**, 19, 193001 (2015).

[20] R. Pathria and P. Beale, *Statistical Mechanics*, Academic Press, (Butterworth-Heinemann, 2011).

[21] Y. Yan and D. Blume, *Path-Integral Monte Carlo Determination of the Fourth-Order Virial Coefficient for a Unitary Two-Component Fermi Gas with Zero-Range Interactions*, Physical Review Letters **116**, 23 (2016).

[22] J. E. Mayer and E. Montroll, *Molecular Distribution*, The Journal of Chemical Physics **9**, 1, 2 (1941).

[23] E. E. Salpeter, *On Mayer's theory of cluster expansions*, Annals of Physics **5**, 3, 183 (1958).

[24] X.-J. Liu, *Virial expansion for a strongly correlated Fermi system and its application to ultracold atomic Fermi gases*, Physics Reports **524**, 2, 37 (2013).

[25] A. J. Czejdo, J. E. Drut, Y. Hou, and K. J. Morrell, *Toward an Automated-Algebra Framework for High Orders in the Virial Expansion of Quantum Matter*, Condensed Matter **7**, 1 (2022).

[26] M. D. Hoffman, P. D. Javernick, A. C. Loheac, W. J. Porter, E. R. Anderson, and J. E. Drut, *Universality in one-dimensional fermions at finite temperature: Density, pressure, compressibility, and contact*, Physical Review A **91**, 3, 033618 (2015).

[27] A. C. Loheac and J. E. Drut, *Third-order perturbative lattice and complex Langevin analyses of the finite-temperature equation of state of nonrelativistic fermions in one dimension*, Physical Review D **95**, 9 (2017).

[28] X.-J. Liu, H. Hu, and P. D. Drummond, *Exact few-body results for strongly correlated quantum gases in two dimensions*, Physical Review B **82**, 5, 054524 (2010).

[29] C. Chafin and T. Schäfer, *Scale breaking and fluid dynamics in a dilute two-dimensional Fermi gas*, Physical Review A **88**, 4, 043636 (2013).

[30] V. Ngampruetikorn, J. Levinsen, and M. M. Parish, *Pair Correlations in the Two-Dimensional Fermi Gas*, Physical Review Letters **111**, 26, 265301 (2013).

[31] M. Barth and J. Hofmann, *Pairing effects in the nondegenerate limit of the two-dimensional Fermi gas*, Physical Review A **89**, 1, 013614 (2014).

[32] W. Daza, J. E. Drut, C. Lin, and C. Ordóñez, *Virial expansion for the Tan contact and Beth-Uhlenbeck formula from two-dimensional SO(2,1) anomalies*, Physical Review A **97**, 3, 033630 (2018).

[33] C. R. Ordóñez, *Path-integral Fujikawa's approach to anomalous virial theorems and equations of state for systems with SO(2,1) symmetry*, Physica A: Statistical Mechanics and its Applications **446**, 64 (2016).

[34] D. Lee and T. Schäfer, *Cold dilute neutron matter on the lattice. I. Lattice virial coefficients and large scattering lengths*, Physical Review C **73**, 1, 015201 (2006).

[35] C. Horowitz and A. Schwenk, *Cluster formation and the virial equation of state of low-density nuclear matter*, Nuclear Physics A **776**, 1-2, 55 (2006).

[36] V. G. J. Stoks, R. A. M. Klomp, M. C. M. Rentmeester, and J. J. de Swart, *Partial-wave analysis of all nucleon-nucleon scattering data below 350 MeV*, Physical Review C **48**, 2, 792 (1993).

[37] H. E. Camblong, A. Chakraborty, W. S. Daza, J. E. Drut, C. L. Lin, and C. R. Ordóñez, *Spectral density, Levinson's theorem, and the extra term in the second virial coefficient for the one-dimensional δ -function potential*, Physical Review A **100**, 6 (2019).

[38] A. Pais and G. E. Uhlenbeck, *On the Quantum Theory of the Third Virial Coefficient*, Physical Review **116**, 2, 250 (1959).

[39] B. J. Baumgartl, *Second and third virial coefficient of a quantum gas from two-particle scattering amplitude*, Zeitschrift für Physik **198**, 2, 148 (1967).

[40] R. Dashen, S.-k. Ma, and H. J. Bernstein, *S-Matrix Formulation of Statistical Mechanics*, Phys. Rev. **187**, 345 (1969).

[41] X. Leyronas, *Virial expansion with Feynman diagrams*, Physical Review A **84**, 5 (2011).

[42] D. B. Kaplan and S. Sun, *New Field-Theoretic Method for the Virial Expansion*, Physical Review Letters **107**, 3 (2011).

[43] S. Endo and Y. Castin, *The interaction-sensitive states of a trapped two-component ideal Fermi gas and application to the virial expansion of the unitary Fermi gas*, Journal of Physics A: Mathematical and Theoretical **49**, 26, 265301 (2016).

[44] S. Endo and Y. Castin, *Unitary boson-boson and boson-fermion mixtures: third virial coefficient and three-body parameter on a narrow Feshbach resonance*, The European Physical Journal D **70**, 11, 238 (2016).

[45] C. Gao, S. Endo, and Y. Castin, *The third virial coefficient of a two-component unitary Fermi gas across an Efimov-effect threshold*, EPL (Europhysics Letters) **109**, 1, 16003 (2015).

[46] V. Ngampruetikorn, M. M. Parish, and J. Levinsen, *High-temperature limit of the resonant Fermi gas*, Physical Review A **91**, 1 (2015).

[47] P. F. Bedaque and G. Rupak, *Dilute resonating gases and the third virial coefficient*, Physical Review B **67**, 17, 174513 (2003).

[48] J. R. Armstrong, N. T. Zinner, D. V. Fedorov, and A. S. Jensen, *Virial expansion coefficients in the harmonic approximation*, Physical Review E **86**, 2 (2012).

[49] N. Sakumichi, Y. Nishida, and M. Ueda, *Lee-Yang cluster expansion approach to the BCS-BEC crossover: BCS and BEC limits*, Physical Review A **89**, 3, 033622 (2014).

[50] T. D. Lee and C. N. Yang, *Many-Body Problem in Quantum Statistical Mechanics. I. General Formulation*, Physical Review **113**, 5, 1165 (1959).

[51] T. D. Lee and C. N. Yang, *Many-Body Problem in Quantum Statistical Mechanics. II. Virial Expansion for Hard-Sphere Gas*, Physical Review **116**, 1, 25 (1959).

[52] F. Mohling, *Linked-Pair Expansions in Quantum Statistics*, Physical Review **122**, 4, 1043 (1961).

[53] C. D. Dominicis, *Variational Formulations of Equilibrium Statistical Mechanics*, Journal of Mathematical Physics **3**, 5, 983 (1962).

[54] X.-J. Liu, H. Hu, and P. D. Drummond, *Virial Expansion for a Strongly Correlated Fermi Gas*, Physical Review Letters **102**, 16, 160401 (2009).

[55] F. Werner and Y. Castin, *Unitary Quantum Three-Body Problem in a Harmonic Trap*, Physical Review Letters **97**, 15, 150401 (2006).

[56] D. Rakshit, K. M. Daily, and D. Blume, *Natural and unnatural parity states of small trapped equal-mass two-component Fermi gases at unitarity and fourth-order virial coefficient*, Physical Review A **85**, 3 (2012).

[57] Y. Yan and D. Blume, *Incorporating exact two-body propagators for zero-range interactions intoN-body Monte Carlo simulations*, Physical Review A **91**, 4, 043607 (2015).

[58] S. E. Gharashi, K. M. Daily, and D. Blume, *Three s-wave-interacting fermions under anisotropic harmonic confinement: Dimensional crossover of energetics and virial coefficients*, Phys. Rev. A **86**, 042702 (2012).

[59] S.-G. Peng, S.-H. Zhao, and K. Jiang, *Virial expansion of a harmonically trapped Fermi gas across a narrow Feshbach resonance*, Physical Review A **89**, 1 (2014).

[60] T. Kristensen, X. Leyronas, and L. Pricoupenko, *Second-order virial expansion for an atomic gas in a harmonic waveguide*, Physical Review A **93**, 6 (2016).

[61] M. J. H. Ku, A. T. Sommer, L. W. Cheuk, and M. W. Zwierlein, *Revealing the Superfluid Lambda Transition in the Universal Thermodynamics of a Unitary Fermi Gas*, Science **335**, 6068, 563 (2012).

[62] S. Nascimbène, N. Navon, K. J. Jiang, F. Chevy, and C. Salomon, *Exploring the thermodynamics of a universal Fermi gas*, Nature **463**, 7284, 1057 (2010).

[63] R. K. Bhaduri, W. van Dijk, and M. V. N. Murthy, *Universal Equation of State of a Unitary Fermionic Gas*, Physical Review Letters **108**, 26, 260402 (2012).

[64] R. K. Bhaduri, W. van Dijk, and M. V. N. Murthy, *Higher virial coefficients of a unitary Fermi gas*, Physical Review A **88**, 4 (2013).

[65] C. W. Johnson, W. E. Ormand, K. S. McElvain, and H. Shan, *BIGSTICK: A flexible configuration-interaction shell-model code* (2018).

[66] B. R. Barrett, P. Navrátil, and J. P. Vary, *Ab initio no core shell model*, Progress in Particle and Nuclear Physics **69**, 131 (2013).

[67] R. J. Bartlett and M. Musiał, *Coupled-cluster theory in quantum chemistry*, Reviews of Modern Physics **79**, 1, 291 (2007).

[68] G. Hagen, T. Papenbrock, M. Hjorth-Jensen, and D. J. Dean, *Coupled-cluster computations of atomic nuclei*, Reports on Progress in Physics **77**, 9, 096302 (2014).

[69] D. Ceperley, G. V. Chester, and M. H. Kalos, *Monte Carlo simulation of a many-fermion study*, Physical Review B **16**, 7, 3081 (1977).

[70] S. Tanaka, *Structural optimization in variational quantum Monte Carlo*, The Journal of Chemical Physics **100**, 10, 7416 (1994).

[71] D. M. Ceperley, *Path integrals in the theory of condensed helium*, Reviews of Modern Physics **67**, 2, 279 (1995).

[72] S. Duane, A. Kennedy, B. J. Pendleton, and D. Roweth, *Hybrid Monte Carlo*, Physics Letters B **195**, 2, 216 (1987).

[73] J. E. Drut and A. N. Nicholson, *Lattice methods for strongly interacting many-body systems*, Journal of Physics G: Nuclear and Particle Physics **40**, 4, 043101 (2013).

[74] X. Wang and H.-G. Matuttis, *The Fermionic Minus-Sign Problem for the Ground State, Revisited with Higher Order Suzuki–Trotter Decompositions*, Journal of the Physical Society of Japan **81**, 10, 104002 (2012).

[75] R. L. Stratonovich, *On a Method of Calculating Quantum Distribution Functions*, Soviet Physics Doklady **2**, 416 (1957).

[76] J. Hubbard, *Calculation of Partition Functions*, Physical Review Letters **3**, 2, 77 (1959).

[77] C. Körber, E. Berkowitz, and T. Luu, *Sampling general N-body interactions with auxiliary fields*, EPL (Europhysics Letters) **119**, 6, 60006 (2017).

[78] D. Lee, *Ground state energy at unitarity*, Physical Review C **78**, 2, 024001 (2008).

[79] D. Roscher, J. Braun, J.-W. Chen, and J. E. Drut, *Fermi gases with imaginary mass imbalance and the sign problem in Monte-Carlo calculations*, Journal of Physics G: Nuclear and Particle Physics **41**, 5, 055110 (2014).

[80] L. Rammelmüller, W. J. Porter, J. E. Drut, and J. Braun, *Surmounting the sign problem in nonrelativistic calculations: A case study with mass-imbalanced fermions*, Physical Review D **96**, 9, 094506 (2017).

[81] V. A. Goy, V. Bornyakov, D. Boyda, A. Molochkov, A. Nakamura, A. Nikolaev, and V. Zakharov, *Sign problem in finite density lattice QCD*, Progress of Theoretical and Experimental Physics **2017**, 3 (2017).

[82] M. Troyer and U.-J. Wiese, *Computational Complexity and Fundamental Limitations to Fermionic Quantum Monte Carlo Simulations*, Physical Review Letters **94**, 17, 170201 (2005).

[83] T. Nakamura, N. Hatano, and H. Nishimori, *Reweighting Method for Quantum Monte Carlo Simulations with the Negative-Sign Problem*, Journal of the Physical Society of Japan **61**, 10, 3494 (1992).

[84] S. Chandrasekharan, *Fermion Bag Approach to Fermion Sign Problems*, The European Physical Journal A **49**, 7 (2013).

[85] Z.-X. Li, Y.-F. Jiang, and H. Yao, *Solving the fermion sign problem in quantum Monte Carlo simulations by Majorana representation*, Physical Review B **91**, 24, 241117 (2015).

[86] C. Gattringer and K. Langfeld, *Approaches to the sign problem in lattice field theory*, International Journal of Modern Physics A **31**, 22, 1643007 (2016).

[87] C. E. Berger, L. Rammelmüller, A. C. Loheac, F. Ehmann, J. Braun, and J. E. Drut, *Complex Langevin and other approaches to the sign problem in quantum many-body physics*, Physics Reports **892**, 1 (2021).

[88] P. Broecker and S. Trebst, *Numerical stabilization of entanglement computation in auxiliary-field quantum Monte Carlo simulations of interacting many-fermion systems*, Physical Review E **94**, 6, 063306 (2016).

[89] C. Bauer, *Fast and stable determinant quantum Monte Carlo*, SciPost Phys. Core **2**, 11 (2020).

[90] C. R. Shill and J. E. Drut, *Virial coefficients of one-dimensional and two-dimensional Fermi gases by stochastic methods and a semiclassical lattice approximation*, Physical Review A **98**, 5 (2018).

[91] F. Ruskey, C. Savage, and T. M. Y. Wang, *Generating necklaces*, Journal of Algorithms **13**, 3, 414 (1992).

[92] F. Ruskey and J. Sawada, *An efficient algorithm for generating necklaces with fixed density*, SIAM Journal on Computing **29**, 2, 671 (1999).

[93] J. Sawada, *A fast algorithm to generate necklaces with fixed content*, Theoretical Computer Science **301**, 1-3, 477 (2003).

[94] M. Lüscher, *Volume dependence of the energy spectrum in massive quantum field theories*, Communications in Mathematical Physics **105**, 2, 153 (1986).

[95] R. Pordes, D. Petravick, B. Kramer, D. Olson, M. Livny, A. Roy, P. Avery, K. Blackburn, T. Wenaus, F. Würthwein, I. Foster, R. Gardner, M. Wilde, A. Blatecky, J. McGee, and R. Quick, *The open science grid*, Journal of Physics: Conference Series **78**, 012057 (2007).

[96] I. Sfiligoi, D. C. Bradley, B. Holzman, P. Mhashilkar, S. Padhi, and F. Wurthwein, *The Pilot Way to Grid Resources Using glideinWMS*, in *2009 WRI World Congress on Computer Science and Information Engineering*, (IEEE, 2009).

[97] G. Baker, *The Padé approximant in theoretical physics*, (Academic Press, New York, 1970).

[98] A. George Jr *et al.*, *Essentials of Padé approximants*, (Elsevier, 1975).

[99] R. Roth and J. Langhammer, *Padé-resummed high-order perturbation theory for nuclear structure calculations*, Physics Letters B **683**, 4-5, 272 (2010).

[100] R. Rossi, T. Ohgoe, K. V. Houcke, and F. Werner, *Resummation of Diagrammatic Series with Zero Convergence Radius for Strongly Correlated Fermions*, Physical Review Letters **121**, 13, 130405 (2018).

[101] Y. Nishida and D. T. Son, *Unitary Fermi Gas, ϵ Expansion, and Nonrelativistic Conformal Field Theories*, in *The BCS-BEC Crossover and the Unitary Fermi Gas*, 233–275, (Springer Berlin Heidelberg, 2011).

[102] Y. Nishida and D. T. Son, *ϵ Expansion for a Fermi Gas at Infinite Scattering Length*, Physical Review Letters **97**, 5, 050403 (2006).

[103] P. Arnold, J. E. Drut, and D. T. Son, *Next-to-next-to-leading-order ϵ expansion for a Fermi gas at infinite scattering length*, Physical Review A **75**, 4, 043605 (2007).

[104] Y. Hou and J. E. Drut, *Fourth- and Fifth-Order Virial Coefficients from Weak Coupling to Unitarity*, Physical Review Letters **125**, 5, 050403 (2020).

[105] L. Rammelmüller, Y. Hou, J. E. Drut, and J. Braun, *Pairing and the spin susceptibility of the polarized unitary Fermi gas in the normal phase*, Physical Review A **103**, 4, 043330 (2021).

[106] T.-L. Ho, *Universal Thermodynamics of Degenerate Quantum Gases in the Unitarity Limit*, Physical Review Letters **92**, 9, 090402 (2004).

[107] E. Braaten and H.-W. Hammer, *Universality in few-body systems with large scattering length*, Physics Reports **428**, 5-6, 259 (2006).

[108] S. Giorgini, L. P. Pitaevskii, and S. Stringari, *Theory of ultracold atomic Fermi gases*, Reviews of Modern Physics **80**, 4, 1215 (2008).

[109] J. Levinsen, P. Massignan, S. Endo, and M. M. Parish, *Universality of the unitary Fermi gas: a few-body perspective*, Journal of Physics B: Atomic, Molecular and Optical Physics **50**, 7, 072001 (2017).

[110] G. C. Strinati, P. Pieri, G. Röpke, P. Schuck, and M. Urban, *The BCS-BEC crossover: From ultra-cold Fermi gases to nuclear systems*, Physics Reports **738**, 1 (2018).

[111] Y. Castin and F. Werner, *Le troisième coefficient du viriel du gaz de Bose unitaire*, Canadian Journal of Physics **91**, 5, 382 (2013).

[112] S. Endo and Y. Castin, *Absence of a four-body Efimov effect in the 2+2 fermionic problem*, Physical Review A **92**, 5, 053624 (2015).

[113] S. Tan, *Energetics of a strongly correlated Fermi gas*, Annals of Physics **323**, 12, 2952 (2008).

[114] S. Tan, *Large momentum part of a strongly correlated Fermi gas*, Annals of Physics **323**, 12, 2971 (2008).

[115] S. Tan, *Generalized virial theorem and pressure relation for a strongly correlated Fermi gas*, Annals of Physics **323**, 12, 2987 (2008).

[116] J. E. Drut, T. A. Lähde, and T. Ten, *Momentum Distribution and Contact of the Unitary Fermi Gas*, Physical Review Letters **106**, 20, 205302 (2011).

[117] E. Taylor and M. Randeria, *Viscosity of strongly interacting quantum fluids: Spectral functions and sum rules*, Physical Review A **81**, 5, 053610 (2010).

[118] J. R. McKenney and J. E. Drut, *Fermi-Fermi crossover in the ground state of one-dimensional few-body systems with anomalous three-body interactions*, Physical Review A **99**, 1, 013615 (2019).

[119] F. Werner and Y. Castin, *General relations for quantum gases in two and three dimensions: Two-component fermions*, Physical Review A **86**, 1, 013626 (2012).

[120] M. Valiente, N. T. Zinner, and K. Mølmer, *Universal properties of Fermi gases in arbitrary dimensions*, Physical Review A **86**, 4, 043616 (2012).

[121] M. Valiente, N. T. Zinner, and K. Mølmer, *Universal relations for the two-dimensional spin-1/2 Fermi gas with contact interactions*, Physical Review A **84**, 6, 063626 (2011).

[122] E. Braaten, *Universal Relations for Fermions with Large Scattering Length*, 193–231, (Springer Berlin Heidelberg, Berlin, Heidelberg, 2012).

[123] D. T. Son and E. G. Thompson, *Short-distance and short-time structure of a unitary Fermi gas*, Physical Review A **81**, 6, 063634 (2010).

[124] E. Braaten, D. Kang, and L. Platter, *Short-Time Operator Product Expansion for rf Spectroscopy of a Strongly Interacting Fermi Gas*, Physical Review Letters **104**, 22, 223004 (2010).

[125] E. Braaten, D. Kang, and L. Platter, *Universal relations for a strongly interacting Fermi gas near a Feshbach resonance*, Physical Review A **78**, 5, 053606 (2008).

[126] E. Braaten and L. Platter, *Exact Relations for a Strongly Interacting Fermi Gas from the Operator Product Expansion*, Physical Review Letters **100**, 20, 205301 (2008).

[127] F. Werner, *Virial theorems for trapped cold atoms*, Physical Review A **78**, 2, 025601 (2008).

[128] S. Zhang and A. J. Leggett, *Sum-rule analysis of radio-frequency spectroscopy of ultracold Fermi gas*, Physical Review A **77**, 3, 033614 (2008).

[129] C. Carcy, S. Hoinka, M. G. Lingham, P. Dyke, C. C. N. Kuhn, H. Hu, and C. J. Vale, *Contact and Sum Rules in a Near-Uniform Fermi Gas at Unitarity*, Physical Review Letters **122**, 20, 203401 (2019).

[130] O. Goulko and M. Wingate, *Numerical study of the unitary Fermi gas across the superfluid transition*, Physical Review A **93**, 5, 053604 (2016).

[131] R. Rossi, T. Ohgoe, E. Kozik, N. Prokof'ev, B. Svistunov, K. V. Houcke, and F. Werner, *Contact and Momentum Distribution of the Unitary Fermi Gas*, Physical Review Letters **121**, 13 (2018).

[132] T. Enss, R. Haussmann, and W. Zwerger, *Viscosity and scale invariance in the unitary Fermi gas*, Annals of Physics **326**, 3, 770 (2011).

[133] F. Palestini, A. Perali, P. Pieri, and G. C. Strinati, *Temperature and coupling dependence of the universal contact intensity for an ultracold Fermi gas*, Physical Review A **82**, 2, 021605 (2010).

[134] H. Hu, X.-J. Liu, and P. D. Drummond, *Universal contact of strongly interacting fermions at finite temperatures*, New Journal of Physics **13**, 3, 035007 (2011).

[135] L. Radzihovsky and D. E. Sheehy, *Imbalanced Feshbach-resonant Fermi gases*, Reports on Progress in Physics **73**, 7, 076501 (2010).

[136] F. Chevy and C. Mora, *Ultra-cold polarized Fermi gases*, Reports on Progress in Physics **73**, 11, 112401 (2010).

[137] K. Gubbels and H. Stoof, *Imbalanced Fermi gases at unitarity*, Physics Reports **525**, 4, 255 (2013).

[138] L. Rammelmüller, A. C. Loheac, J. E. Drut, and J. Braun, *Finite-Temperature Equation of State of Polarized Fermions at Unitarity*, Physical Review Letters **121**, 17, 173001 (2018).

[139] Z. Yan, P. B. Patel, B. Mukherjee, R. J. Fletcher, J. Struck, and M. W. Zwierlein, *Boiling a Unitary Fermi Liquid*, Physical Review Letters **122**, 9, 093401 (2019).

[140] T. Enss and R. Haussmann, *Quantum Mechanical Limitations to Spin Diffusion in the Unitary Fermi Gas*, Physical Review Letters **109**, 19 (2012).

[141] F. Palestini, P. Pieri, and G. C. Strinati, *Density and Spin Response of a Strongly Interacting Fermi Gas in the Attractive and Quasirepulsive Regime*, Physical Review Letters **108**, 8, 080401 (2012).

[142] P.-A. Pantel, D. Davesne, and M. Urban, *Polarized Fermi gases at finite temperature in the BCS-BEC crossover*, Physical Review A **90**, 5, 053629 (2014).

[143] G. Wlazłowski, P. Magierski, J. E. Drut, A. Bulgac, and K. J. Roche, *Cooper Pairing Above the Critical Temperature in a Unitary Fermi Gas*, Physical Review Letters **110**, 9, 090401 (2013).

[144] S. Jensen, C. N. Gilbreth, and Y. Alhassid, *The pseudogap regime in the unitary Fermi gas*, The European Physical Journal Special Topics **227**, 15-16, 2241 (2019).

[145] A. Richie-Halford, J. E. Drut, and A. Bulgac, *Emergence of a Pseudogap in the BCS-BEC Crossover*, Physical Review Letters **125**, 6 (2020).

[146] H. Tajima, T. Kashimura, R. Hanai, R. Watanabe, and Y. Ohashi, *Uniform spin susceptibility and spin-gap phenomenon in the BCS-BEC-crossover regime of an ultracold Fermi gas*, Physical Review A **89**, 3, 033617 (2014).

[147] C. Sanner, E. J. Su, A. Keshet, W. Huang, J. Gillen, R. Gommers, and W. Ketterle, *Speckle Imaging of Spin Fluctuations in a Strongly Interacting Fermi Gas*, Physical Review Letters **106**, 1, 010402 (2011).

[148] A. Sommer, M. Ku, G. Roati, and M. W. Zwierlein, *Universal spin transport in a strongly interacting Fermi gas*, Nature **472**, 7342, 201 (2011).

[149] Y. Long, F. Xiong, and C. V. Parker, *Spin Susceptibility above the Superfluid Onset in Ultracold Fermi Gases*, Physical Review Letters **126**, 15, 153402 (2021).

[150] E. J. Mueller, *Review of pseudogaps in strongly interacting Fermi gases*, Reports on Progress in Physics **80**, 10, 104401 (2017).

[151] I. Boettcher, J. Braun, T. K. Herbst, J. M. Pawlowski, D. Roscher, and C. Wetterich, *Phase structure of spin-imbalanced unitary Fermi gases*, Physical Review A **91**, 1, 013610 (2015).

[152] Y. il Shin, C. H. Schunck, A. Schirotzek, and W. Ketterle, *Phase diagram of a two-component Fermi gas with resonant interactions*, Nature **451**, 7179, 689 (2008).

[153] M. Pini, P. Pieri, R. Grimm, and G. C. Strinati, *Beyond-mean-field description of a trapped unitary Fermi gas with mass and population imbalance*, Physical Review A **103**, 2, 023314 (2021).

[154] B. Frank, J. Lang, and W. Zwerger, *Universal Phase Diagram and Scaling Functions of Imbalanced Fermi Gases*, Journal of Experimental and Theoretical Physics **127**, 5, 812 (2018).

[155] S. Nascimbène, N. Navon, S. Pilati, F. Chevy, S. Giorgini, A. Georges, and C. Salomon, *Fermi-Liquid Behavior of the Normal Phase of a Strongly Interacting Gas of Cold Atoms*, Physical Review Letters **106**, 21, 215303 (2011).

[156] C. Lobo, A. Recati, S. Giorgini, and S. Stringari, *Normal State of a Polarized Fermi Gas at Unitarity*, Physical Review Letters **97**, 20, 200403 (2006).

[157] O. Goulko and M. Wingate, *Thermodynamics of balanced and slightly spin-imbalanced Fermi gases at unitarity*, Physical Review A **82**, 5, 053621 (2010).

[158] Y. Hou, A. J. Czejdo, J. DeChant, C. R. Shill, and J. E. Drut, *Leading- and next-to-leading-order semiclassical approximation to the first seven virial coefficients of spin-1/2 fermions across spatial dimensions*, Physical Review A **100**, 6, 063627 (2019).

[159] Y. Hou and J. E. Drut, *Virial expansion of attractively interacting Fermi gases in one, two, and three dimensions, up to fifth order*, Physical Review A **102**, 3, 033319 (2020).

[160] A. C. Loheac, J. Braun, and J. E. Drut, *Polarized fermions in one dimension: Density and polarization from complex Langevin calculations, perturbation theory, and the virial expansion*, Physical Review D **98**, 5, 054507 (2018).

[161] J. Levinsen and M. M. Parish, *STRONGLY INTERACTING TWO-DIMENSIONAL FERMI GASES*, in *Annual Review of Cold Atoms and Molecules*, 1–75, (WORLD SCIENTIFIC, 2015).

[162] E. R. Anderson and J. E. Drut, *Pressure, Compressibility, and Contact of the Two-Dimensional Attractive Fermi Gas*, Physical Review Letters **115**, 11 (2015).

[163] M. Bauer, M. M. Parish, and T. Enss, *Universal Equation of State and Pseudogap in the Two-Dimensional Fermi Gas*, Physical Review Letters **112**, 13, 135302 (2014).

[164] I. Boettcher, L. Bayha, D. Kedar, P. Murthy, M. Neidig, M. Ries, A. Wenz, G. Zürn, S. Jochim, and T. Enss, *Equation of State of Ultracold Fermions in the 2D BEC-BCS Crossover Region*, Physical Review Letters **116**, 4, 045303 (2016).

[165] K. Fenech, P. Dyke, T. Peppler, M. Lingham, S. Hoinka, H. Hu, and C. Vale, *Thermodynamics of an Attractive 2D Fermi Gas*, Physical Review Letters **116**, 4, 045302 (2016).

[166] J. McCabe and S. Ouvry, *Perturbative three-body spectrum and the third virial coefficient in the anyon model*, Physics Letters B **260**, 1, 113 (1991).

[167] X.-J. Liu, H. Hu, and P. D. Drummond, *Three attractively interacting fermions in a harmonic trap: Exact solution, ferromagnetism, and high-temperature thermodynamics*, Physical Review A **82**, 2 (2010).

[168] H. Bateman, *Higher transcendental functions [volumes i-iii]*, vol. 2, (McGraw-Hill Book Company, 1953).

[169] K. J. Morrell, C. E. Berger, and J. E. Drut, *Third- and fourth-order virial coefficients of harmonically trapped fermions in a semiclassical approximation*, Physical Review A **100**, 6, 063626 (2019).

[170] A. Alexandru, P. Bedaque, E. Berkowitz, and N. C. Warrington, *Structure Factors of Neutron Matter at Finite Temperature*, Physical Review Letters **126**, 13, 132701 (2020).

[171] A. Alexandru, P. F. Bedaque, and N. C. Warrington, *Structure factors of the unitary gas under supernova conditions*, Physical Review C **101**, 4 (2020).

[172] M. Sun, P. Zhang, and H. Zhai, *High Temperature Virial Expansion to Universal Quench Dynamics*, Phys. Rev. Lett. **125**, 110404 (2020).

[173] P. F. Bedaque, S. Reddy, S. Sen, and N. C. Warrington, *Neutrino-nucleon scattering in the neutrino-sphere*, Physical Review C **98**, 1 (2018).

[174] T. Enss, *Bulk Viscosity and Contact Correlations in Attractive Fermi Gases*, Phys. Rev. Lett. **123**, 205301 (2019).

[175] Y. Nishida, *Viscosity spectral functions of resonating fermions in the quantum virial expansion*, Annals of Physics **410**, 167949 (2019).

[176] J. Hofmann, *High-temperature expansion of the viscosity in interacting quantum gases*, Physical Review A **101**, 1, 013620 (2020).

[177] G. Shen, C. J. Horowitz, and S. Teige, *Equation of state of nuclear matter in a virial expansion of nucleons and nuclei*, Phys. Rev. C **82**, 045802 (2010).

[178] E. O'Connor, C. J. Horowitz, Z. Lin, and S. Couch, *Core-Collapse Supernova Simulations including Neutrino Interactions from the Virial EOS*, Proceedings of the International Astronomical Union **12**, S331, 107 (2017).

[179] C. Horowitz and A. Schwenk, *The neutrino response of low-density neutron matter from the virial expansion*, Physics Letters B **642**, 4, 326 (2006).

[180] C. J. Horowitz, G. Shen, E. O'Connor, and C. D. Ott, *Charged-current neutrino interactions in core-collapse supernovae in a virial expansion*, Physical Review C **86**, 6 (2012).

[181] G. Shen, C. J. Horowitz, and E. O'Connor, *Second relativistic mean field and virial equation of state for astrophysical simulations*, Physical Review C **83**, 6 (2011).

[182] C. J. Horowitz, O. L. Caballero, Z. Lin, E. O'Connor, and A. Schwenk, *Neutrino-nucleon scattering in supernova matter from the virial expansion*, Physical Review C **95**, 2 (2017).

[183] Z. Lin and C. J. Horowitz, *Neutrino scattering in supernovae and the universal spin correlations of a unitary gas*, Physical Review C **96**, 5 (2017).

[184] Y. Nishida and D. T. Son, *Universal four-component Fermi gas in one dimension*, Physical Review A **82**, 4, 043606 (2010).

[185] P. Makotyn, C. E. Klauss, D. L. Goldberger, E. A. Cornell, and D. S. Jin, *Universal dynamics of a degenerate unitary Bose gas*, Nature Physics **10**, 2, 116 (2014).